Estimating Energy Dissipation Due to Wave Breaking in the Surf Zone Using Infrared Imagery

Roxanne J Carini

A thesis
submitted in partial fulfillment of the
requirements for the degree of

Master of Science in Civil Engineering

University of Washington

2014

Reading Committee:

Andrew T Jessup, Chair

C Chris Chickadel

Jim Thomson

Program Authorized to Offer Degree:
Civil and Environmental Engineering

University of Washington

Abstract

Estimating Energy Dissipation
Due to Wave Breaking in the Surf Zone
Using Infrared Imagery

Roxanne J Carini

Chair of the Supervisory Committee:
Dr. Andrew T Jessup
Civil and Environmental Engineering

Wave breaking is the largest forcing mechanism in the surf zone. Therefore, quantifying energy dissipation due to wave breaking is important for improving models that seek to predict nearshore circulation, wave-current interactions, air-sea gas exchange, erosion and accretion of sediment, and storm surge. Wave energy dissipation is difficult to measure with *in situ* instruments, and even the most reliable estimates are limited to point measurements. Using remote sensing technologies, specifically infrared (IR) imagery, the high spatial and temporal variability of wave breaking may be sampled. Duncan (1981) proposed a model (D81) for dissipation on a wave-by-wave basis, based on wave slope and roller length, the crest-perpendicular length of the aerated region of a breaking wave. The wave roller is composed of active foam, which, in thermal IR images, appears brighter than the surrounding water and the residual foam, the foam left behind in the wake of a breaking wave. Using IR imagery taken during the Surf Zone Optics 2010 experiment at Duck, NC, and exploiting the distinct signature of active foam, a retrieval algorithm was developed to identify and extract breaking wave roller length. Roller length was then used to estimate dissipation rate via the D81 formulation. The D81 dissipation rate estimates compare reasonably to *in situ* dissipation estimates at a point. When the D81 estimates are compared to the bulk energy flux into the surf zone, it is found that wave breaking dissipates approximately 25-36% of the incoming wave energy. The D81 dissipation rate estimates also agree closely with those

from a dissipation parameterization proposed by Janssen and Battjes (2007) (JB07) and commonly applied within larger nearshore circulation models. The JB07 formulation, however, requires additional physical parameters (wave height and water depth) that are often sparsely sampled and are difficult to attain from remote sensing alone. The power of the D81 formulation lies in its dependence on surface signatures alone, and with the methods developed here and those proposed for future work, wave energy dissipation rate maps could be produced for any imageable coastline.

TABLE OF CONTENTS

LIST OF FIGURES

ACKNOWLEDGMENTS

Thank you, Andy and Chris, for all your guidance, insight, and compassion. Working with you, I've grown as a scientist and learned how to ask good questions (the kind that motivate even more questions). This *becoming a scientist* business is an ongoing process, and your continued encouragement helps me take ownership of and initiative in my research. At the same time, you remind me of the big picture. As academic advisors and mentors, you were especially supportive when, in the home stretch, life tossed me around a bit. With your help and understanding, I realized that there is a time to push through rough surf, but there's also a time to ride a breaker in to shore and take some rest. After all, the waves will be there when I return! Thank you for everything.

Thank you to my committee, Andy, Chris, and Jim, for your questions and feedback. Thank you to the Environmental Fluid Mechanics group, for your academic camaraderie and inquiry, and for Thursday barbecues. Thank you to the DARLA-MURI researchers at OSU and WHOI, for sharing your perspective and fostering a collaborative environment. To my Seattle family of housemates, teammates, classmates, and friends, thanks for all your love and support. You have all helped make me a better scientist, and I look forward to the discussions and discoveries ahead.

This research was made possible by DARLA-MURI funding from the Office of Naval Research (Award Number: N000141010932) and additional student funding from the NDIA UWD Academic Fellowship Program 2011-2012. Thank you to the USACE and the APL-UW team at the Field Research Facility in Duck, NC, for collecting and sharing this fruitful dataset. I was not yet attending UW when the Surf Zone Optics 2010 experiment took place, so your work enabled mine. Finally, thank you to the Civil & Environmental Engineering Department of UW and the Air-Sea Interactions and Remote Sensing Department of APL for academic resources and support.

DEDICATION

To my family,

for your incredible support of my adventures out West...

even though it is really, *really* far away.

I am so very thankful for you.

Chapter 1

INTRODUCTION

This research was pursued in the context of an ongoing larger project titled Data Assimilation and Remote Sensing for Littoral Applications (DARLA), a Multidisciplinary University Research Initiative (MURI) funded by the Office of Naval Research. The project's objectives are to evaluate and improve the estimation of physical parameters from remote sensing data, determine the extent to which remote sensing technologies can replace the use of *in situ* instruments, and infer bathymetry in littoral environments using remote sensing and data assimilation models. This thesis contributes to the achievement of the first two DARLA objectives. Infrared (IR) imagery was used to estimate the physical parameters necessary to evaluate the Duncan (1981) and Janssen and Battjes (2007) models of energy dissipation due to wave breaking in the surf zone (D81 and JB07, respectively). Ultimately, some *in situ* measurements were required, but this research provides a solid first step to estimating wave energy dissipation solely from remote sources. Since wave breaking is the primary forcing mechanism in the surf zone, detailed spatial and temporal estimation of energy dissipation due to wave breaking is important for models that seek to predict nearshore processes. Wave energy dissipation estimates are useful for a diverse group of predictive models: air-sea gas exchange, nearshore circulation, wave-current interactions, beach erosion, storm surge, and bathymetry inversion.

Measuring, understanding, and predicting wave breaking in the surf zone is crucial. The surf zone is rife with bathymetry changes, subject to currents and river plumes, strongly modulated by tidal fluctuations, and influenced by local weather. The shallow water approximations to the linear wave equations are often applied to shoaling incoming waves, but breaking is a nonlinear, episodic event. As will be shown, breaking waves and the residual foam left in their wake are distinguishable from each other and from background water in IR imagery. This can facilitate a study of the evolution of a breaking wave. In the present

research, the roller length, or the crest-perpendicular length of the aerated region of the breaking wave, is extracted from a cross-shore transect using IR imagery of the surf zone. The onset, growth, and completion of a breaking wave can be mapped through changes in the roller length, and it is this roller length that Duncan (1981) used in his parameterization of energy dissipation due to wave breaking. Here, the first steps are taken towards remotely estimating dissipation due to wave breaking in the surf zone. Retrieval algorithms for breaking wave parameters from IR imagery are developed, and these remotely-derived parameters, along with some supplementary *in situ* data, are employed to field test D81. The D81 estimate of energy dissipation due to wave breaking compares well with *in situ* estimates and a commonly used wave dissipation model, JB07.

This thesis first reviews the IR signal of the sea surface, explains how wave breaking affects the energy balance in the surf zone, and provides an overview of the D81 and JB07 parameterizations. The methods for IR image processing and the development of the retrieval algorithm are then be presented in detail. The results of the remote and *in situ* dissipation rate estimates are compared, and the underlying assumptions, confidence levels, and implications are discussed. Finally, future research and next steps are proposed.

Chapter 2

BACKGROUND

2.1 IR imaging of the sea surface

A thermal infrared camera is a passive sensor that collects emitted and reflection radiation along its look-path within a given wavelength band (8-9.2μm for the IR imager used in this research). Because the imager operates in the thermal IR band, it can collect data during the day or at night. In a thermal IR image of the surf zone, regions that are bright are relatively warmer and regions that are dark are relatively cooler. The signal received by the IR sensor is composed of the radiation emitted from the surface and the radiation reflected from the background. A simplified radiative transfer equation can be used to explain the IR signal received by the imager. IR radiation received at a sensor is composed of emitted and reflected components from the water surface according to,

$$L_{meas} = \epsilon(\vartheta) L_{water} + \varrho(\vartheta) L_{sky}(\vartheta), \tag{2.1}$$

for a given wavelength. Here, ϑ is the incidence angle, L is the radiance measured, emitted by the sea surface, or reflected from the sky, and $\epsilon(\vartheta)$ and $\varrho(\vartheta)$ are the emissivity and reflectivity of the sea surface, respectively (Figure 2.1). Emissivity and reflectivity of water vary with incidence angle, such that as the angle at which the surface is observed increases from nadir to near-grazing, emissivity decreases (Masuda et al., 1988).

By conservation of energy, the sum of the fraction of radiation transmitted $\tau(\vartheta)$, absorbed $\alpha(\vartheta)$, and reflected $\varrho(\vartheta)$, must be unity:

$$\tau(\vartheta) + \alpha(\vartheta) + \varrho(\vartheta) = 1. \tag{2.2}$$

The sea surface is opaque to IR radiation ($\tau(\vartheta) = 0$), which yields:

$$\alpha(\vartheta) + \varrho(\vartheta) = 1. \tag{2.3}$$

Kirchoff's law of thermal radiation states that, for a body in thermodynamic equilibrium, the ratio of its emissivity to its absorptivity is unity. This means that all absorbed energy is re-emitted, or,

$$\alpha(\vartheta) = \epsilon(\vartheta). \tag{2.4}$$

Combining (2.3) and (2.4) gives,

$$\epsilon(\vartheta) + \varrho(\vartheta) = 1. \tag{2.5}$$

The assumption that the sea surface absorbs and emits in equilibrium, and that (2.5) is valid, has been tested and found sufficient (Masuda, 2006). Thus (2.1) can be rewritten, using (2.5), as a function of emissivity:

$$L_{meas} = \epsilon(\vartheta)L_{water} + (1 - \epsilon(\vartheta))L_{sky}(\vartheta). \tag{2.6}$$

It is the dependence of emissivity on incidence angle that permits an IR imager to "see" waves. For a camera obliquely viewing the surf zone from a distance and at near-grazing incidence angle ($\geq 60°$), a small change in the local incidence angle (i.e. wave slope) produces a large change in emissivity and thus a large change in measured radiance (Figure 2.2 (Niclos et al., 2007)). Ultimately, this incidence angle-dependent emissivity could be used to develop an inversion algorithm to derive wave slope from IR pixel intensity modulations. However, there are other incidence angle-dependent components of L_{meas} that must be accounted for first.

A consequence of the angular dependence of ϵ is that lower emissivity in the far field causes the sea surface to appear darker, even though its kinetic temperature may not be different than the brighter sea surface in the near field. This effect is pronounced for near-grazing viewing angles. The emissivity of the sea surface in the far field of the image, where incidence angle exceeds 80°, decreases steeply, as seen in Figure 2.2 for incidence angles from nadir to 65°. The pixel intensities in the IR image may be scaled according to incidence angle to correct for this effect. However, there is still incidence angle dependence of $L_{sky}(\vartheta)$.

For cold, clear skies, $L_{sky}(\vartheta)$ can vary due to path length. This is one reason why the horizon may appear bright in IR, even at night. The path length to the horizon increases with incidence angle and incorporates a progressively thicker atmosphere, throughout which

water vapor and other particles emit IR radiation. For partly cloudy skies, the background signal is variable, and a small change in ϑ may be the difference between observing the sea surface reflecting a cool sky background, $L_{sky} << L_{water}$, and observing the sea surface reflecting a warm cloud-covered background, $L_{sky} \approx L_{water}$. In the case of $L_{sky}(\vartheta) = L_{water}$, as can happen for low-lying clouds, (2.6) becomes,

$$\begin{aligned} L_{meas} &= \epsilon(\vartheta)L_{sky}(\vartheta) + (1 - \epsilon(\vartheta))L_{sky}(\vartheta), \\ L_{meas} &= L_{sky}(\vartheta), \end{aligned} \tag{2.7}$$

and the sea surface signal is obscured. In general, $L_{sky}(\vartheta) \cong L_{water}$ results in decreased contrast between the background signal and the signal of breaking waves. This effect is spatially inhomogeneous for partly cloudy skies and spatially homogenous for uniformly overcast skies. It is also temporally variable on a range of timescales as weather changes.

The signatures of active and residual foam are distinct in IR images, but both appear bright in electro-optical (EO) images (Figure 2.5). An actively breaking wave appears warm (bright) because foam has a higher emissivity than non-foamy water at near-grazing incidence angle (Figure 2.2). This effect has been shown by Niclos et al. (2007) to hold whether the sea surface is considered a diffuse or specular reflector. Newer data has extended this relationship to 85° (Branch et al., 2012) and the resulting emissivity curves were found in agreement with extension of the Niclos et al. (2007) curves. Another reason active breakers appear bright may be because the turbulent breaker disrupts the cool skin layer (Jessup et al., 2009), making the slightly warmer bulk water visible to the IR imager. However, residual foam left behind in the wake of a breaking wave cools quickly and appears dark in the IR imagery (Fogelberg, 2003b; G. O. Marmorino, 2005) (Figure 2.4). The exact mechanism through which foam cools quickly has not yet been explained, but enhanced heat loss is most likely due to the increased surface area and spray generation in foamy seas. The distinct IR signals of active and residual foam will be used to extract breaking wave parameters in Section 3.3.2.

2.2 Basic energy balance for the surf zone

The wave energy flux ($\mathcal{F}$) into the surf zone evolves in the cross-shore direction ($d\mathcal{F}/dx$) through wave orbital-induced bottom drag (ε_{bot}), wave breaking (ε_{brk}), and reflection by the beach (reflection coefficient, R), according to:

$$(1-R)\frac{d\mathcal{F}}{dx} = \varepsilon_{brk} + \varepsilon_{bot}. \tag{2.8}$$

This balance neglects along-shore depth variations, nonlinear effects, and directional spreading. Reflection at the beach discussed in this thesis has been previously studied and was found to very with tidal stage (Elgar, 1994). The bottom stress has been estimated using turbulence measurements near the bed and found to be a factor of 2 smaller than the forcing due to wind and waves (Trowbridge and Elgar, 2001). Dissipation due to wave breaking can be further divided into components of turbulent kinetic energy dissipation (ε_{tke}), bubble production and buoyancy (ε_{buoy}), losses to the mean current (ε_{mc}), sediment suspension and transport (ε_{sed}), sound and heat production (ε_{sound}, ε_{heat}), and sea spray production (ε_{spray}) (Lamarre and Melville, 1991; Bryan et al., 2003; Gerbi et al., 2009; Feddersen, 2012; Grasso et al., 2012; Lanckriet and Puleo, 2013):

$$\varepsilon_{brk} = \varepsilon_{tke} + \varepsilon_{buoy} + \varepsilon_{mc} + \varepsilon_{sed} + \varepsilon_{sound} + \varepsilon_{heat} + \varepsilon_{spray}. \tag{2.9}$$

ε_{tke} and ε_{buoy} are coupled because bubbles that are injected into the water column contribute to turbulent mixing as they buoyantly rise. ε_{tke}, ε_{mc}, and ε_{sed}, are energy transformations that occur at depth, while ε_{spray} occurs at the surface ε_{buoy}, ε_{sound}, and ε_{heat}, occur throughout the whole water column and at the surface. These components are difficult to measure individually, so the bulk energy dissipation due to wave breaking is often estimated instead and based on sparse measurements or models of wave height evolution across the surf zone (Collins, 1970; Battjes, 1972; Kuo and Kuo, 1974; Battjes et al., 1978; Thornton and Guza, 1983). The main objective of the research presented here is to use the surface signature of wave breaking as input for a physical model of wave-by-wave energy dissipation to estimate ε_{brk} remotely.

2.3 Duncan's 1981 model

In 1981, Duncan proposed a wave-by-wave model of wave energy dissipation due to breaking (Duncan, 1981), hereafter referred to as D81, as a balance between the shear stress (τ) along the breaking boundary (L_r) and the tangential component (determined by wave slope, θ) of the weight of the aerated breaking region (A) on the underlying wave face (equation (7) in (Duncan, 1981)):

$$\tau L_r = \rho' g A \sin\theta. \tag{2.10}$$

This formulation (2.10) was derived by combining the spatially-integrated and time-averaged vertical and horizontal momentum equations over the breaking region (equations (5) and (6) in D81). In his experiments, Duncan towed a hydrofoil through a flume and measured physical parameters related to the resulting breaking wave. These breaking waves were considered fully developed and breaking in a steady state. Wave speeds were recorded between 0.625m/s and 1.03m/s, wavelengths ranged 0.24m-0.68m, and wave slopes from 10° to 14.7°. Through a series of empirical relationships, Duncan found the ratio of breaking region thickness to length to be self-similar (Figure 2.6):

$$\frac{\text{thickness}}{\text{length}} = \frac{A/L_r}{L_r} = \frac{A}{L_r^2} = 0.11 \pm 0.01. \tag{2.11}$$

As will be shown in Section 3.4.1, (2.10) and (2.11) can be used to estimate dissipation rate due to breaking waves based only on wave slope and roller length (3.16). The D81 formulation has been successfully applied in other laboratory experiments (Haller and Catalan, 2009), but has not yet been field tested. The present research uses the D81 parameterization with IR remote sensing methods to estimate the dissipation rate due to wave breaking on a beach in Duck, NC, where the waves observed in the field cover the same range of wave slopes as in the laboratory, but measure larger wave heights. Also, waves breaking in the surf zone may or may not be considered steady state breakers, like those created in Duncan's experiment. However, the D81 formulation provides a powerful framework for estimating energy dissipation due to wave breaking on a wave-by-wave basis using only a few, remotely-measurable, physical parameters.

2.4 Figures

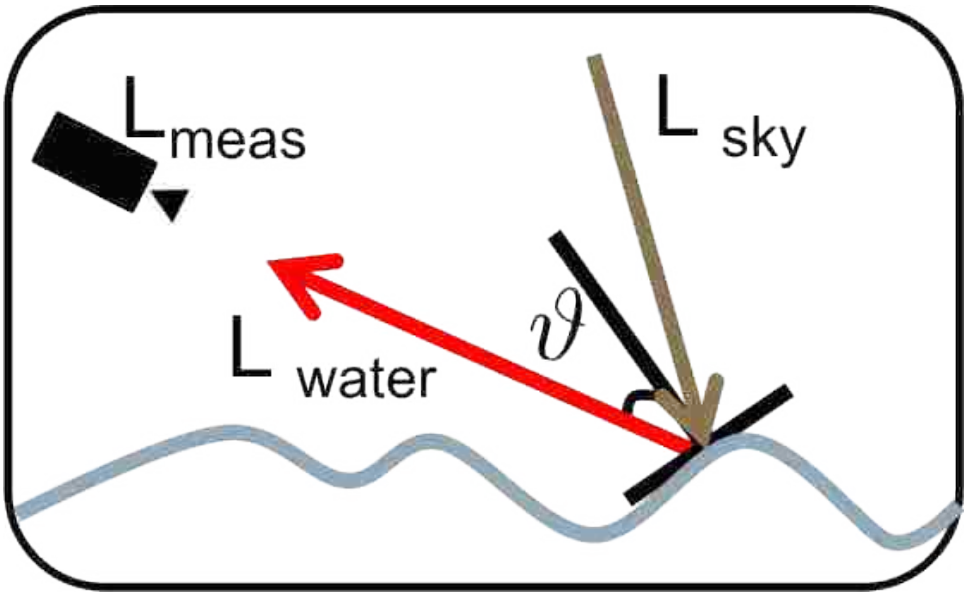

Figure 2.1: Schematic of the simplified radiative transfer equation (2.6). Camera position and look angle not to scale. See Section 2.1 for definitions of L_{meas}, L_{water}, L_{sky}, and ϑ.

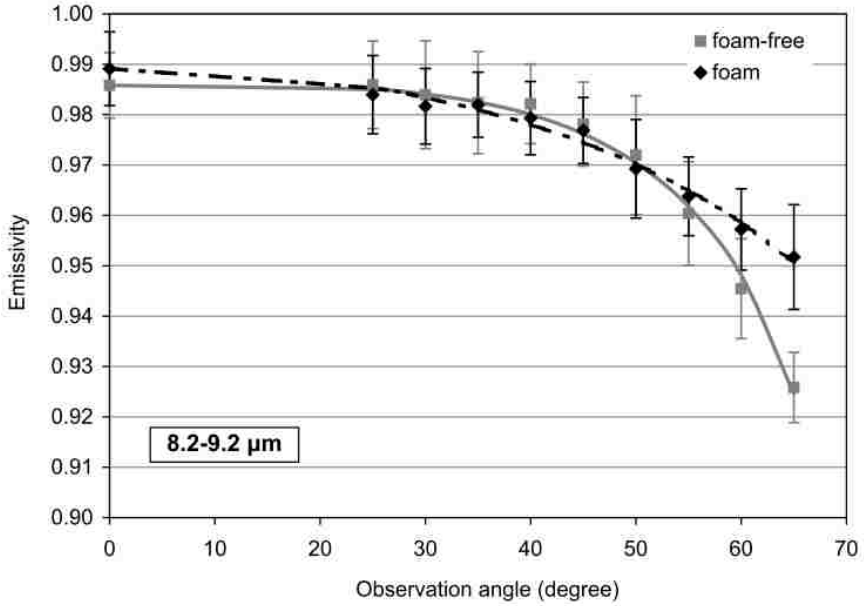

Figure 2.2: The 8.2-9.2μm wavelength panel from Niclos (2007) Figure 6 showing modulation of emissivity of foamy and foam-free sea surface with incidence angle assuming the sea surface is a specular reflector.

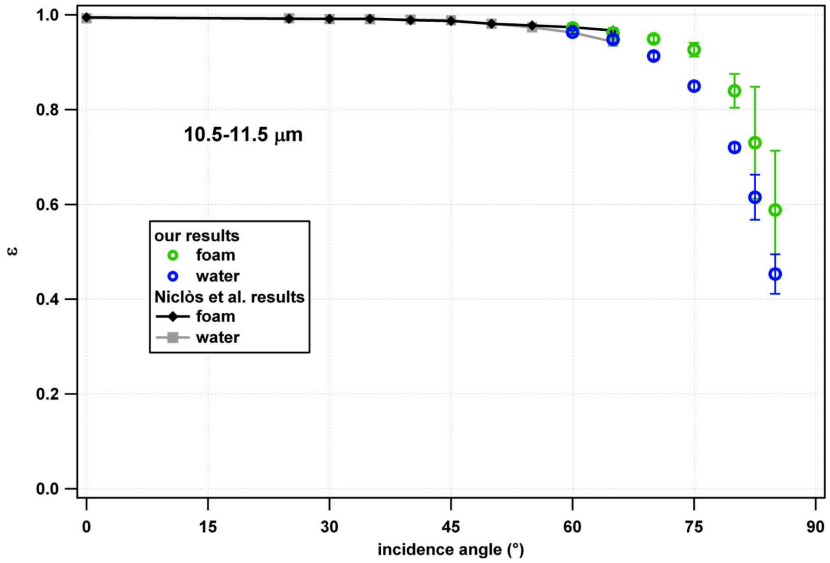

Figure 2.3: Unpublished results (Branch et al., 2012) of the emissivity of foamy and non-foamy salty water as a function of incidence angle. Branch et al. experimented with incidence angles 60-82.5° in the 10.5-11.5 μm thermal IR band. Results are plotted with Niclos et al. (2007) data from the same wavelengths and are found in agreement.

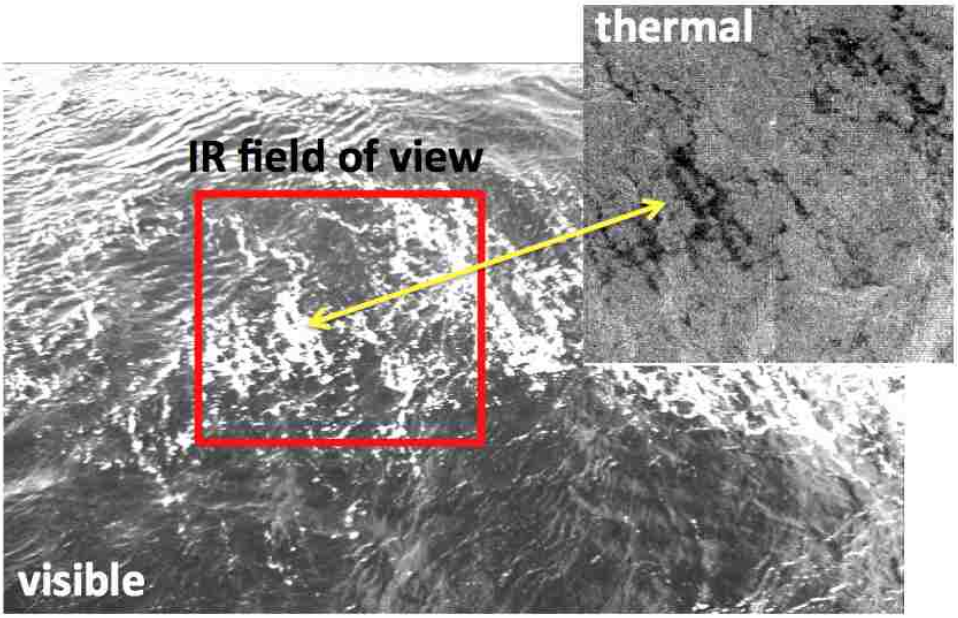

Figure 2.4: Residual foam appears bright in visible image and dark in IR image. (Fogelberg, 2003a)

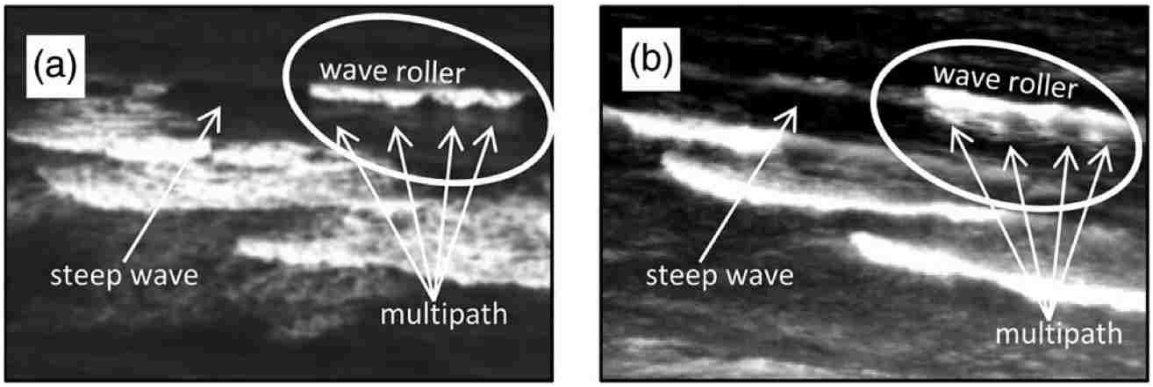

Figure 2.5: Coincident images of breaking waves in the surf zone taken with (a) an EO camera and (b) an IR camera. (a) Residual foam appears bright in the EO image and (b) dark in the IR image. A steep wave face augments the emissivity of the sea surface in the IR image, and the wave rollers are distinct from the residual foam. (Branch et al., 2014)

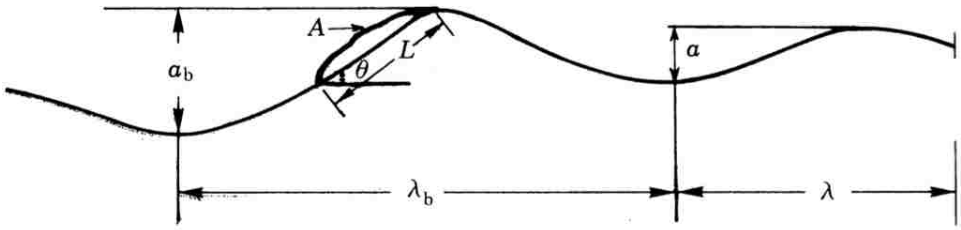

Figure 2.6: Figure 4 from Duncan (1981). Sketch of steady state breaking wave produced for lab experiments. Roller length, L, cross-sectional roller area, A, and wave slope, θ, are labeled. a_b and λ_b are the breaker amplitude and wavelength.

Chapter 3

METHODS

3.1 Experimental setup

The data presented here were collected during the SZO field campaign from September 9-15, 2010, at the Field Research Facility (FRF) maintained by the US Army Corps of Engineers at Duck, NC, shown in Figure 3.1. A right-handed FRF coordinate system is defined with the positive x-axis pointing offshore, the positive y-axis pointing parallel to the shore, and the positive z-axis pointing vertically upward. The shoreline is located at approximately x = 100m and a 560-meter pier extends offshore at y = 510m. The beach morphology is variable, but typically includes a shore-parallel sand bar or terrace, punctuated by rip current channels (Plant et al., 1999). Bathymetry surveys (USACE survey) from before and after the SZO September field campaign (Figure 3.2) reveal regions of deposition and erosion. The survey taken on 09/06/2010, adjusted for tidal elevation, was used in the analysis to follow. At the FRF, significant wave height is commonly 0.2-1.0m; storms and hurricanes episodically increase significant wave heights to 2-3m and sometimes as high as 4-5m (Birkemeier et al., 1985). During this field campaign, the average significant wave height was 0.37m, with a maximum of 0.51m. Figure 3.3 shows the significant wave height, peak and energy-weighted wave frequency, peak wave direction, wind speed and direction, air and water temperature, and shortwave (SW) solar radiation, for the duration of the experiment. These data were acquired by the FRF meteorological station located at the end of the pier. Conditions varied mildly on a daily basis with the exception of a storm on September 12-13, 2010, indicated by the lower, unsteady SW radiation curve and sustained higher wind speed.

A thermal IR camera was mounted at the top of the FRF imaging tower at (x,y,z) = (33.6m, 587.1m, 43.3m), positioned to observe the surf zone. Figure 3.4 shows the 120-foot tower's position relative to the pier, and Figure 3.5 shows the railing-mounted IR

camera. The IR camera used was a cooled Indigo Phoenix (640 x 512 pixel array) operating with a spectral response range of 8-9.2μm. The manufacturer's specified noise equivalent differential temperature (NEDT) is 25mK. The camera has a 37° horizontal by 29.6° vertical field of view (FOV) and was mounted to the tower at a tilt angle of 77.8° from nadir; full frame data were collected at 10Hz. Figure 3.6 provides an example of the infrared camera's field of view. The blue 'x' in this snapshot marks the location of an acoustic doppler current profiler (ADCP). This instrument was a 2MHz, pulse-coherent Nortek Aquadopp HR and sampled at 1Hz with a vertical bin size of 10cm. The number of bins was set to 35, and at high tide (∼3.5m depth) only 30 of those bins were submerged. Pressure and velocity data from the ADCP are used to estimate water depth, wave height, and wave slope (Section 3.4.1). The ADCP data is also used to calculate an *in situ* estimate of dissipation rate (Section 3.4.2), which is compared to a remotely-derived estimate of energy dissipation rate due to wave breaking (Section 4.3).

3.2 Image processing

As previously discussed, breaking rate and roller length are required to calculate an energy dissipation rate due to wave breaking via the methods of JB07 and D81, respectively. The methods developed here provide estimates of these parameters from a cross-shore transect of IR imagery. Using a one-dimensional transect of the surf zone, rather than a two-dimensional area, minimized the amount of data processing and still provided adequate information about the breaking wave field for validation of these techniques. This transect was chosen in FRF coordinates with 0.25m spacing in the x-direction, as seen in Figure 3.7. To maximize the offshore extent of the transect in the image FOV and minimize the distance from the ADCP, the cross-shore transect was drawn at y=725m. The transect begins at x=85m, onshore of the highest high water line, extends over the trough-bar bathymetry displayed in the lower panel of Figure 3.7, and ends offshore at x=245m. Using previously developed image rectification algorithms (Holland and Holman, 1997), the (x,y)-coordinates were mapped into image coordinates (u,v) (Figure 3.8) and modified based on the known biases of the camera (i.e. lens distortion). This resulted in a list of (u,v)-coordinates. To avoid interpolation, the nearest neighboring integer-valued (u,v)-coordinates were used to define

the transect in image space. Figure 3.9 shows how pixel resolution degrades with distance in the alongshore and cross-shore directions. It is clear that stretching is more significant in the cross-shore direction than in the alongshore direction. However, along the transect used for this analysis, misregistration is relatively small in both directions (0.5-1.6m/pixel cross-shore, 0.1-0.25m/pixel alongshore). These resolution factors were accounted for in the rectification process.

Along this transect, 18-minute time series of data were selected from the start of every half hour to create a series of timestacks, such as the one shown in Figure 3.10. In these timestacks, time increases from top to bottom and distance from shore increases to the right. Thus, a shoreward-bound wave roller appears in the timestack as a bright region sloped from upper right to lower left. These wave rollers will be counted and measured to obtain the necessary input parameters for the JB07 and D81 dissipation rate models.

In addition to geometric corrections, any strong spatial or temporal variations in background pixel intensity were addressed before analysis of the timestacks. Temporal intensity variations were usually due to the passage of clouds during the 18-minute time series, and spatial variations were often attributed to emissivity modulation at near grazing incidence angles. (Refer to Section 2.1 for further explanation of cloud effects and incidence angle dependence in the IR signal of the sea surface.) The background intensity need not be uniform across all timestacks, only within a timestack, since each 18-minute segment was treated individually. The aim of the following processing was to normalize the background pixel intensity without reducing the contrast between the background and features of interest (eg. breaking waves).

Before background normalization, the shore and dunes were identified and removed from each timestack. This was done for two reasons: first, the IR signal of the sea surface, not the land, was the target of analysis, and second, the relatively cooler land skewed the pixel intensity distribution towards lower values, which prohibited successful normalization of background intensity levels. To remove the shore from a timestack, the "shore break" and shoreline were defined. The shore break is the region of increased breaking near the shoreline and appears bright in the IR imagery. The shore break was determined using the temporal mean of the timestack. The temporal mean was computed at each cross-shore location, and

the shore break was defined as the position of the maximum mean intensity that occurred between x=85m (the start of the transect) and x=135m (a position seaward of the shoreline at the lowest low tide). Here, the shoreline was estimated as four meters onshore of the shore break, which included the full swash region and excluded the dry beach. If the shore break was identified less than four meters from the beginning of the transect, then the entire transect was preserved. Otherwise, the transect data was limited to the identified shoreline to the offshore extent of transect.

Temporal variations in background intensity were more prevalent than spatial variations and were therefore addressed first. For each timestack (size N_t x N_x), a cumulative distribution function (cdf) was computed from all the pixels at each sample time, and the pixel intensity of the 25th percentile of the cdf was removed from all the data at that sample time. The temporally normalized timestack was computed,

$$\tilde{I}(x,t_j) = I(x,t_j) - I_{25}(t_j), \quad j = 1, ..., N_t, \tag{3.1}$$

where $I_{25}(t_j)$ is the intensity of the 25th percentile of the spatial cdf created from the transect at time t_j. The cdf of $\tilde{I}(x,t)$ was then computed at each x-location, and the pixel intensity of the 5th percentile of its temporal cdf, $\tilde{I}_5(x_i)$, was removed from all the data at the respective x-location following,

$$\hat{I}(x_i,t) = \tilde{I}(x_i,t) - \tilde{I}_5(x_i), \quad i = 1, ..., N_x. \tag{3.2}$$

The choice of the 25th or 5th percentile intensities was qualitatively based on the spatial and temporal dynamic ranges. For a given timestack, the range of pixel intensity exhibited at a sample time was wider than the range displayed at a given x-location. This supports the conclusion that over these short (18-minute) time scales, given constant background (sky) conditions, breaking is more strongly correlated with location (changes in cross-shore bathymetry) than with temporal (tidal) variations in water depth. Finally, the pixel intensity range of each timestack was shifted by subtracting the global minimum value of $\hat{I}(x,t)$,

$$\mathbf{I}(x_i,t_j) = \hat{I}(x_i,t_j) - \min\left[\hat{I}(x,t)\right]. \tag{3.3}$$

3.3 Detection algorithm

3.3.1 Intensity level distributions

Breaking waves appear warm (bright) in thermal IR imagery and are apparent by inspection. To explore the dynamic range of the IR imagery and inform further analysis, histograms created from a region of interest in the surf zone were examined. The size of the sample region was chosen based on observed roller length in order to ensure that over time the IR signals of a breaking wave, residual foam, and background water, were individually sampled. For ease of comparison, the histograms are converted to probability density functions (pdf) using,

$$p(\mathbf{I}) = \frac{n_{\mathbf{I}}}{N}, \qquad \mathbf{I} = 0, ..., L, \tag{3.4}$$

where $n_{\mathbf{I}}$ is the number of pixels of intensity level $\mathbf{I}$, N is the total number of pixels counted, and L is the maximum pixel intensity displayed during a given sampling period. Figure 3.12 shows a series of snapshots taken throughout the passage of the breaking wave, each accompanied by its respective $p(\mathbf{I})$ created from the sample region marked by the red square (covering approximately 4m^2). For spatial reference, the sample region (red square) in each image is the same as that in Figure 3.6. Figure 3.12 illustrates (a) the increased intensity of a passing wave roller followed by (b-c) its wake of cool, residual foam, as well as (d) a quiescent wave state. The black pdf (right y-axis) is the distribution of pixel intensity from a 10-minute record ($N = 6 \times 10^5$) and is the same in each plot. The red pdf (left y-axis) is the distribution of pixel intensity from a 1-second record ($N = 1000$), and reflects the pixel intensities present within the sample region in the accompanying snapshot.

The 10-minute distribution is typically bimodal, with a large broad peak at low intensities due to background water and cooling/cool foam and a small narrow peak at high intensities due to actively breaking waves. The bimodal character of $p(\mathbf{I})$ was also found when sampling at a point or along a transect over time. The example in Figure 3.12 reveals that the bimodal shape occurs through the combination of high intensity breaking waves and mid- to low-intensity quiescent conditions and residual foam. The dramatic distinction between the infrared signal of breaking waves and the rest of the distribution, as seen in

the 1-second distribution in Figure 3.12(a), suggests that thresholding may be sufficient to identify wave rollers. This feature contrast is different than in EO imagery, where both active and residual foam always appear bright, which makes it difficult to distinguish a wave roller from its foamy wake.

3.3.2 Wave roller detection algorithm

Figure 3.12 suggests that a threshold should be chosen at or near the local minimum between the two peaks of the bimodal distribution. While the vast majority of the timestacks produced a pdf that exhibits two distinct peaks, sometimes the modal peak was followed by a small plateau with a monotonically decreasing tail. Figures 3.13, 3.14, and 3.15, illustrate the detection algorithm's performance on three different timestacks whose pdf's exhibit a bimodal distribution, a unimodal-plateau distribution, and an irregular distribution, respectively. For each example, the breaking intensity threshold, $\mathbf{I}_b$, is marked on (a) $p(\mathbf{I})$, (b) $p'(\mathbf{I})$, and (c) $p''(\mathbf{I})$. The first timestack (d) in each figure shows a four-minute segment from the raw data. The second (e) shows the timestack after background intensity normalization. The third timestack (f) is the binary mask created by thresholding the normalized data. As a qualitative assessment of the detection algorithm, the last timestack (g) in these figures overlays the leading edge of each detected breaking wave (taken from the binary mask) and the normalized timestack.

In order to accommodate the different distributions, a threshold was chosen based on the first or second order differences (discrete derivatives) of the pdf,

$$p'(\mathbf{I}) \equiv \frac{\Delta p(\mathbf{I})}{\Delta \mathbf{I}} = \frac{p(\mathbf{I}) - p(\mathbf{I}-1)}{\mathbf{I} - (\mathbf{I}-1)}, \qquad \mathbf{I} = 1, ..., L, \tag{3.5}$$

$$p''(\mathbf{I}) \equiv \frac{\Delta p'(\mathbf{I})}{\Delta \mathbf{I}} = \frac{p'(\mathbf{I}) - p'(\mathbf{I}-1)}{\mathbf{I} - (\mathbf{I}-1)} \qquad \mathbf{I} = 2, ..., L. \tag{3.6}$$

$p'(\mathbf{I})$ describes the rate of change, or slope, of $p(\mathbf{I})$, and $p''(\mathbf{I})$ describes the curvature of $p(\mathbf{I})$. When a bimodal $p(\mathbf{I})$ was present (Figure 3.13(a)), the threshold was chosen as the pixel intensity of the zero-crossing of $p'(\mathbf{I})$, $\mathbf{I}_0$, that occurs at a pixel intensity higher than that of the global minimum of $p'(\mathbf{I})$, $\mathbf{I}_{min}$, as marked in Figure 3.13(a-c). Using this method, the

breaking threshold intensity was defined as,

$$\mathbf{I}_b = \mathbf{I}_0, \tag{3.7}$$

where,

$$p'(\mathbf{I}_0 > \mathbf{I}_{min}) = 0, \tag{3.8}$$

and,

$$p'(\mathbf{I}_{min}) = \min(p'(\mathbf{I})). \tag{3.9}$$

If $\mathbf{I}_0$ did not exist or was equal to L, the maximum pixel intensity observed in the $p(\mathbf{I})$, the second derivative $p''(\mathbf{I})$ was used to determine a threshold. Figure 3.14(a) shows a unimodal $p(\mathbf{I})$ for September 11 at 03:30 EDT. For this example, $\mathbf{I}_0$ was undefined because the first derivative $p'(\mathbf{I})$ in Figure 3.14(b) did not cross zero, so the second derivative was used to define $\mathbf{I}_b$. The second local maximum in the second derivative $p''(\mathbf{I})$, marked in Figure 3.14(c), indicates the pixel intensity at which the curvature of $p(\mathbf{I})$ achieves maximum positive concavity subsequent to the modal peak in the distribution:

$$p''(\mathbf{I}_{max}) = \max(p''(\mathbf{I} > \mathbf{I}_{min})). \tag{3.10}$$

The breaking threshold was then objectively chosen at a pixel intensity higher than $\mathbf{I}_{max}$. Specifically, the algorithm set the threshold intensity as the 25th percentile of the set of $p''(\mathbf{I})$ that satisfies,

$$p''(\mathbf{I} > \mathbf{I}_{max}) > 0, \tag{3.11}$$

and defined the breaking threshold,

$$\mathbf{I}_b = \mathbf{I}_{25}, \tag{3.12}$$

where,

$$p''(\mathbf{I}_{25}) = [p''(\mathbf{I} > \mathbf{I}_{max}) > 0]_{25}. \tag{3.13}$$

After determining $\mathbf{I}_b$ using one of these two methods, the normalized timestacks were converted to binary masks, $M(x,t)$, by setting all pixels whose value equaled or exceeded $\mathbf{I}_b$ to one and all pixels whose value was less than $\mathbf{I}_b$ to zero, written conditionally as,

$$\text{if} \quad \hat{I}(x_i, t_j) \geq \mathbf{I}_b, \quad \text{then} \quad M(x_i, t_j) = 1,$$

$$\text{if} \quad \hat{I}(x_i, t_j) < \mathbf{I}_b, \quad \text{then} \quad M(x_i, t_j) = 0,$$
$$i = 1, ..., N_x, \quad j = 1, ..., N_t. \tag{3.14}$$

Before further analysis, a quality control protocol was employed to ensure that a reasonable threshold was chosen. In some cases where $\mathbf{I}_b$ was chosen via the zero-crossing method, $\mathbf{I}_b$ was set too high, and not all breaking waves were identified. The poor performance of the detection algorithm in these cases was attributed to either unusual behavior of $p(\mathbf{I})$ or failed normalization. Detection algorithm failure was assumed if the percentage of pixels identified as breaking in a given timestack was less than 0.3%:

$$\frac{\sum_{i=1}^{N_x} \sum_{j=1}^{N_t} M(x_i, t_j)}{N_x N_t} < 0.003. \tag{3.15}$$

This percentage is slightly less than that expected if the timestack exhibited only shore break. If this occurred, then a new threshold was set via the $p''(\mathbf{I})$ method, and a new binary mask was created (Figure 3.15). Lastly, basic image processing techniques were used to refine the binary masks. Spurious values were removed if the pixel set to 1 was surrounded by values of 0. If the 8-cell neighborhood around a pixel set to 0 contained at least five values of 1, then that pixel was changed to a 1. Single pixel holes (zeros) in the binary mask were filled if they were surrounded by values of 1. Erosion and dilation image processing techniques were avoided in order to best preserve the dimensions of the identified regions, later used for roller length.

Although most of the imagery collected during the Duck SZO experiment are typified by the bimodal or unimodal-plateau distributions presented in Figures 3.13 and 3.14, there were times when environmental conditions, such as cloud coverage or rain, interfered with the IR signal and limited the success of the detection algorithm. The background intensity of the raw IR timestack in Figure 3.15 exhibited significant temporal variability, most likely due to cloud interference. After normalization, and with the use of $p''(\mathbf{I})$ in the detection algorithm, breaking waves were consistently identified over the bar. However, the detection algorithm failed to identify breaking waves at the shoreline between times 05:42 and 05:43. The timestacks for which $\mathbf{I}_b$ was chosen by employing $p''(\mathbf{I})$ are those with the most inhomogenous

background pixel intensity distributions. These times are marked in gray in Figure 3.3 and will also be noted in the final results.

3.4 Dissipation rate estimation

3.4.1 Duncan (1981) wave energy dissipation model

The Duncan (1981) model expresses the wave energy dissipation rate as a function of roller length L_r and wave slope θ. Recall that Duncan's formulation was developed as a balance between the shear stress of the breaking wave roller on the underlying wave face and the tangential component of the weight of the aerated breaking region (2.10). Duncan also found self-similarity in the geometry of quasi-steady breaking waves (2.11). For each wave observed, Duncan's wave roller dissipation can be calculated, summed over time at each x-position, and divided by record length, t_{total} to produce a dissipation rate estimate at that location (3.16).

$$\varepsilon_{\mathrm{D81}} = \frac{1}{t_{total}} \sum_{i=0}^{N_b} 0.11 \rho' g L_{r,i}^2(x) \sin\theta. \tag{3.16}$$

A forward difference method was used to obtain L_r', the projected roller length. The forward difference with respect to space was taken at every time step (dt=0.1s) in the binary mask. The front edge, or toe, of a breaking wave was indicated every time the forward difference produced a value of 1, x_{toe}. The trailing edge, or crest, of a breaking wave was indicated each time the forward difference produced a value of -1, x_{crest}. The cross-shore position of each breaking wave at time t, x_b, was defined by the midpoint between its toe and crest positions. Therefore the roller length was defined as,

$$L_r'(x_b, t) = x_{crest} - x_{toe}, \tag{3.17}$$

where $x_b = (x_{crest} - x_{toe})/2$. Examples of these wave features (toe and crest) and L_r' are marked in Figure 3.16. The projected roller length was then scaled according to its cross-shore position, estimated wave slope, and propagation direction (See Appendix A for computation details and Section 4.2 for further discussion.):

$$L_r = \frac{L_r'}{r}, \tag{3.18}$$

where r is the projection correction factor. The resultant corrected roller length, L_r, was used to evaluate (3.16). Error bars on $\varepsilon_{\mathrm{D81}}(190,t)$ indicate the maximum and minimum values resulting from the largest and smallest projection error corrections for a given set of wave slope and wave direction parameters.

To evaluate the formulation, roller length and wave slope are required, yet no direct measurement of wave slope was available for this dataset. However, reported values for wave slopes of breaking waves created in laboratory experiments have a range of 2°-24° (Duncan, 1981; Haller and Catalan, 2009; Dally and Brown, 1995; Reniers and Battjes, 1997; Ruessink et al., 2001), and there are several ways to indirectly estimate the slope from field data. Duncan used the slope of a wave in an equilibrium breaking state, whereas the wave slope estimates described here encompass both breaking and non-breaking waves.

A bulk estimate of wave slope, θ, for each 18-minute segment was computed using H_{sig} and half the peak wavelength λ_p:

$$\theta_p = \frac{H_{sig}}{0.5\lambda_p}. \tag{3.19}$$

H_{sig} was estimated by applying linear wave theory for subsurface pressure to the ADCP pressure time series,

$$P = -\rho g z + \rho g \eta K_p(z), \tag{3.20}$$
$$K_p(z) = \frac{\cosh(k(z-h))}{\cosh(-kh)}.$$

Since the ADCP was positioned on the seabed, $z = h$ and $K_p(h) = 1/\cosh(-kh)$. Tidal changes were assumed negligible inside our 18-minute time series, and the mean pressure (in dbars) was used to approximate the mean sea level (MSL). Removing this hydrostatic component from (3.20) yields an equation for the dynamic pressure, P_D, which was solved for η (Figure 3.17):

$$\eta = \frac{P_D}{\rho g K_p(h)}. \tag{3.21}$$

Using the Fourier transform of P_D (pressure in Pa), (3.21) was evaluated in wavenumber space. Then the inverse Fourier transform was taken to recover the wave height time series of η. H_{sig} is equal to four times the standard deviation of η (Dean and Dalrymple, 1984):

$$H_{sig} = 4\sqrt{\frac{1}{n}\sum_{i=1}^{n}(\eta_i - \bar{\eta})^2}. \tag{3.22}$$

Peak wavelength, λ_p, was estimated assuming shallow water linear wave theory: $\lambda_p = c/f_p$. The energy-weighted frequency, f_e, was produced from the wave height spectrum of each 18-minute $\eta(t)$ time series (ADCP), and the phase speed was calculated assuming shallow water, $c = \sqrt{gh}$. This bulk, spectrum-based parametrization produced wave slopes ranging from 1.4° to 4.9°, with an average of 3.2° (Figure 3.18).

Alternatively, a wave-by-wave averaged wave slope was calculated using the *in situ* wave height time series, $\eta(t)$. First, $\eta(t)$ was converted to $\eta(x)$ using an average shallow water phase speed, c,

$$\eta(x) = \eta(t \cdot c). \tag{3.23}$$

Then the peaks and troughs of $\eta(x)$ were identified and the wave slope was calculated,

$$\theta_i = \tan^{-1}\left(\frac{\eta(x_{\text{peak},i}) - \eta(x_{\text{trough},i})}{x_{\text{peak},i} - x_{\text{trough},i}}\right), \tag{3.24}$$

from trough to peak of each wave. The vertical distance from trough to peak is the wave height, H_i. For each 18-minute time series, the average wave slope was estimated from the subset of slopes produced by waves of height H_{rms} (Figure 3.17) or greater, where $H_{rms} = H_{sig}/\sqrt{2}$ (Dean and Dalrymple, 1984). Figure 3.18 compares this time series-derived wave slope with the spectrum-derived wave slope. The wave slope derived from the times series are steeper than the spectrum-derived wave slopes, ranging from 1.8° to 7.6° with a mean of 4.5°. The time series-derived wave slopes (one wave slope estimate for each 18-minute timestack) more closely resemble a wave-by-wave estimate than the spectrum-derived wave slopes and were therefore used to calculate ε_{D81} (3.16). Additionally, the minimum and maximum estimated wave slopes (for each 18-minute time series) were incorporated in the error bar estimation for ε_{D81}.

3.4.2 TKE dissipation rate estimation

In situ TKE dissipation rates were estimated from ADCP data using the methods developed in Wiles et al. (2006) and Thomson (2012). Assuming the measured velocity fluctuations describe turbulent eddies within the inertial subrange, the use of the second order structure function to estimate TKE dissipation rate is valid. In the inertial subrange, cascade theory

gives scaling arguments relating the second order structure function, $D(z,r)$, and TKE dissipation rate, $\varepsilon_{\text{in situ}}$. The second order structure function,

$$D(z,r) = \overline{(v'(z) - v'(z+r))^2}, \tag{3.25}$$

is computed using the ADCP velocity measurements, and the TKE dissipation rate is then estimated according to,

$$\varepsilon_{\text{in situ}} = \frac{(D(z,r) - N)^{3/2}}{C_v^3 r}. \tag{3.26}$$

ADCP velocity data was processed in five-minute bursts to compute a time series of dissipation rate depth profiles, shown in Figure 3.19. Depth-integrating $\varepsilon_{\text{in situ}}$ gives the estimated total TKE dissipation rate at the ADCP's location at a given time. Finally, $\varepsilon_{\text{in situ}}$ was integrated over 18-minute segments every half hour, corresponding to the IR timestack records, to facilitate comparison of the remote and *in situ* estimates.

In addition to breaking waves, this estimate accounts for dissipation due to shear from longshore currents, return flow from shore, and bottom drag. At times when dissipation is dominated by breaking waves, the depth-integrated $\varepsilon_{\text{in situ}}$ may underestimate dissipation due to poor ADCP performance at a highly turbulent (bubble-saturated) interface. At times when breaking is negligible and dissipation is dominated by other sources, the depth-integrated $\varepsilon_{\text{in situ}}$ is expected to measure greater values than ε_{D81}. Additionally, the *in situ* estimate has a depth-integrated noise floor of 3-5W/m^2 (personal correspondence with Jim Thomson), which limits its accuracy at very low dissipation rates.

3.4.3 Janssen and Battjes (2007) wave energy dissipation model

The JB07 model (3.27) requires mean wave frequency $\bar{f}$, the fraction of breaking waves Q_b, root-mean-square wave height H_{rms}, and depth h:

$$\varepsilon_{\text{JB07}} = \frac{3\sqrt{16}}{\pi} \bar{f} B \rho g \frac{H_{rms}^3}{h} Q_b. \tag{3.27}$$

The product of the $\bar{f}$ and Q_b is the breaking rate, which is equivalent to the ratio of the number of breaking waves in a given sampling period to the length of that time period, t_{total}:

$$\bar{f} Q_b = \frac{1}{\overline{T}} \cdot \frac{N_b}{N_{total}} \equiv \frac{N_b}{t_{total}} \tag{3.28}$$

t_{total} was fixed at 1080s and N_b was attained from a binary mask of identified breaking waves. The front edge of a breaking wave was identified in the binary mask when the forward difference in x produced a value of 1. These occurrences were tabulated for each cross-shore bin (dx=0.25m) over the 18-minute timestack, yielding $N_b(x_i)$.

Both H_{rms} and h were acquired (see Section 3.4.1) at a point using the pressure measurement from the ADCP. The JB07 model requires an average depth input, so while $h(t) = MSL + \eta(t)$, the average depth at the ADCP location was taken as $h = MSL$ for (3.27). Again, Figure 3.17(a) shows the mean h over the full experiment record and H_{rms}. In order to apply the JB07 model along the entire transect, an additional model would be needed to estimate H_{rms}. Since these wave shoaling models must include a parameterization of dissipation in order to estimate wave height, the present analysis was completed at one point in the surf zone (x=190m), which preserved the ability to evaluate and compare the two dissipation rate models without contaminating the results on the structure of the dissipation assumptions. The D81 formulation is a function of roller length and wave slope, while the JB07 model is based on breaking rate, wave height, and water depth. Therefore, the D81 and JB07 remote estimates are independent dissipation rate results. The JB07 model is often implemented within larger nearshore circulation models, so the comparison of the two remote estimates is relevant to current research applications (Booij et al., 1999; Ris et al., 1999).

3.5 Figures

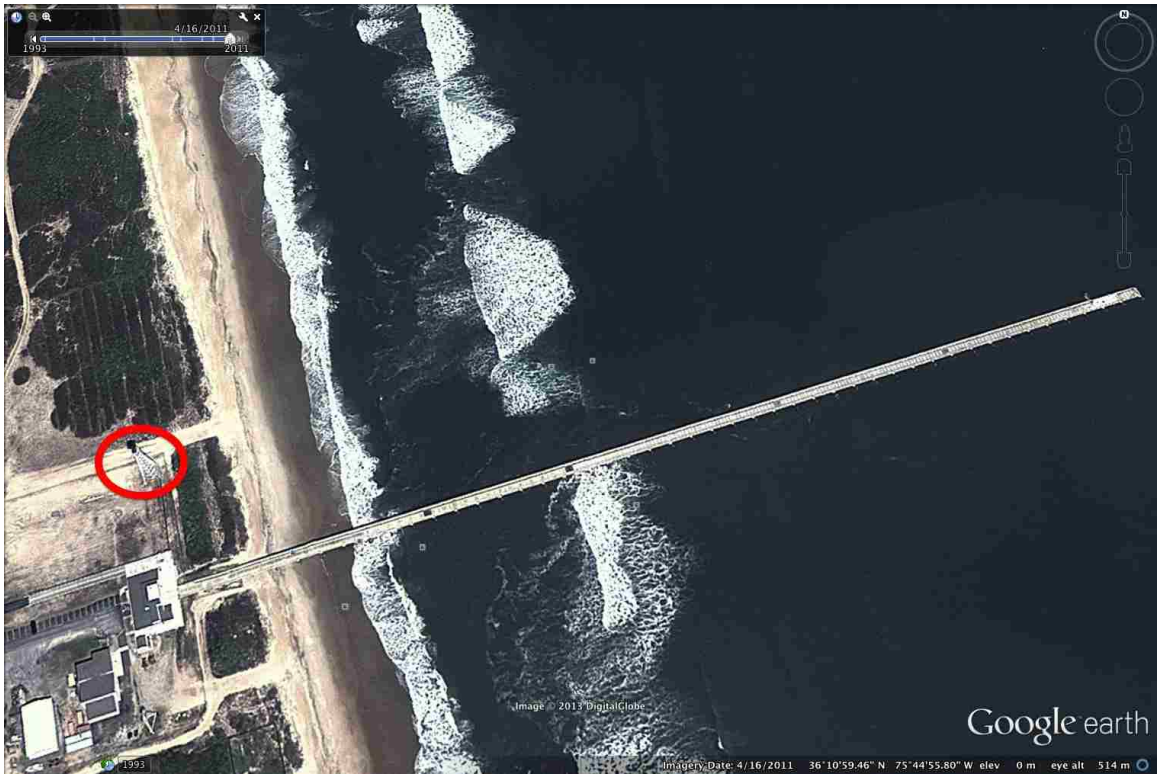

Figure 3.1: A satellite image from April 2011 of the FRF at Duck, NC. The IR camera was installed on the imaging tower, circled in red. Breaking waves are visible at the shoreline and over the sand bar typical at this beach.

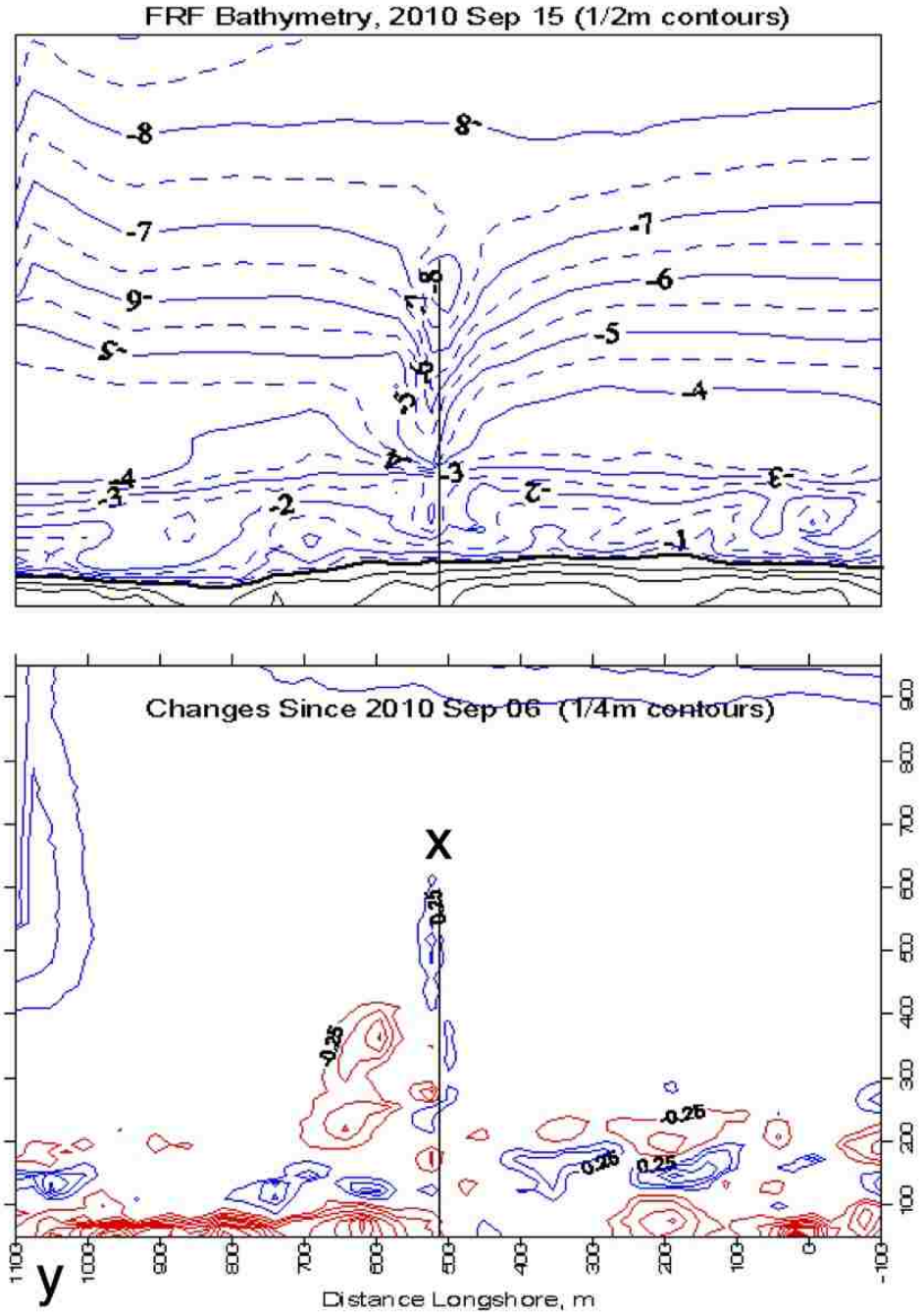

Figure 3.2: (top) Bathymetry of the field site from the end of the experiment on September 15, 2010. (bottom) Changes in bathymetry (red-erosion, blue-deposition) since September 6, 2010 (just before the experiment began) using the FRF coordinate system. (USACE survey)

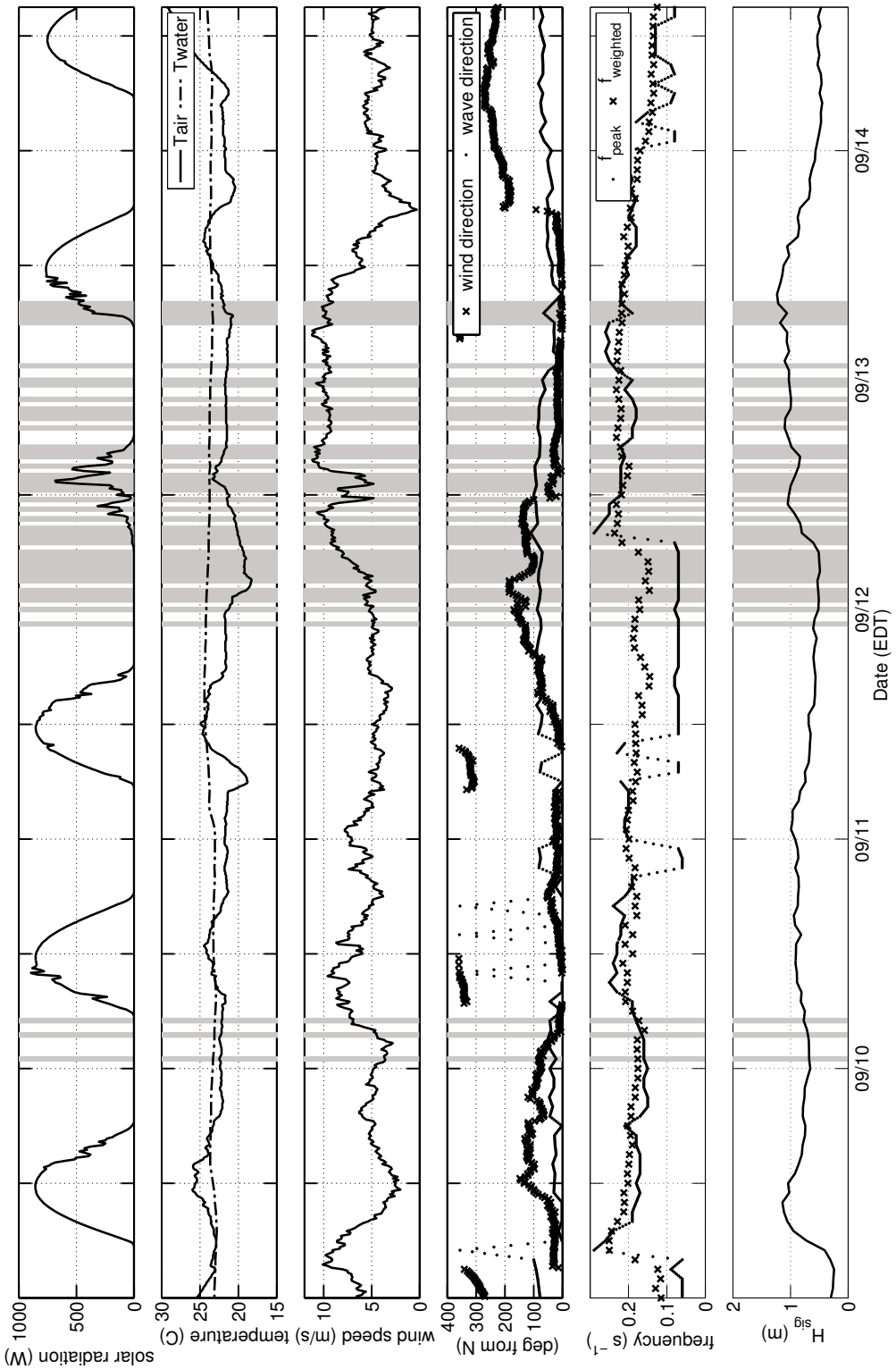

Figure 3.3: Conditions from the FRF at Duck, NC for the SZO experiment (September 9-15, 2010), including (from top) solar radiation, air and water temperature, wind speed, wind and wave direction, peak and energy-weighted wave frequency, and significant wave height. Gray bars mark times when detection algorithm used secondary normalization and thresholding methods (Section 3.3.2) due to storm/cloudy conditions.

Figure 3.4: Looking onshore from the FRF pier. The FRF imaging tower, located at FRF (x,y) = (33.6m, 587.1m), is 43.3m tall.

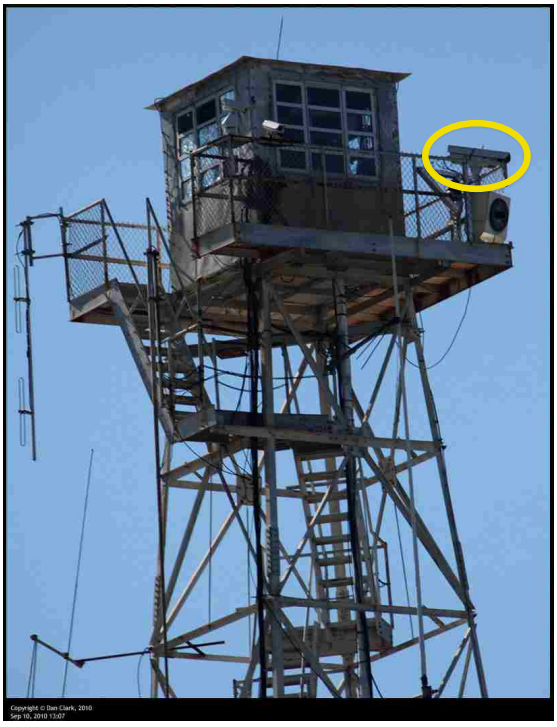

Figure 3.5: IR camera mounted to the railing at the top of tower (circled).

Figure 3.6: Example of the IR camera's field of view. The blue 'x' marks the position of an ADCP. The red box highlights a small region used for an initial investigation of pixel intensity histograms (Section 3.3.1). The black line is the transect from which 18-minute timestacks were created for further analysis (Section 3.3.2).

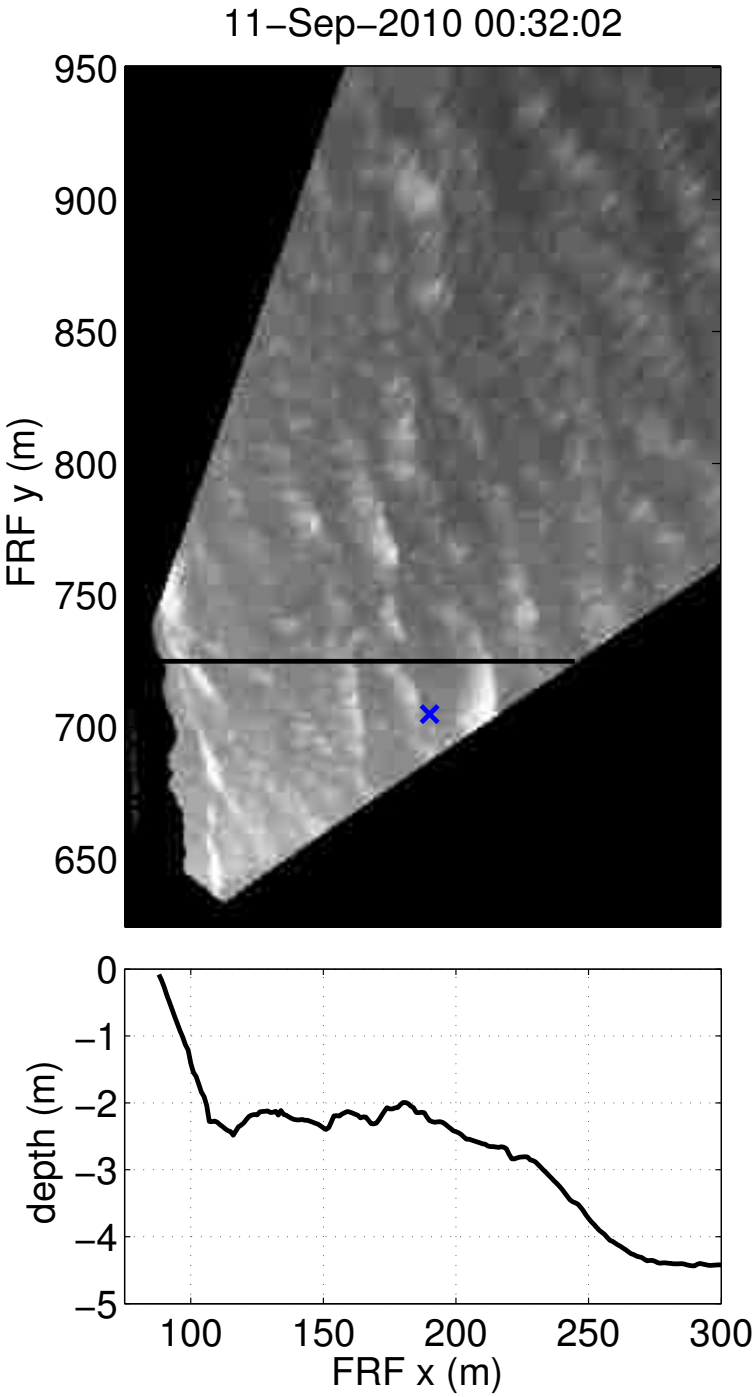

Figure 3.7: (top) Example of the rectified (FRF coordinate system) field of view. Chosen transect and location of in situ ADCP (also in Figure 3.6) are marked. (bottom) Transect bathymetry.

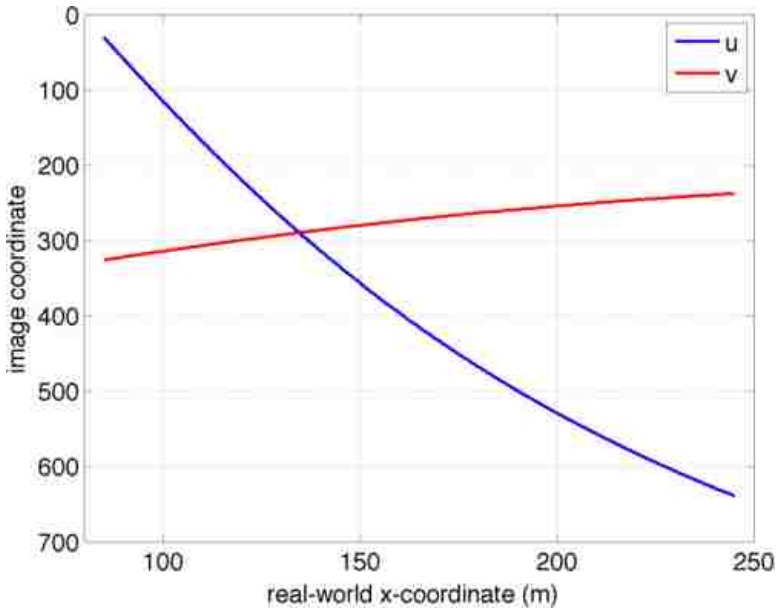

Figure 3.8: Pixel resolution in u and v with distance in x.

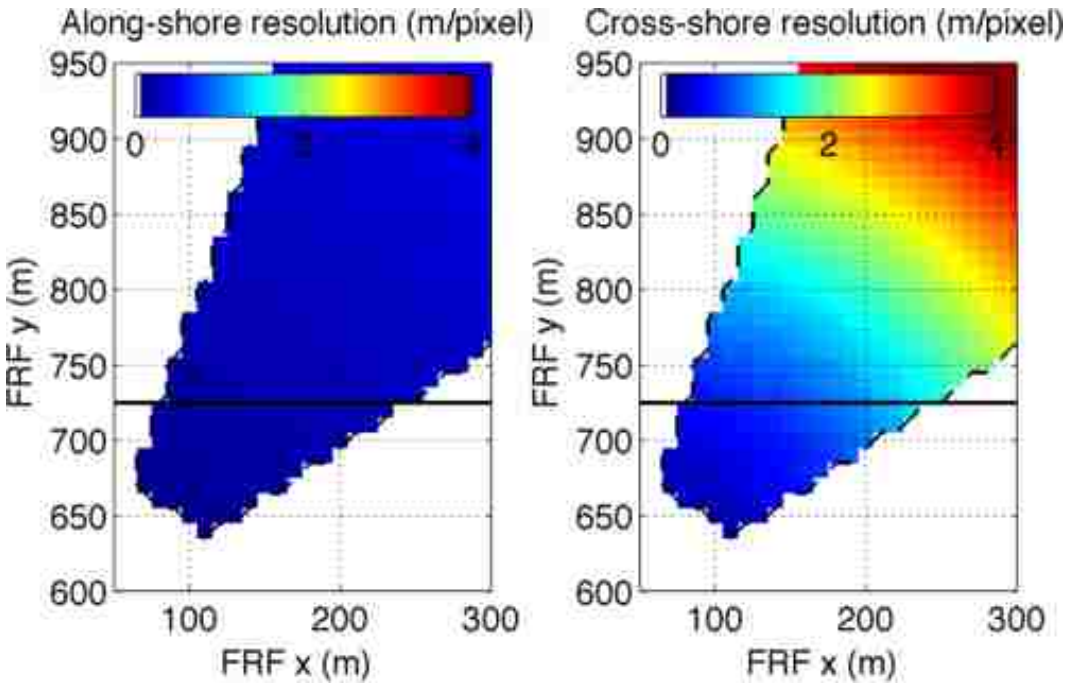

Figure 3.9: Pixel resolution with distance in x and y.

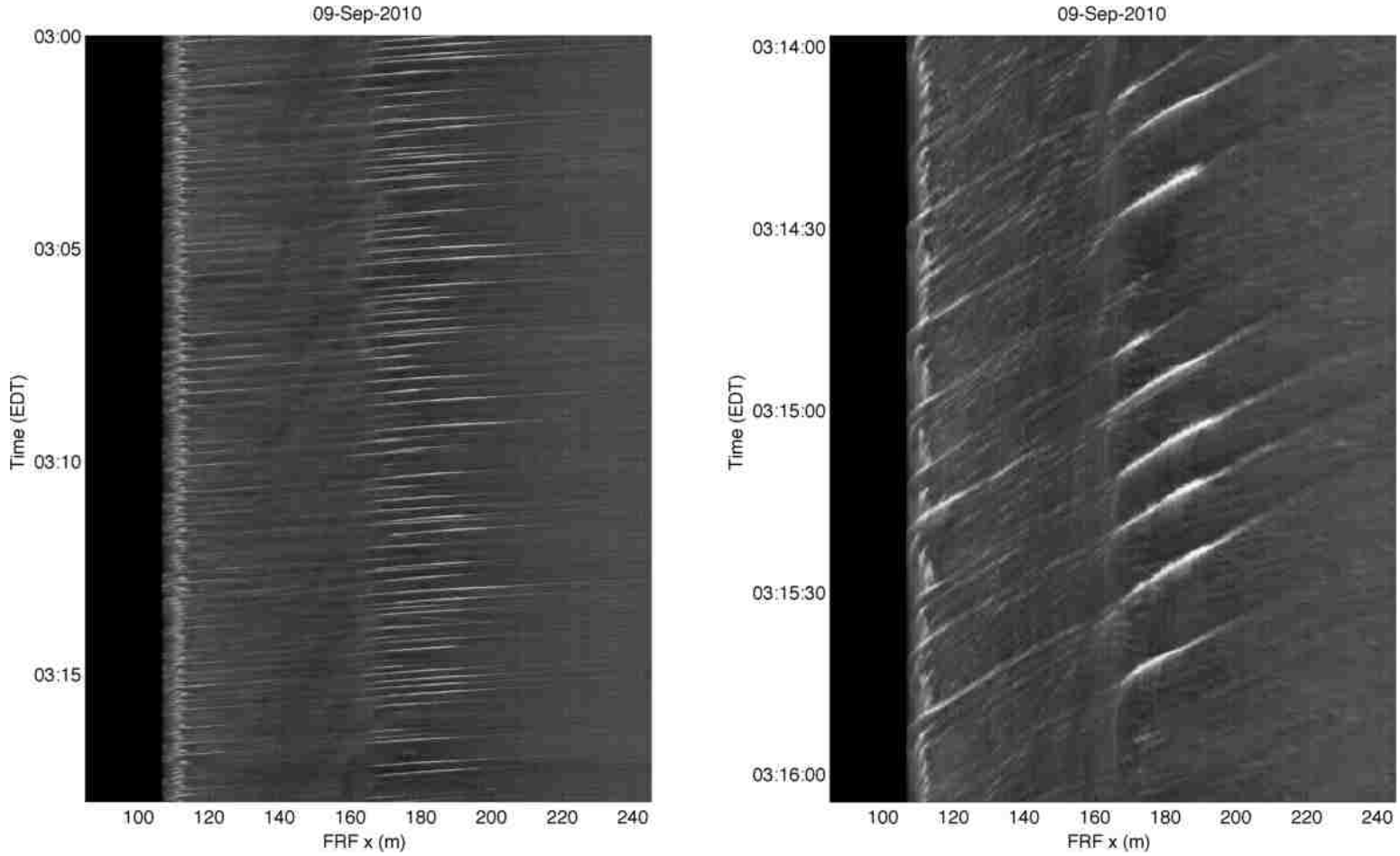

Figure 3.10: (left) Timestack created from 18 minutes of data along the transect shown in Figures 3.6 and 3.7. Time progresses from top to bottom and x increases to the right (shoreline at far left). (right) An expansion of 2 minutes of data shows bright breaking waves over the bar (x≈190m) and at the shoreline. Other passing waves appear as ridges of brighter intensity, though not as bright as breakers.

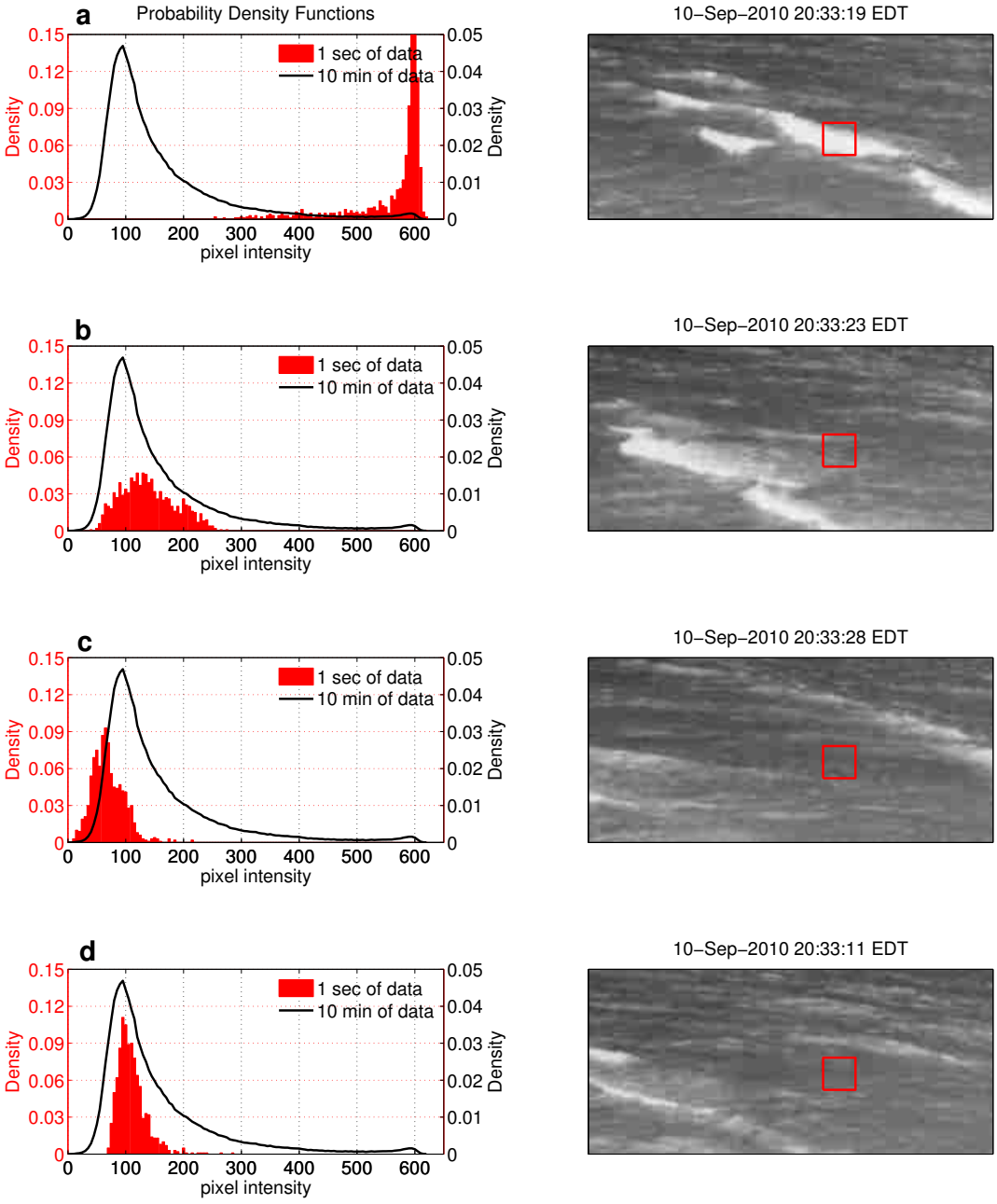

Figure 3.12: The variation of the pixel intensity pdf as a wave breaks and leaves behind residual foam. Panels in the right column show (a) a breaking wave, (b) residual foam, (c) cool, residual foam, and (d) a quiescent wave state. In the left column, the red pdf is the instantaneous distribution created from a 1-second record corresponding to the accompanying snapshot. The black pdf is the same in all panels and was created from a 10-minute record.

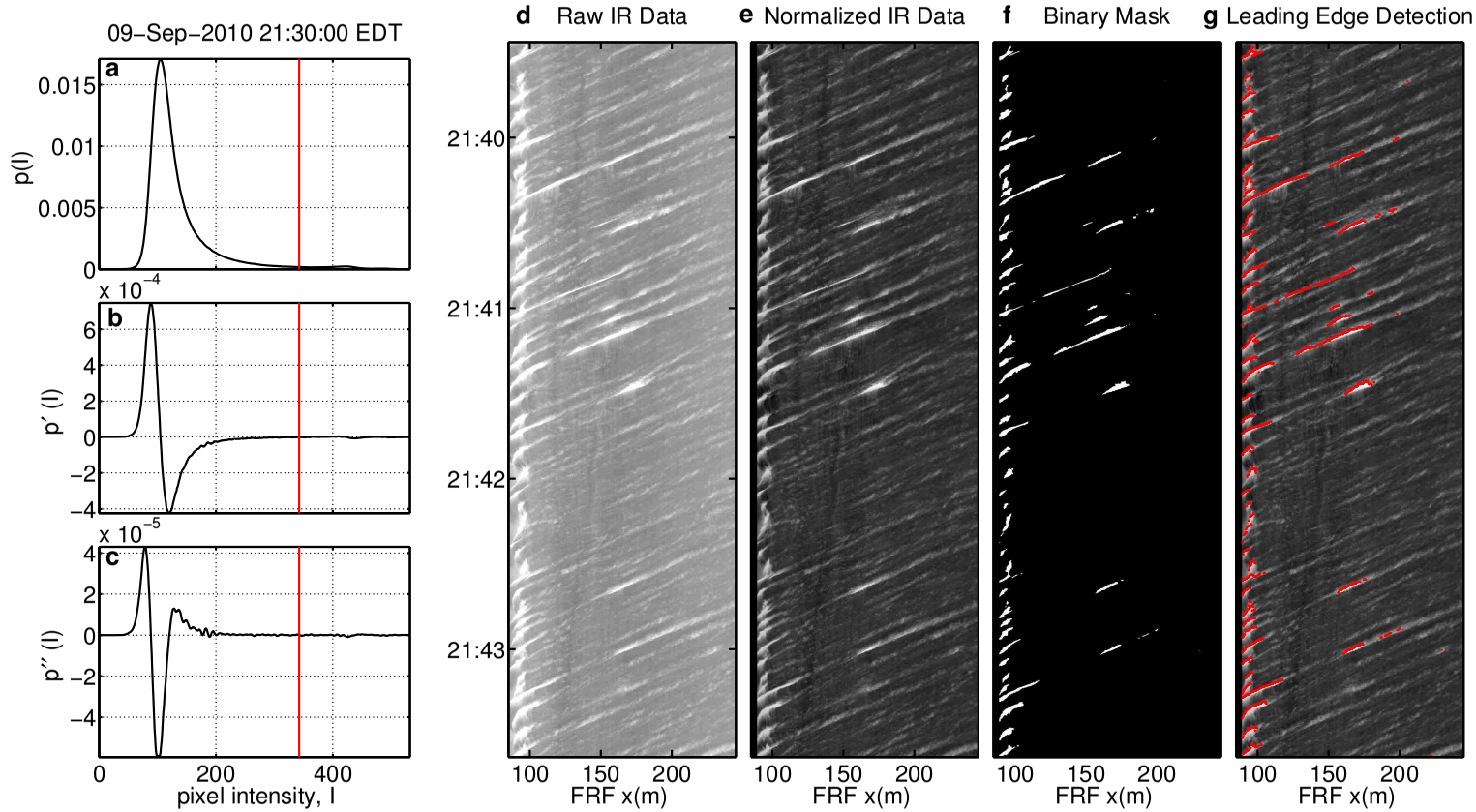

Figure 3.13: (a) Normalized bimodal distribution $p(\mathbf{I})$, (b) its first derivative $p'(\mathbf{I})$, and (c) its second derivative $p''(\mathbf{I})$, marked at threshold $\mathbf{I}_b$ with a red line. (d) Raw IR timestack, (e) normalized timestack, (f) thresholded binary mask, and (g) front-edge identification overlaid on normalized IR timestack, illustrate the detection algorithm's individual steps.

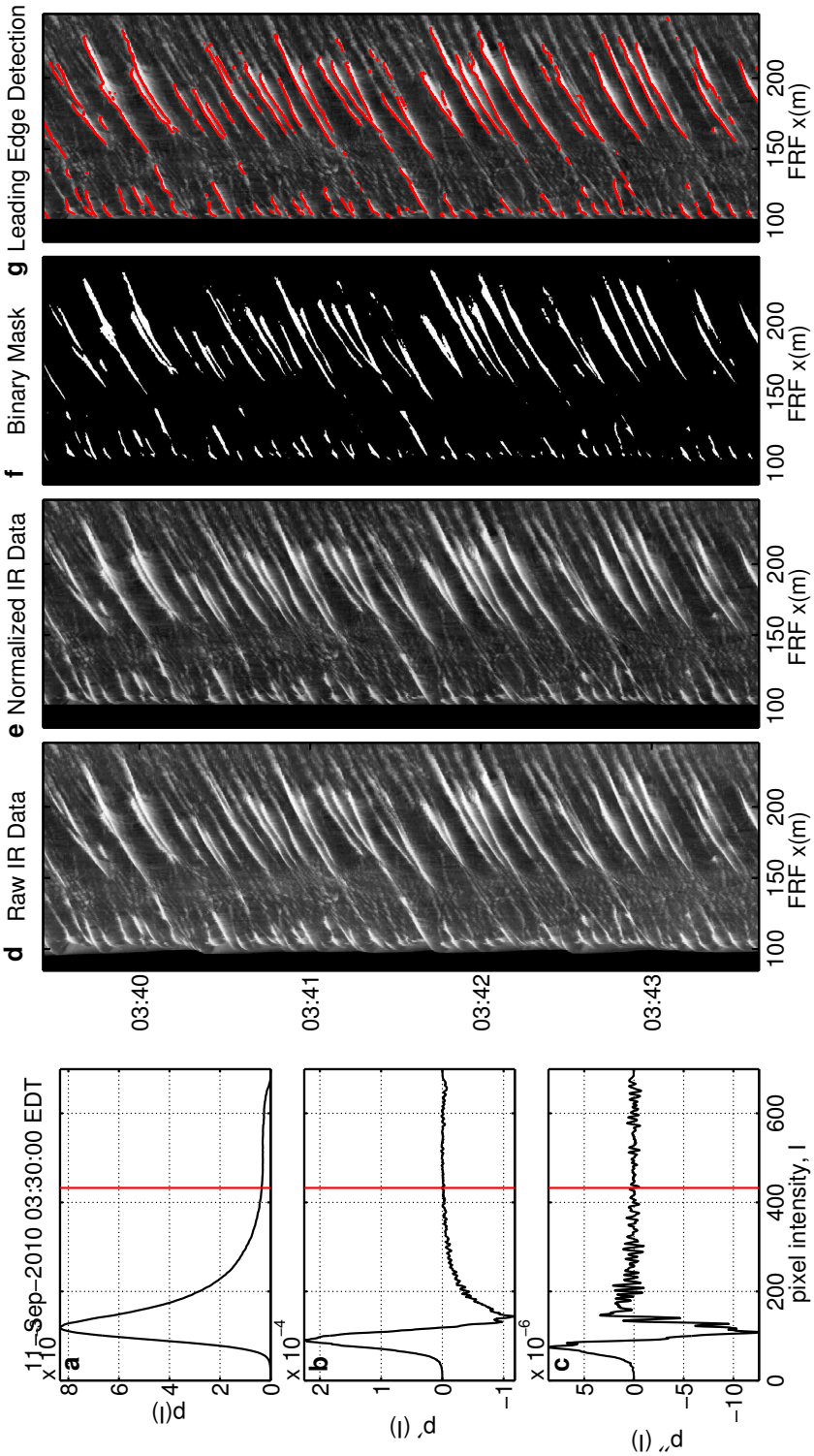

Figure 3.14: (a) Normalized unimodal-plateau distribution $p(\mathbf{I})$, (b) its first derivative $p'(\mathbf{I})$, and (c) its second derivative $p''(\mathbf{I})$, marked at threshold $\mathbf{I}_b$ with a red line. (d) Raw IR timestack, (e) normalized timestack, (f) thresholded binary mask, and (g) front-edge identification overlaid on normalized IR timestack, illustrate the detection algorithm's performance.

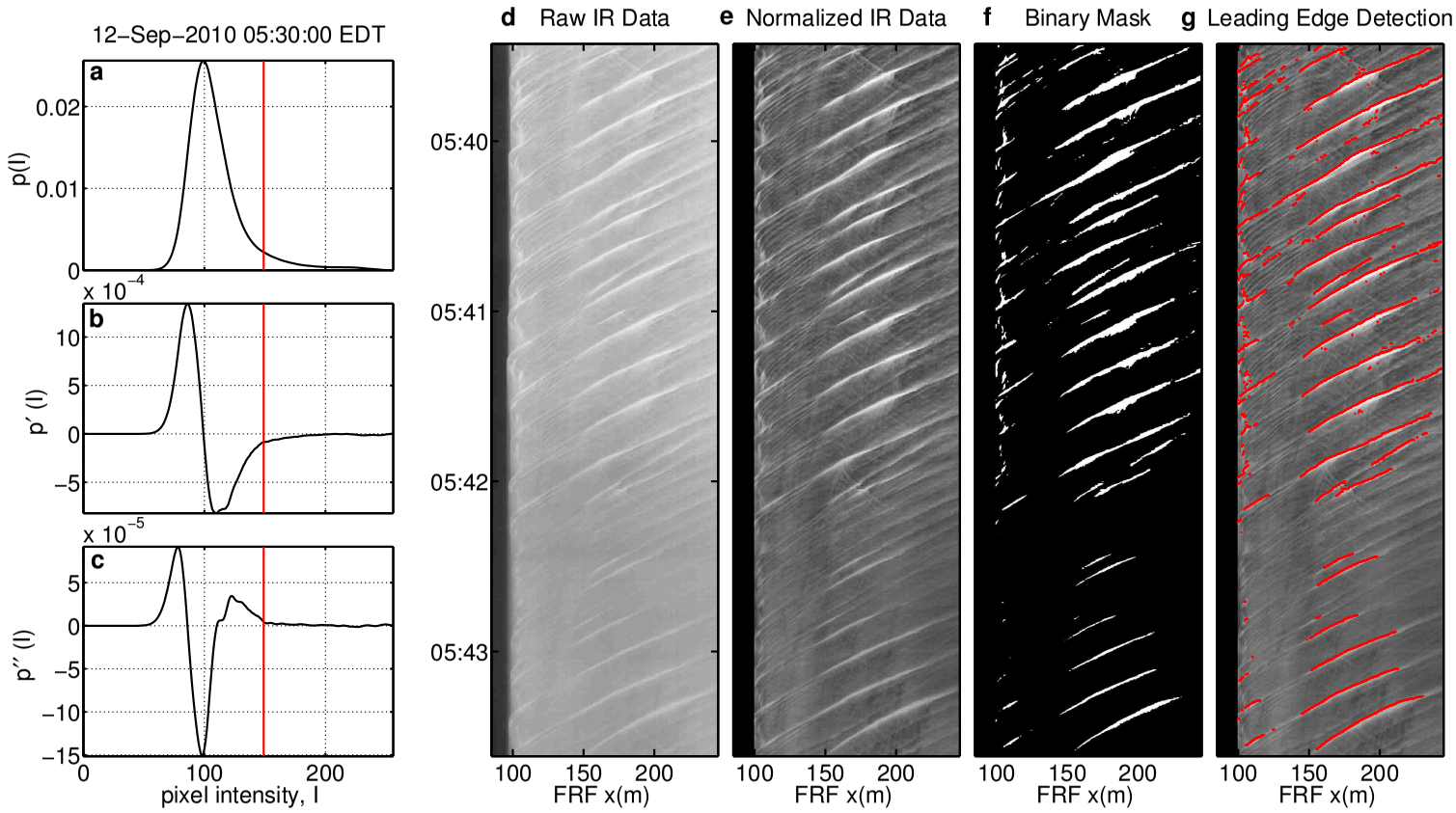

Figure 3.15: (a) Normalized unimodal and irregular distribution $p(\mathbf{I})$ (lack of second peak or long tail attributed to inhomogeneous background pixel intensity), (b) its first derivative $p'(\mathbf{I})$, and (c) its second derivative $p''(\mathbf{I})$, marked at threshold $\mathbf{I}_b$ with a red line. (d) Raw IR timestack, (e) normalized timestack, (f) thresholded binary mask, and (g) front-edge identification overlaid on normalized IR timestack, illustrate the detection algorithm's performance.

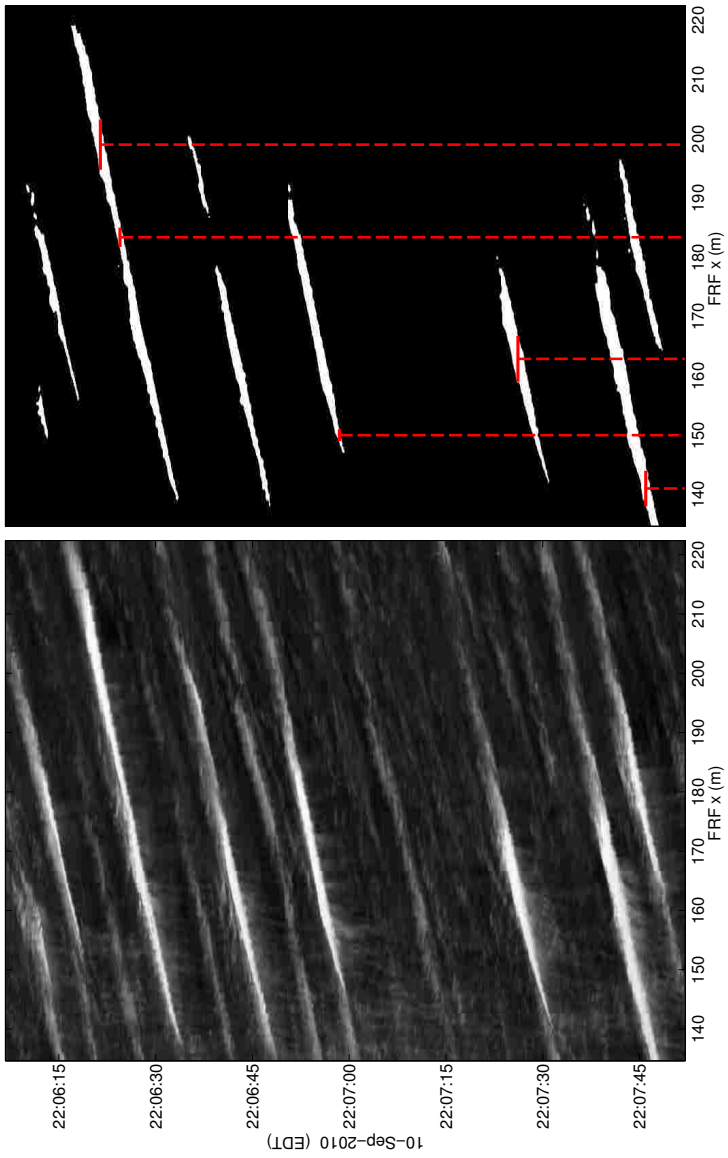

Figure 3.16: (right) Examples of the cross-shore projected roller length are marked on the binary mask corresponding to (left) the normalized IR timestack. The solid, horizontal red lines give the roller length measurement, and the dashed, vertical red lines indicate the cross-shore position associated with the given roller length.

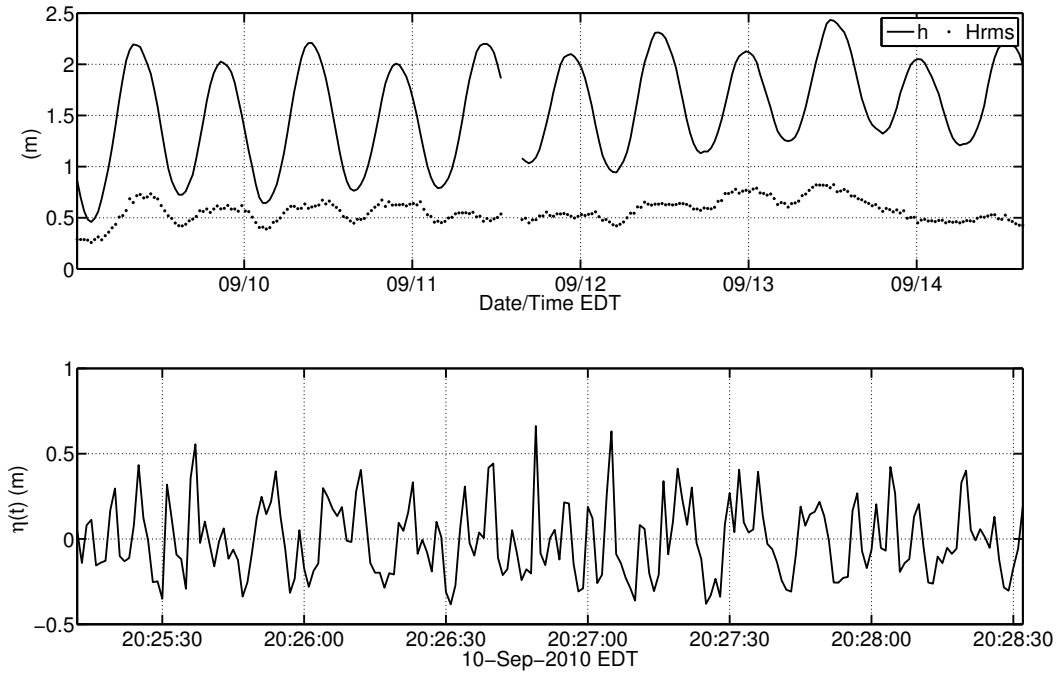

Figure 3.17: Time series over full experiment record of (top) mean sea level, h, and root-mean-square wave height, H_{rms}, as measured and estimated by the ADCP at x=190m. (bottom) 5-minute sea surface elevation time series, $\eta(t)$, from 09/10/2010.

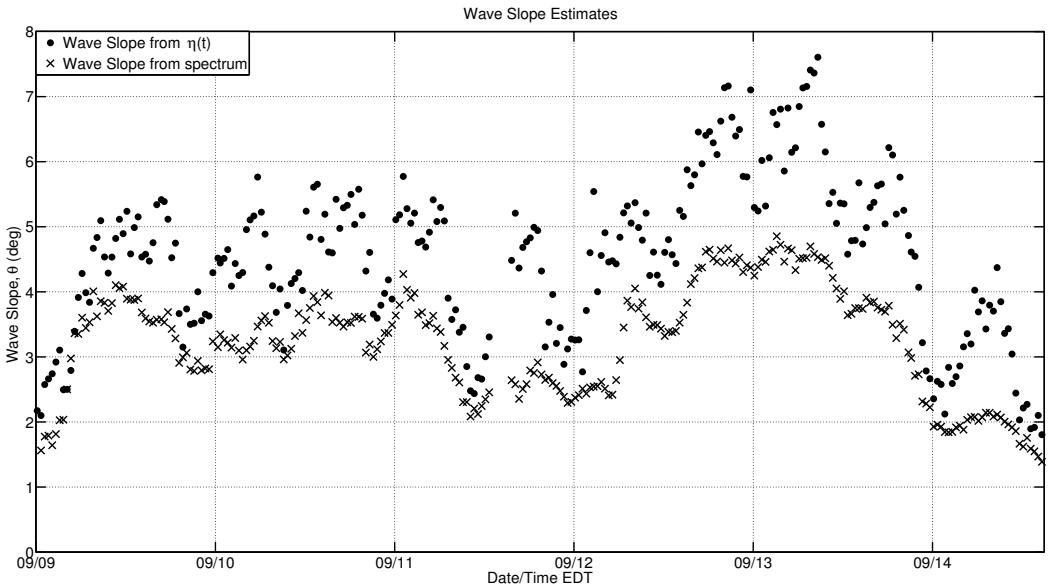

Figure 3.18: Time series-derived (circles) and spectrum-derived (x's) wave slope estimates. One estimate was made for each 18-minute data segment at the top of every half hour.

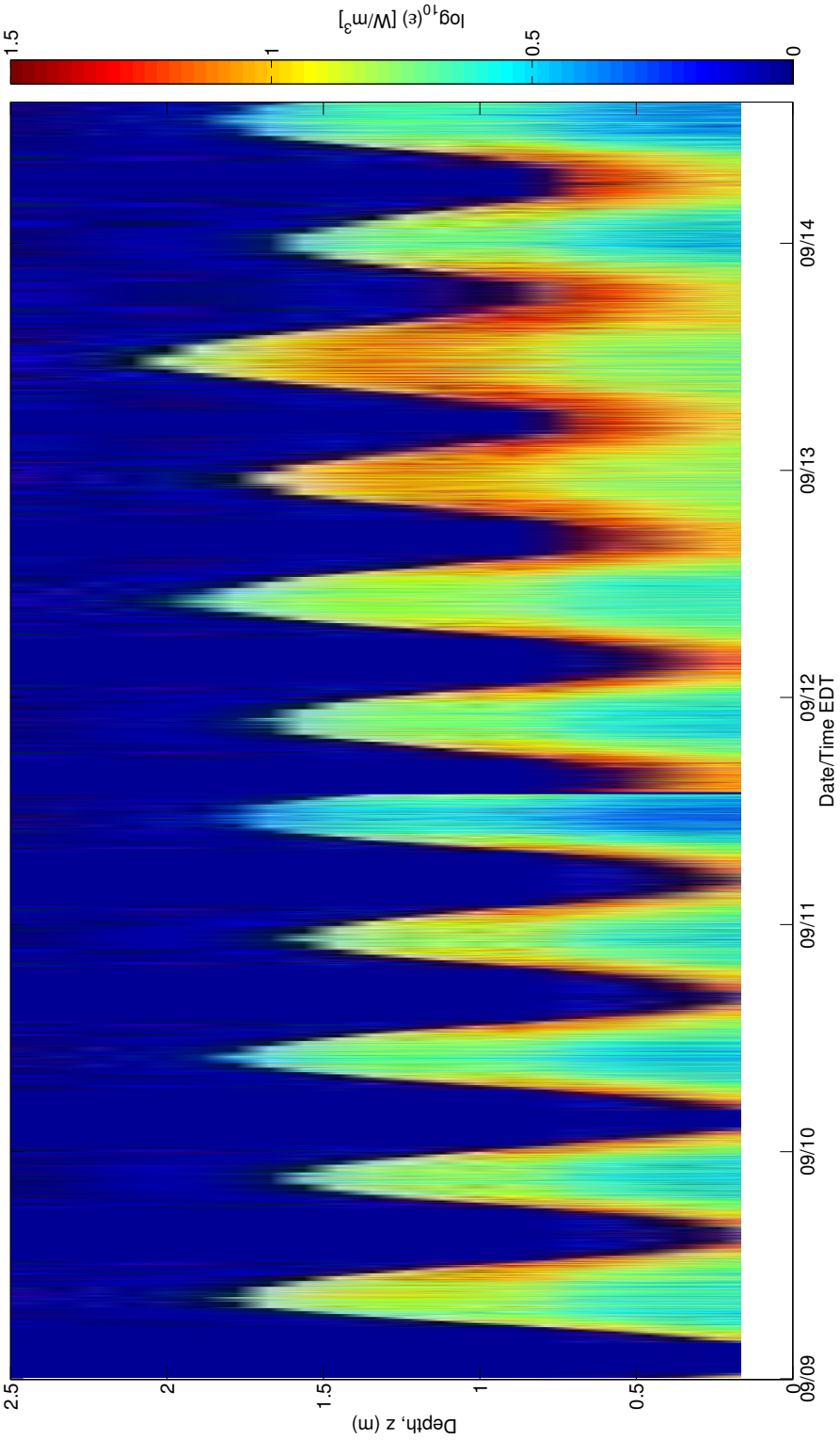

Figure 3.19: Depth profile time series of $\varepsilon_{\text{in situ}}$ estimated from the ADCP velocity data. Color scale in $\log_{10}$.

Chapter 4

RESULTS

The results are presented in two parts. First, the breaking detection algorithm produced breaking rate and roller length as direct results. Then, these parameters were used to evaluate the JB07 and D81dissipation rate estimates, respectively, yielding the geophysical results of interest. Discussion will focus more on the dissipation rate estimates than on the individual extracted parameters, however these direct results are novel and demonstrate the utility of IR-based wave detection in the surf zone, as well as its future potential applications.

4.1 Breaking rate

The timestack in Figure 4.1(a) displays breaking rate (3.28) as a function of cross-shore location over the experimental record. Also plotted are (b) water depth at x=190m (ADCP), (c) significant wave height (FRF 3-m ADCP), and (d) energy-weighted wave frequency (FRF 3-m ADCP) for context. The overall range of breaking rates, from $0s^{-1}$ to $0.22s^{-1}$, is consistent with the energy-weighted wave frequency of the incoming wave field, which ranged from $0.1s^{-1}$ to $0.25s^{-1}$ (Figure 4.1(d)). The f_e was calculated using the 1-D energy spectrum of the incoming wave field at x=245m (provided in FRF data from 3-m ADCP). Breaking occurred preferentially at the shoreline (x≈100m) and, at low tide, over the sand bar between x=160m and x=200m. The maximum IR-measured breaking rate of $0.22s^{-1}$ occurred at the shoreline, where the interquartile range was 0.11-$0.17s^{-1}$. Shoaling was sufficient for breaking over the sand bar during low tide, for which the interquartile range was 0.06-$0.10s^{-1}$. Almost no breaking occurred over the sand bar during high tide.

The region of increased breaking rate at low tide developed gradually over the bar as the water depth decreased (Figures 4.1(a, b)). The evolution of the pattern of breaking was best illustrated during the lower-low tide on 09/11/2010, expanded in Figure 4.2. As shown in Figure 4.2(b), breaking over the bar began at approximately 00:00 EDT at cross-

shore position x=160m. The cross-shore extent of the bar break increased as the water depth decreased, with the widest breaking region (∼40m) occurring at low tide at 03:30 EDT. As the water depth increased, the breaking region over the bar decreased. The scalloped onshore edge of the region of increased breaking over the bar may be due to the relationship between incoming wave heights, bathymetry, and a changing water level, as addressed further in the Discussion section. Figure 4.2(c) shows the transect bathymetry at 03:30 EDT (square symbol in Figure 4.2(a)). The sand bar is marked by a rise in bottom topography to a plateau with variations of approximately 0.2m about 1-m depth (at low tide). The maximum offshore extent of the bar break on 09/11/2010, which occurred at 03:30 EDT, was x≈215m, corresponding with a depth of approximately 1.4m. Shoreward of x≈110m, the transect bathymetry rises steeply to the shoreline. At high tide, when little to no breaking occurred over the bar, the region at the shoreline with rates of 0.175-0.2s^{-1} was wider than at low tide. The shore break region was narrower at low tide because the increased breaking over the bar decreased the wave energy that reached the shoreline.

While the magnitude of breaking rate varied, the patterns of breaking seen on 09/11/2010 were evident throughout the full record of breaking rate (Figure 4.1(a)). The magnitude of breaking rate over the bar at low tide appears positively correlated with H_{sig}. Lower H_{sig} (∼0.6m) after 12:00 EDT on 09/11/2010 and on 09/14/2010 correspond with peak breaking rates (over the bar) of 0.10s^{-1} and 0.08s^{-1}, respectively. Higher H_{sig} (∼0.75-1.25m) measured on 09/09/2010, 09/10/2010, 09/12/2010, and 09/13/2010, correspond with peak breaking rates between 0.09s^{-1} and 0.15s^{-1}. The position of the low tide bar break shifted shoreward approximately 10m over the course of the experiment. The implications of this migration will be discussed later.

4.2 Roller length

The roller length extracted from the IR timestack is the projected length, L_r'. The difference between the actual roller length and the projected roller length, or the misregistration, depends on wave slope and wave direction (Appendix A). The cross-shore position of the wave also affects the projection error because pixel resolution decreases with distance from the camera. The wave directions reported at the FRF 3-m ADCP varied between 49° and

121° from the positive y-axis. The camera look-direction was 38° from the positive y-axis. Therefore, the wave directions relative to the camera look-direction ranged from 11° to 83° with an interquartile range of 33°-61°. Wave slope estimates, made from the ADCP sea surface height time series (Figure 3.17) and the shallow water phase speed estimates, ranged from 2° to 8° over the length of the experiment (Figure 3.18). These slopes fall within the 2°-24° range reported in the literature (Duncan, 1981; Dally and Brown, 1995; Reniers and Battjes, 1997; Ruessink et al., 2001; Haller and Catalan, 2009). The ratio of L_r'/L_r, r in (3.18), was computed for the specified parameter space (cross-shore location, wave slope, and wave direction) using a geometric model, detailed in Appendix A. Figure 4.3 displays this ratio for wave slopes 0°-12° and wave direction 0°-75° at the cross-shore location of the ADCP (x=190m), where the D81, JB07, and *in situ* estimates will be compared. The minimum ratio is equal to 1, indicating that no projection error is incurred. The maximum ratio is approximately 7, which means that, at most, $L_r = L_r'/7$. The correction ratio is more sensitive to wave direction than wave slope and changes rapidly for wave directions greater than 60° (Figure 4.3). For wave slopes 2°-8° and wave directions below 60° (parameter space for 75% of the observed rollers), the correction ratio ranges from 1 to 4 (boxed in Figure 4.3). Therefore, in the extreme case, L_r could be incorrectly estimated by a factor of 4 (incorporated in the error calculations). Since ε_{D81} is proportional to L_r^2, a factor of 4 error in L_r yields a factor of 16 in ε_{D81}. However, ε_{D81} estimates span almost four orders of magnitude, so this error is relatively small (Figure 4.9).

After applying projection corrections to $L_r'(x,t)$ for each 18-minute timestack, 2-D histograms of L_r as a function of cross-shore position were computed. Figures 4.5(a-c) show examples of typical L_r distributions for low, medium, and high tide, respectively. In general, there are two peaks in L_r, one at the shoreline and another over the sand bar. The cross-shore extent of the bar break is greater than that of the shore break, and L_r reaches higher values over the bar than at the shore. Overall, the highest density of roller lengths occurs between L_r=0.5m and L_r=2.0m. The shore break exhibits roller lengths as great as 3.0m, with the average of approximately 0.75m. The position of the shore break shifts onshore as the tidal elevation increases, but its shape and density remain consistent throughout the different tidal stages. In Figure 4.5(a), a triangular pattern begins at x=245m with $L_r \approx$0.75m,

peaks at x=190m with L_r ≈3.5m, and decreases again to L_r ≈0.25m at x=150m. Within this triangular patch, the highest concentration of wave rollers occurs along its shoreward edge. This suggests that waves begin to break offshore and grow to some depth-limited L_r before decreasing again. In Figure 4.5(b), the bar break is sparser and narrower than at low tide, but maintains a similar triangular shape. When high tide is reached (Figure 4.5(c)), very little breaking occurs over the bar. There are so few breakers that individual breaker paths are distinguishable as continuous arcs of evolving L_r. This demonstrates the ability of IR imagery to examine wave roller evolution in the surf zone, although this topic will not be explored further here.

The timestack of occurence-weighted mean L_r, computed from the 2-D histograms, provides a summary of the variation of roller lengths with cross-shore position (Figure 4.6(a)). Figure 4.6 also shows (b) tidal elevation, (c) H_{sig}, and (d) peak and energy-weighted frequency. The large scale patterns are similar to those seen in the breaking rate timestack in Figure 4.1(a). However, roller length is noisier, varying from 1m to 4.5m at the shoreline and 2m to 5.5m over the bar. At the shoreline, roller lengths decrease from 4m to near 0m, which is physically consistent because the wave must decay almost completely at the shore. At the bar, roller lengths create a periodic pattern that mirrors the tidal elevation. This periodic pattern forms because waves can break farther offshore at low tide than at high tide, and the position of the critical breaking depth moves onshore as the tide rises. The strongest qualitative correlation with roller length is seen in f_p. When low frequency ($0.07s^{-1}$-$0.1s^{-1}$) swell approaches the shore, the roller lengths produced are longer than those resulting from sea waves ($0.15s^{-1}$-$0.2s^{-1}$).

4.3 Comparison of dissipation rate estimates

Using the binary masks of identified breaking waves, the energy dissipation rate was estimated by discretely summing Duncan's formulation over each roller length and scaling by record length (3.16). Figure 4.7 shows the cross-shore profile of $\varepsilon_{\mathrm{D81}}$ for the low, mid, and high tide examples from Figure 4.5. In all three cases, the interplay of roller length frequency and magnitude is apparent in the $\varepsilon_{\mathrm{D81}}$ estimate. The dissipation rate estimate from the shore break is similar across the three examples because, at the shoreline, break-

ing frequency and roller length vary little with tidal stage. $\varepsilon_{\mathrm{D81}}$ over the bar, however, decreases significantly from low to high tide from $\mathcal{O}(10)$ to $\mathcal{O}(10^{-1})$ W/m^2. Cross-shore profiles of wave energy dissipation rate were made from each 18-minute timestack, produced every half hour throughout the experiment (Figure 4.8). MSL at x=190m, H_{sig}, and peak and energy-weighted frequency are provided for reference in Figure 4.8(b-d). $\varepsilon_{\mathrm{D81}}$ is clearly modulated by the tide and, over the bar, displays strong qualitative correlation with H_{sig}. Correlation with H_{sig} is best illustrated during and just after the storm between 09/12/2010 and 09/14/2010. High H_{sig} ($\sim$1.2m) during the storm corresponds to values of $\varepsilon_{\mathrm{D81}}$ between 30 and 100W/m^2. When H_{sig} decreases to approximately 0.5m post-storm, $\varepsilon_{\mathrm{D81}}$ decreases to 10W/m^2 or less. A similar qualitative correlation is seen between $\varepsilon_{\mathrm{D81}}$ and f_{peak}. f_{peak} is approximately 0.07-0.08s^{-1} (low frequency swell waves) before and after the storm, but increases to 0.17-0.2s^{-1} (high frequency sea waves) during the storm.

To compare the remote estimate to the *in situ* estimate, a time series of $\varepsilon_{\mathrm{D81}}$ is extracted at x=190m (the cross-shore position of the ADCP). A first look at $\varepsilon_{\mathrm{D81}}(190,t)$ (Figure 4.9) shows that the maximum remote estimate of dissipation rate is just less than 100W/m^2 and the minimum is near 0W/m^2. The remote estimate fluctuates with tide, where (middle panel) low tide corresponds to (bottom panel) high breaking rate and large dissipation rate, and high tide corresponds to low breaking rate and small dissipation rate. The times when $\varepsilon_{\mathrm{D81}}(190,t)$ drops to very low values correspond to times when the breaking rate is near zero. Therefore, the remote estimate is based on observation of very few waves, which means it should be small and could potentially be noisy. The dynamic range of the remote estimate spans almost four orders of magnitude, but decreases on 09/12/2010 and 09/13/2010 due to the storm. Specifically, storm conditions increase breaking rate during high tide, when breaking is usually low, which raises the minimum $\varepsilon_{\mathrm{D81}}(190,t)$ during this period.

Figure 4.10 includes the time series of the *in situ* turbulent dissipation rate estimate with error bands (95% CI). The turbulent dissipation rate estimate, $\varepsilon_{\mathrm{in\ situ}}$, exhibits similar tidal fluctuations to $\varepsilon_{\mathrm{D81}}(190,t)$, and also has comparable magnitude to $\varepsilon_{\mathrm{D81}}(190,t)$, but maintains a smaller dynamic range. The dashed regions mark times when the *in situ* estimate is at or below its noise floor of approximately 3-5W/m^2 (Thomson, personal communication), and the data gap on 09/11/10 was due to equipment maintenance (battery replacement and

data download). A one-to-one comparison is not expected between the wave dissipation rate estimate, $\varepsilon_{\mathrm{D81}}(190,t)$, and the turbulent dissipation rate estimate, $\varepsilon_{\text{in situ}}$, because the estimate from the ADCP includes other sources of dissipation in addition to wave breaking (addressed further in Discussion section). The scatter plot of $\varepsilon_{\mathrm{D81}}(190,t)$ versus $\varepsilon_{\text{in situ}}$, in Figure 4.11, shows that the remote and *in situ* estimates are positively correlated. There is a clustering about the one-to-one line for large values of $\varepsilon_{\mathrm{D81}}(190,t)$. However, for small values of $\varepsilon_{\mathrm{D81}}(190,t)$ (near zero breaking rate), $\varepsilon_{\text{in situ}}$ is much higher than what would be predicted from the one-to-one line. This scatter plot suggests two regimes: one when wave breaking dominates the dissipation rate estimate, and one when breaking rate is low and other sources might dominate the dissipation rate estimate or the *in situ* estimate is limited by instrument noise.

As a further comparison to *in situ* data, the cross-shore profile of $\varepsilon_{\mathrm{D81}}$ (Figure 4.8) is discretely integrated,

$$E_{\mathrm{D81}} = \sum_{x=\text{shore}}^{x=245\text{m}} \varepsilon_{\mathrm{D81}}(x)\Delta x, \tag{4.1}$$

and compared to the bulk energy flux entering the surf zone at the offshore edge of the transect (Figure 4.12). As described in Section 2.2, energy dissipation due to wave breaking is one of several sinks for wave energy fluxed into the surf zone. As such, E_{D81} is expected to be less than the bulk energy flux, $\mathcal{F}$. The bulk energy flux is defined as the wave energy multiplied by the group velocity. Here, $\mathcal{F}$ was estimated by multiplying the 1-D energy density spectrum, reported by the FRF 3-m ADCP, by the frequency-dependent group velocity and integrating over all frequencies:

$$\mathcal{F} = \int E(f)\cdot c_g(f)df, \quad \text{where} \tag{4.2}$$

$$E(f) = \frac{1}{8}\rho g H^2(f), \quad \text{and} \tag{4.3}$$

$$c_g(f) = \frac{1}{2}\left(1+\frac{2kh}{\sinh(2kh)}\right)\left(\frac{g}{2\pi f}\right)\tanh(kh).$$

Estimating $\mathcal{F}$ from the FRF 3-m ADCP assumes that the wave were propagating shore-normal. Obliquely propagating waves would transmit less energy cross-shore, so the estimate of bulk energy flux in Figure 4.12 is an upper bound on the true bulk energy flux at x=245m. $\mathcal{F}$ (Figure 4.12) does not vary with the tide, rather it fluctuates around 2×10^3W/m due

to fairly consistent, slowly varying dominant wave height, H_{sig}, throughout the experiment (Figure 3.3). E_{D81} is more strongly tied to the tidal fluctuations in breaking rate, but lies mostly within one order of magnitude of $\mathcal{F}$. E_{D81} is less than $\mathcal{F}$ for most of the experimental record, as expected. However, E_{D81} surpasses $\mathcal{F}$ briefly on 09/10/2010 and repeatedly during the storm on 09/12/2010 and 09/13/2010 (addressed in Discussion section).

The Duncan and JB07 dissipation rate estimates agree well (Figure 4.13). Both estimates are 180° out of phase with tidal fluctuations. The greatest differences between $\varepsilon_{\mathrm{D81}}$ and $\varepsilon_{\mathrm{JB07}}$ occur during the storm, and the lowest values of $\varepsilon_{\mathrm{D81}}$ and $\varepsilon_{\mathrm{JB07}}$ occur at times when the breaking rate is near zero ($< 0.001\mathrm{s}^{-1}$). The remarkable agreement between these two independent estimates is further illustrated in Figure 4.14. $\varepsilon_{\mathrm{D81}}$ and $\varepsilon_{\mathrm{JB07}}$ are positively correlated. The estimates exhibit a near one-to-one relationship, but with an offset that indicates a systematically higher dissipation rate predicted by $\varepsilon_{\mathrm{JB07}}$.

4.4 Figures

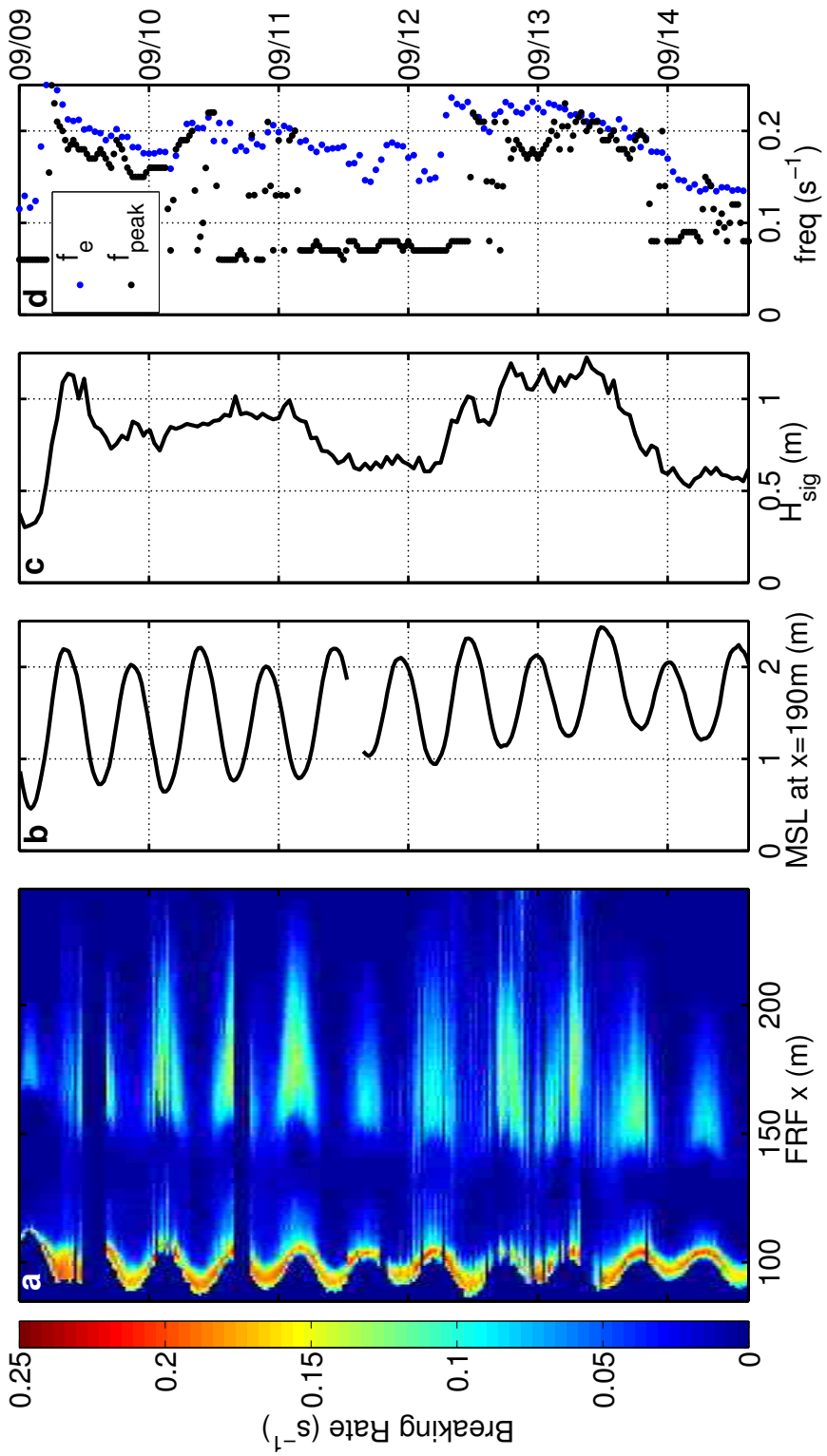

Figure 4.1: (a) Timestack of breaking rate (Hz) along the cross-shore transect for he full experiment record. (b) Mean sea level (m) time series at cross-shore location x=190m as measured by ADCP on the sand bar. (c) Significant wave height (m) time series measured by the FRF 3-m ADCP. (d) Peak (black) and energy-weighted (blue) wave frequency (Hz) from the FRF 3-m ADCP.

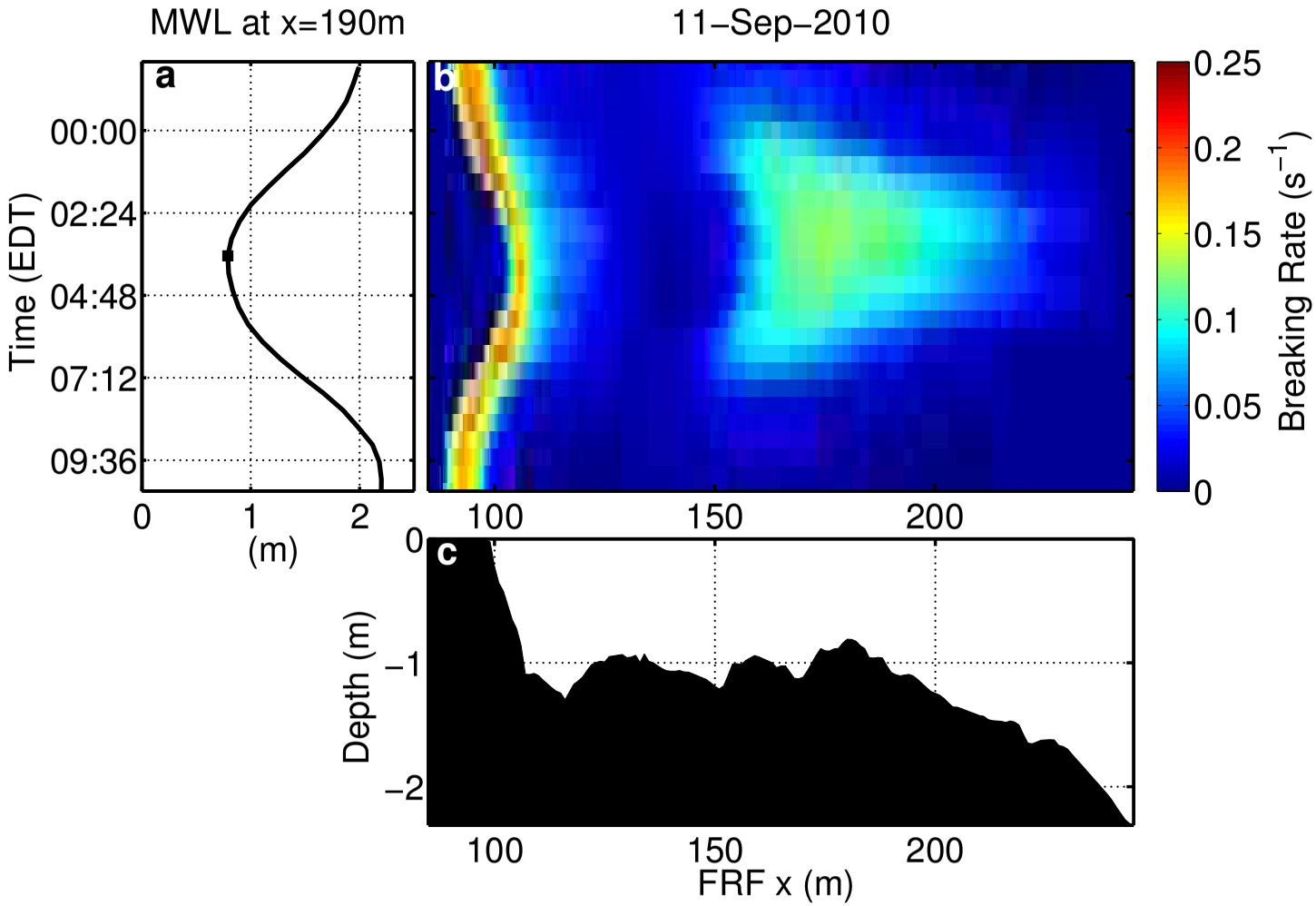

Figure 4.2: Expansion of one tidal cycle from the breaking rate timestack shown in Figure 4.1. (a) Example of mean sea level (m) on 09/11/2010. (b) Breaking rate (Hz) timestack along cross-shore transect for tidal cycle shown in (a). (c) Transect bathymetry adjusted for tidal elevation corresponding to the time marked with a black square in (a).

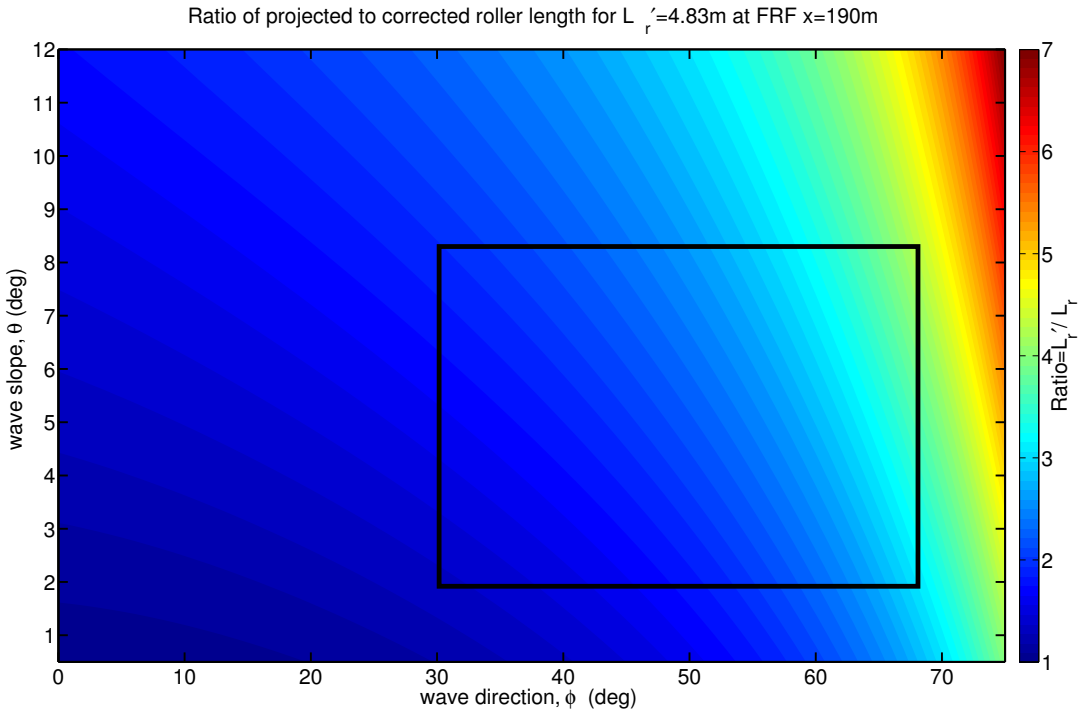

Figure 4.3: Ratio of projected to corrected roller length (L_r'/L_r) as a function of wave slope θ (y-axis) and wave direction ϕ (x-axis). This example provides the correction factor specific to a breaking wave with L_r' equal to 4.83m observed at cross-shore location x=190m (average $L_r'(x = 190, t)$).

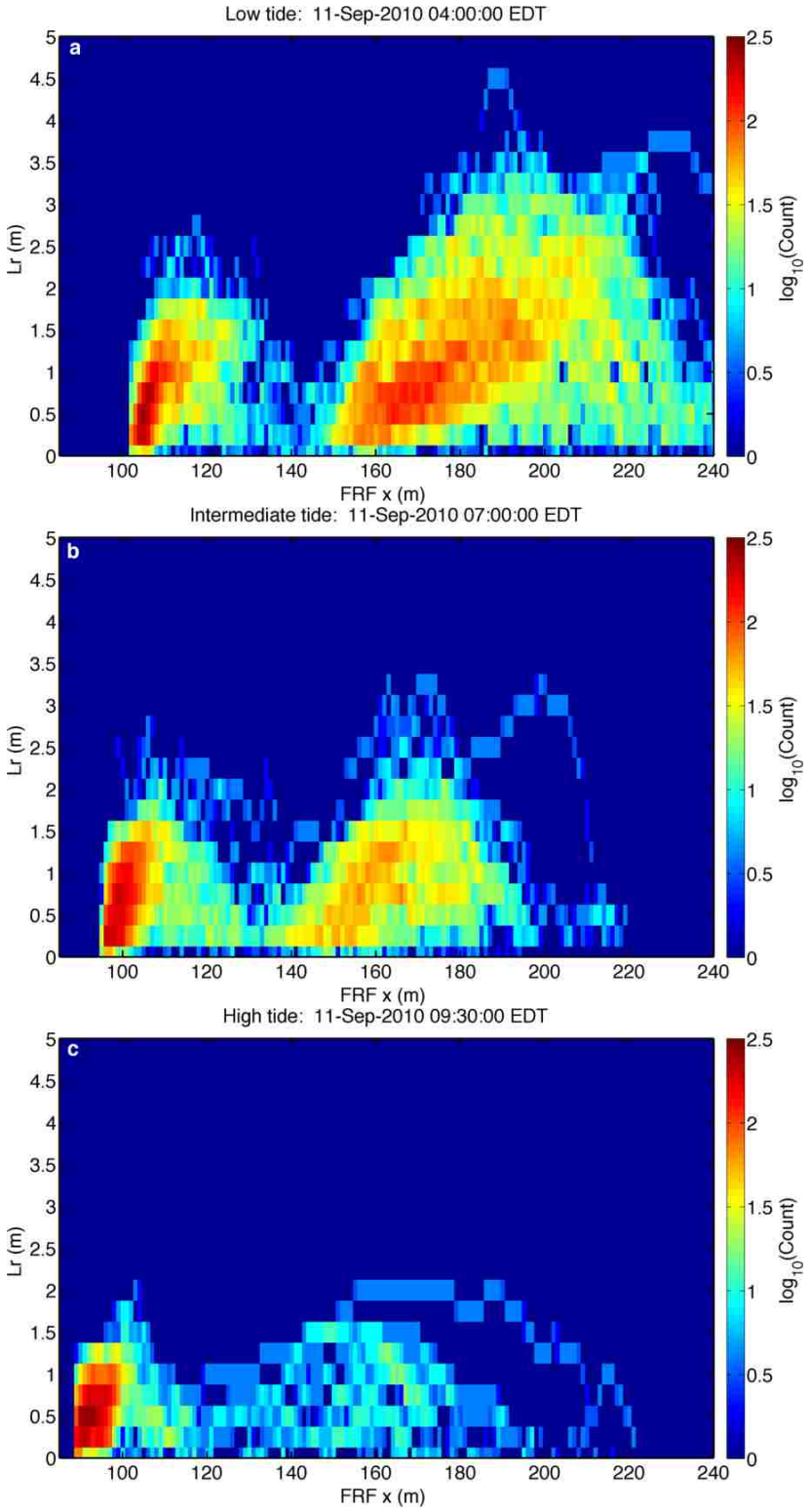

Figure 4.5: 2-D histograms of corrected roller length, L_r (m), as a function of cross-shore position. Examples shown from (a) low tide, (b) intermediate tide, and (c) high tide on 09/11/2010.

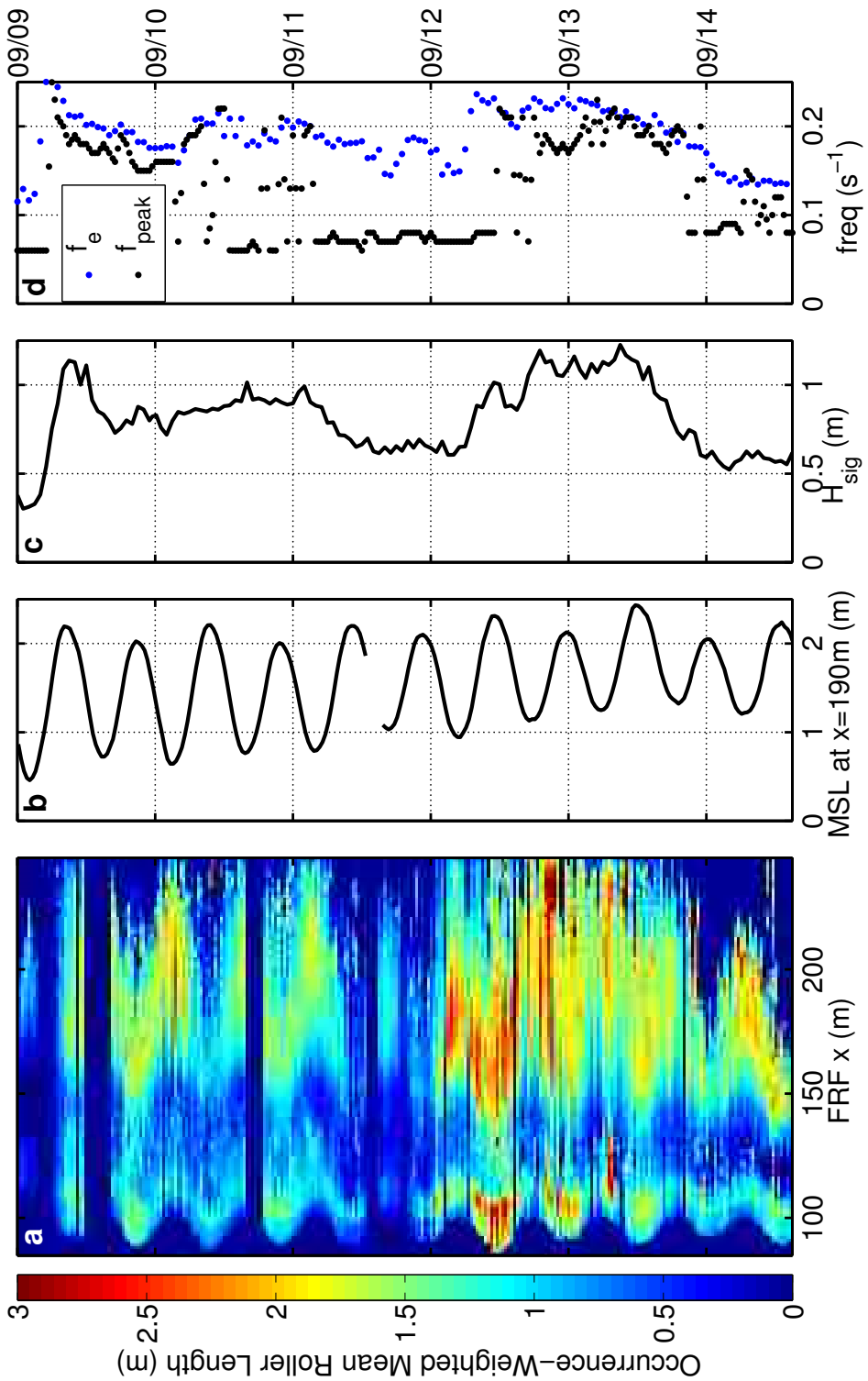

Figure 4.6: (a) Timestack of the weighted mean roller length (m) along the cross-shore transect for the full experiment record. (b) Mean sea level (m) time series at cross-shore location x=190m as measured by ADCP on the sand bar. (c) Significant wave height (m) time series measured by the FRF 3-m ADCP. (d) Peak (black) and energy-weighted (blue) wave frequency (Hz) from the FRF 3-m ADCP.

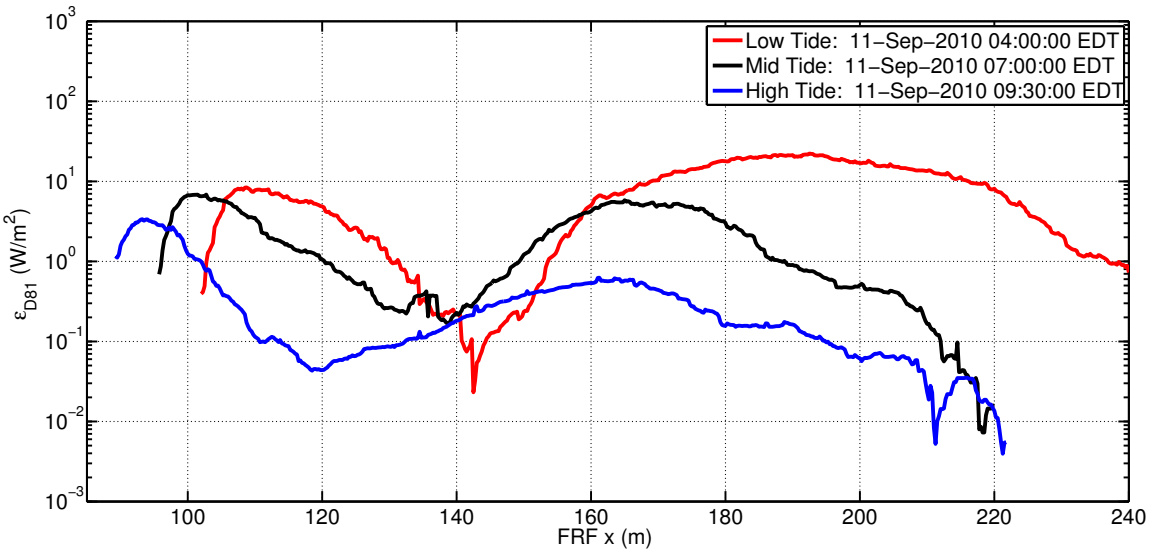

Figure 4.7: Cross-shore profiles of ε_{D81} computed from the roller lengths represented in the 2-D histograms in Figure 4.5. Examples shown from low tide, intermediate tide, and high tide on 09/11/2010.

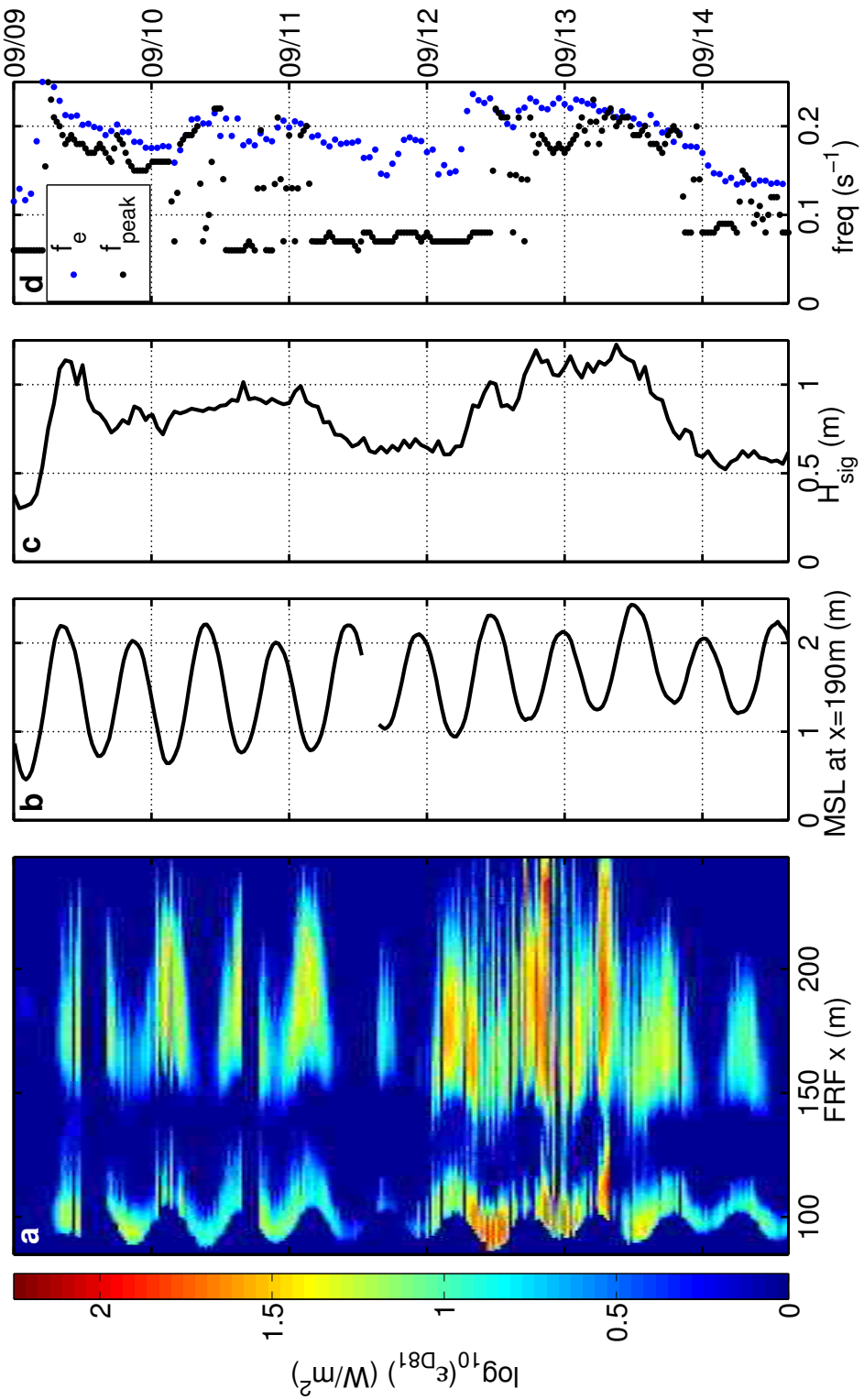

Figure 4.8: (a) Timestack of average dissipation rate (W/m^2), as estimated using Duncan's parameterization, along the cross-shore transect for the full experiment record. (b) Mean sea level (m) time series at cross-shore location x=190m as measured by ADCP on the sand bar. (c) Significant wave height (m) time series measured by the FRF 3-m ADCP. (d) Peak (black) and energy-weighted (blue) wave frequency (Hz) from the FRF 3-m ADCP.

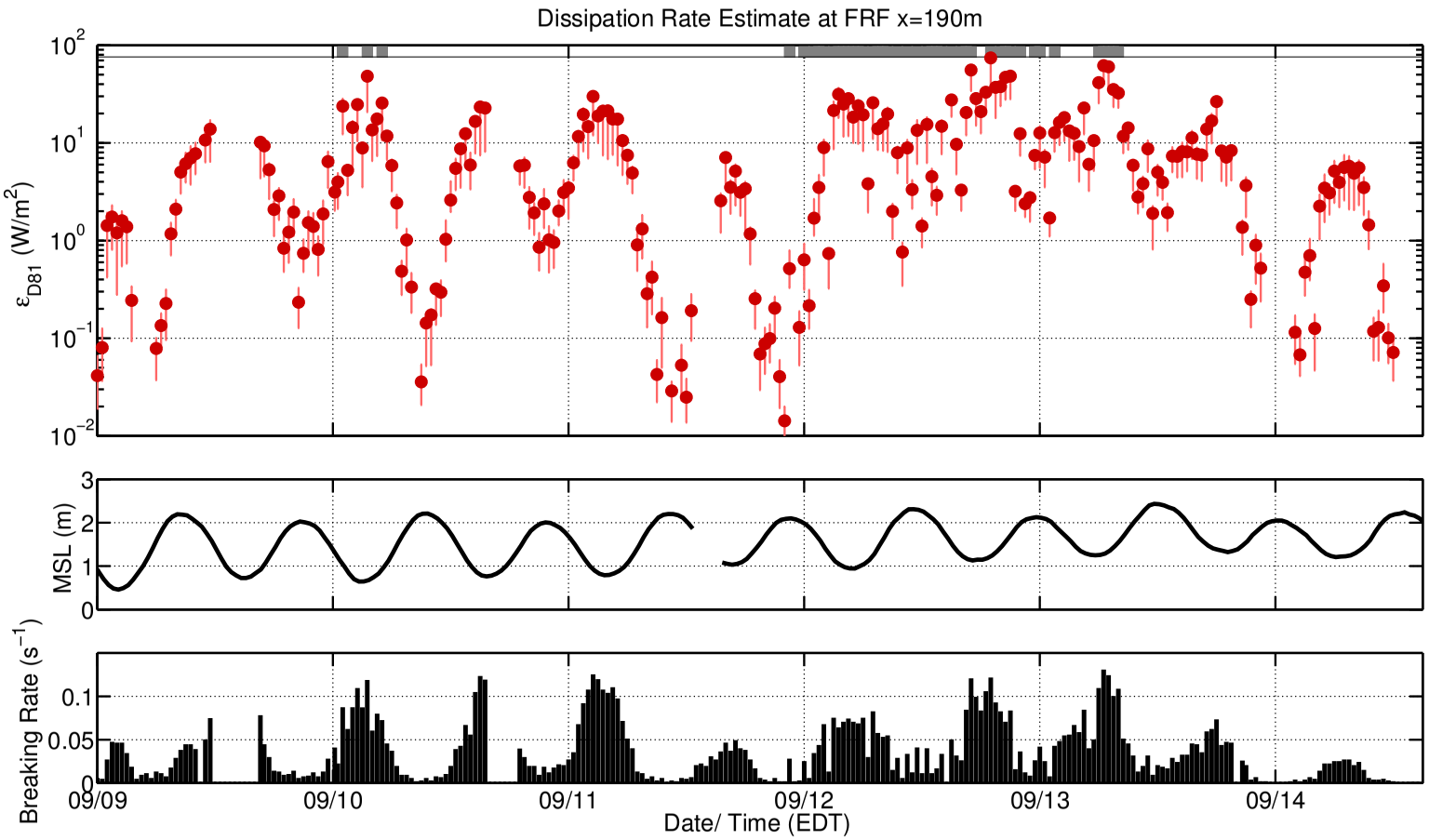

Figure 4.9: (top) Remotely-derived dissipation rate estimate (W/m^2) with error bars from transect position x=190m for the full experiment record. Dark gray bars along the top of the plot indicate times when secondary methods were employed in the detection algorithm. (middle) Mean seal level (m) times series from ADCP at x=190m. (bottom) Breaking rate (Hz) time series from x=190m in the timestack in Figure 4.1.

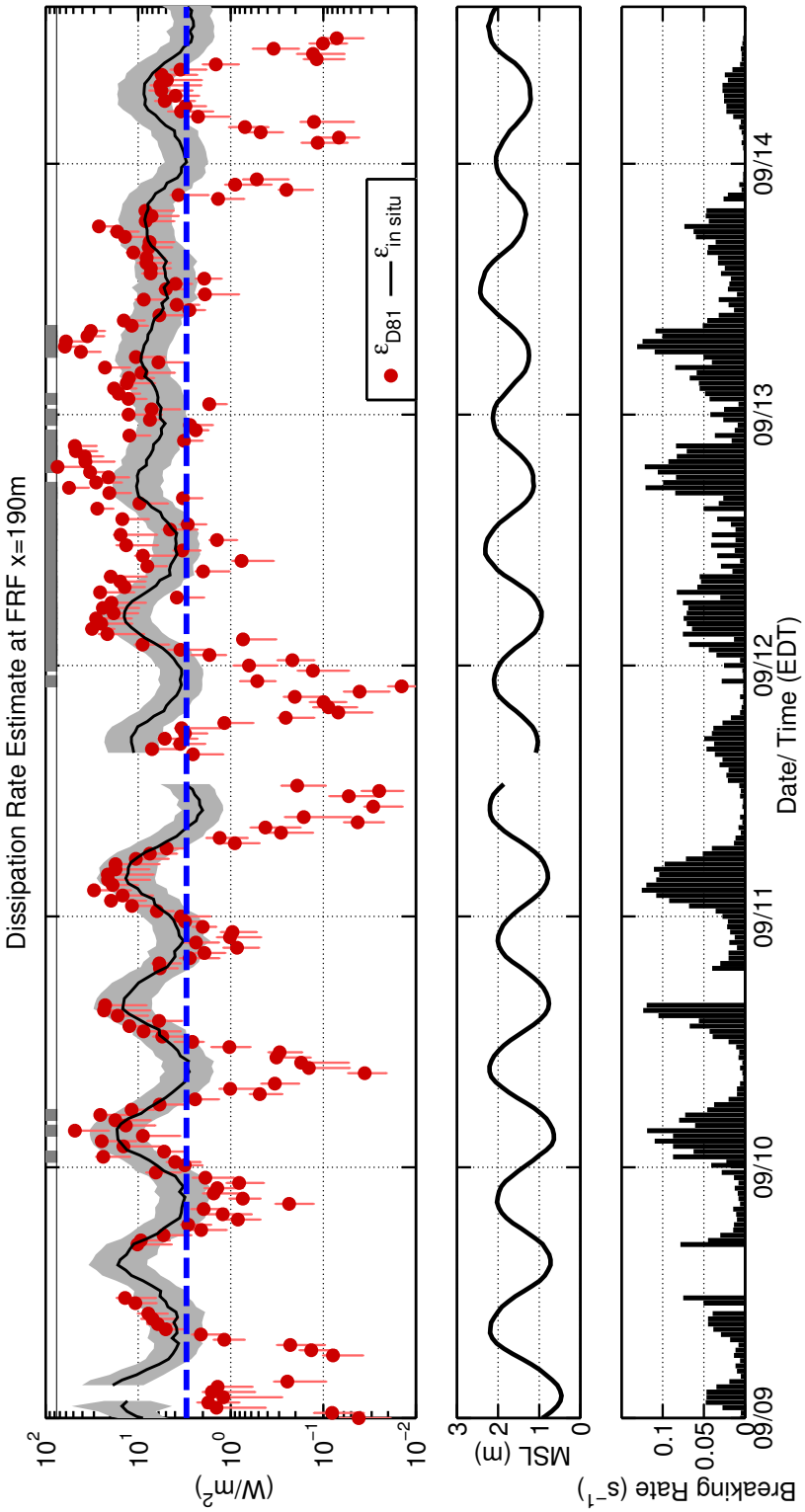

Figure 4.10: (top) Remote dissipation rate estimate (W/m^2) from Figure 4.9 compared with *in situ* TKE dissipation rate estimate (black curve with gray error band). The noise floor of the *in situ* estimate is marked by the dashed blue line. (middle) Mean seal level (m) times series from ADCP at x=190m. (bottom) Breaking rate (Hz) time series measured at x=190m.

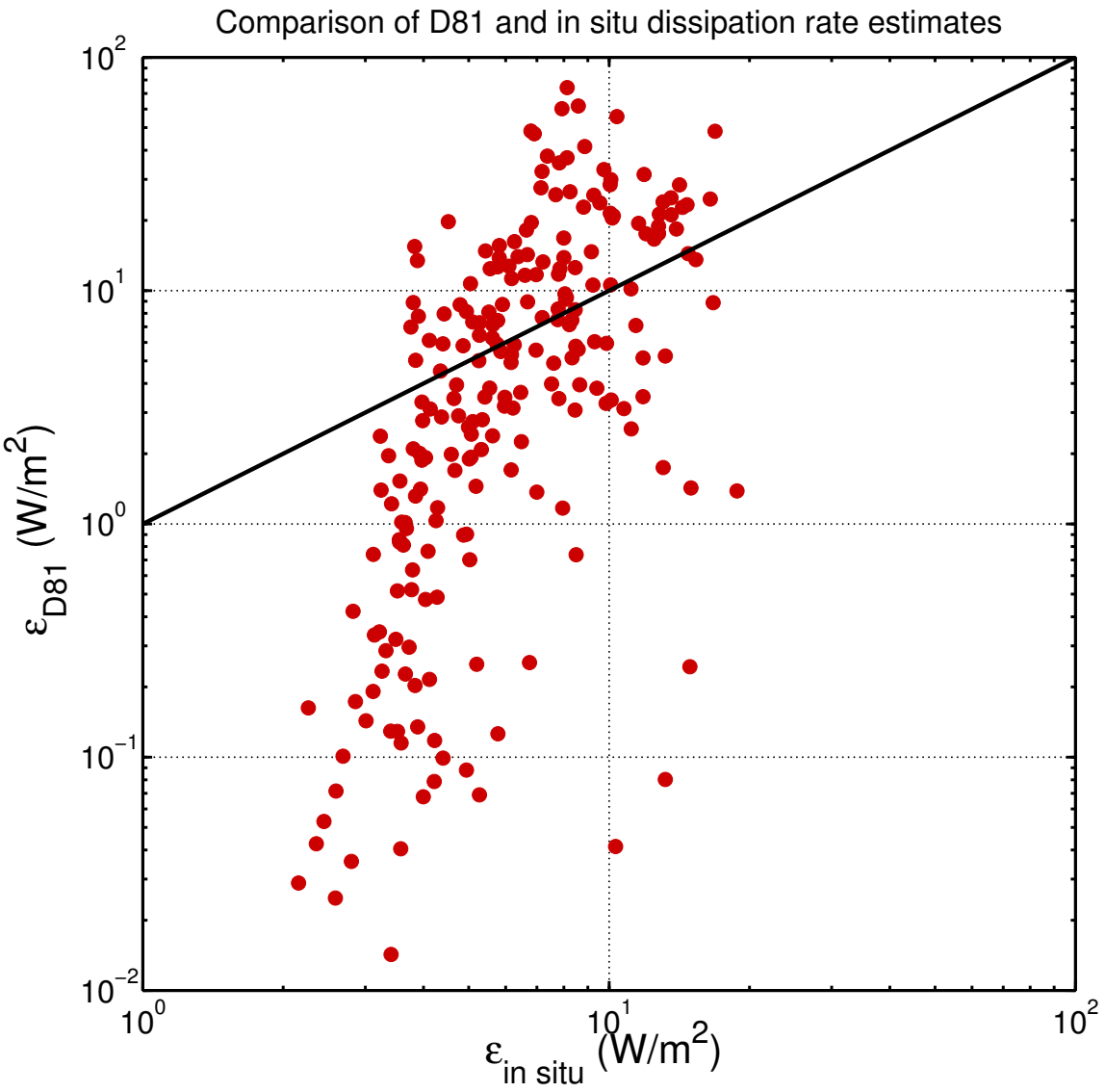

Figure 4.11: Scatter plot of remote (Duncan) versus *in situ* dissipation rate estimates. One-to-one line plotted in black for comparison.

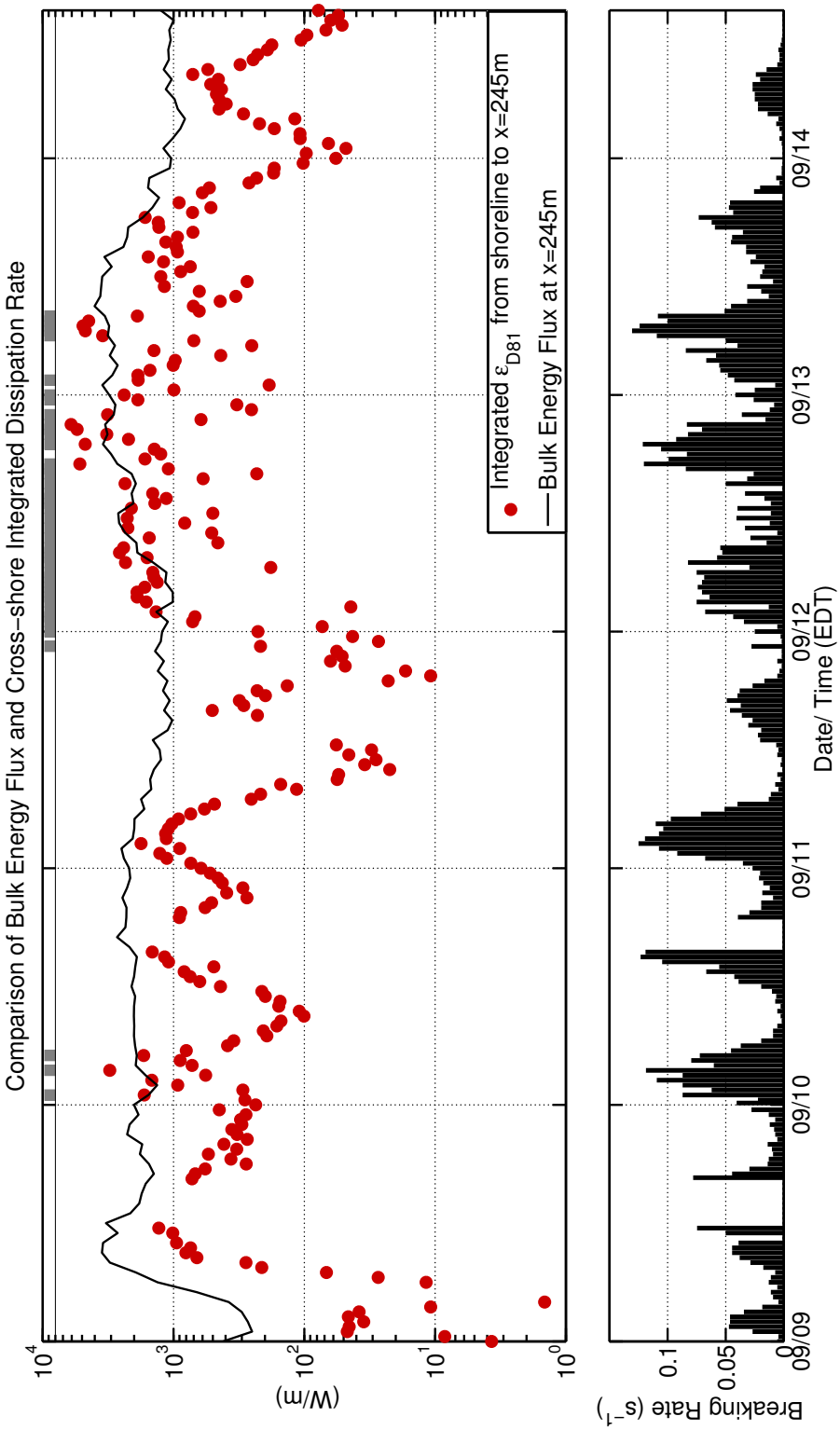

Figure 4.12: (top) Time series of cross-shore integrated removed dissipation rate estimate (red circles) and bulk energy flux through x=245m (black curve). x=245m is the offshore extent of the IR transect. (bottom) Breaking rate (Hz) time series measured at x=190m.

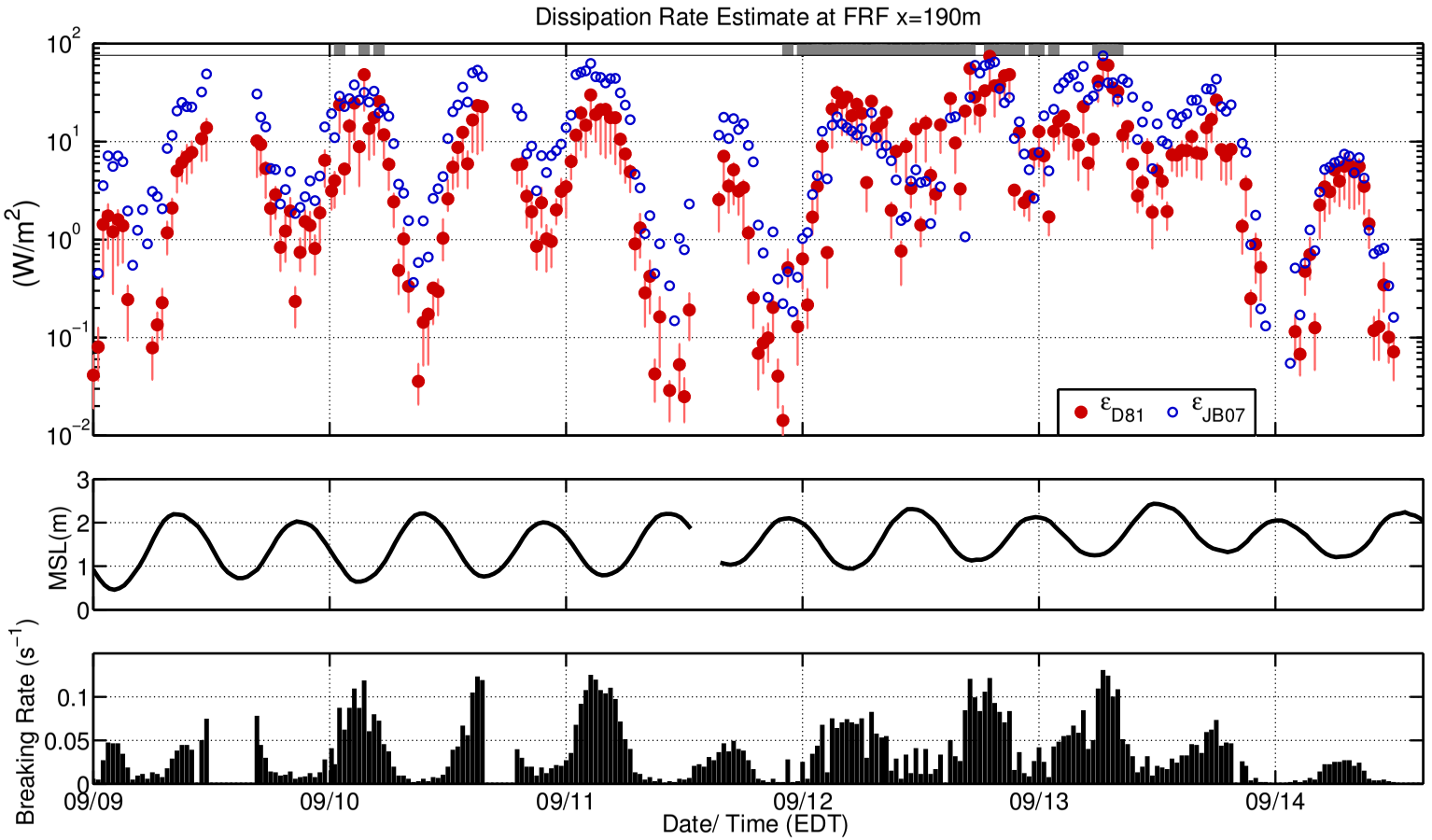

Figure 4.13: (top) Time series comparison of remote dissipation rate estimates, Duncan (filled, red circles) and JB07 (open, blue circles), at cross-shore position x=190m. (middle) Mean seal level (m) times series from ADCP at x=190m. (bottom) Breaking rate (Hz) time series measured at x=190m.

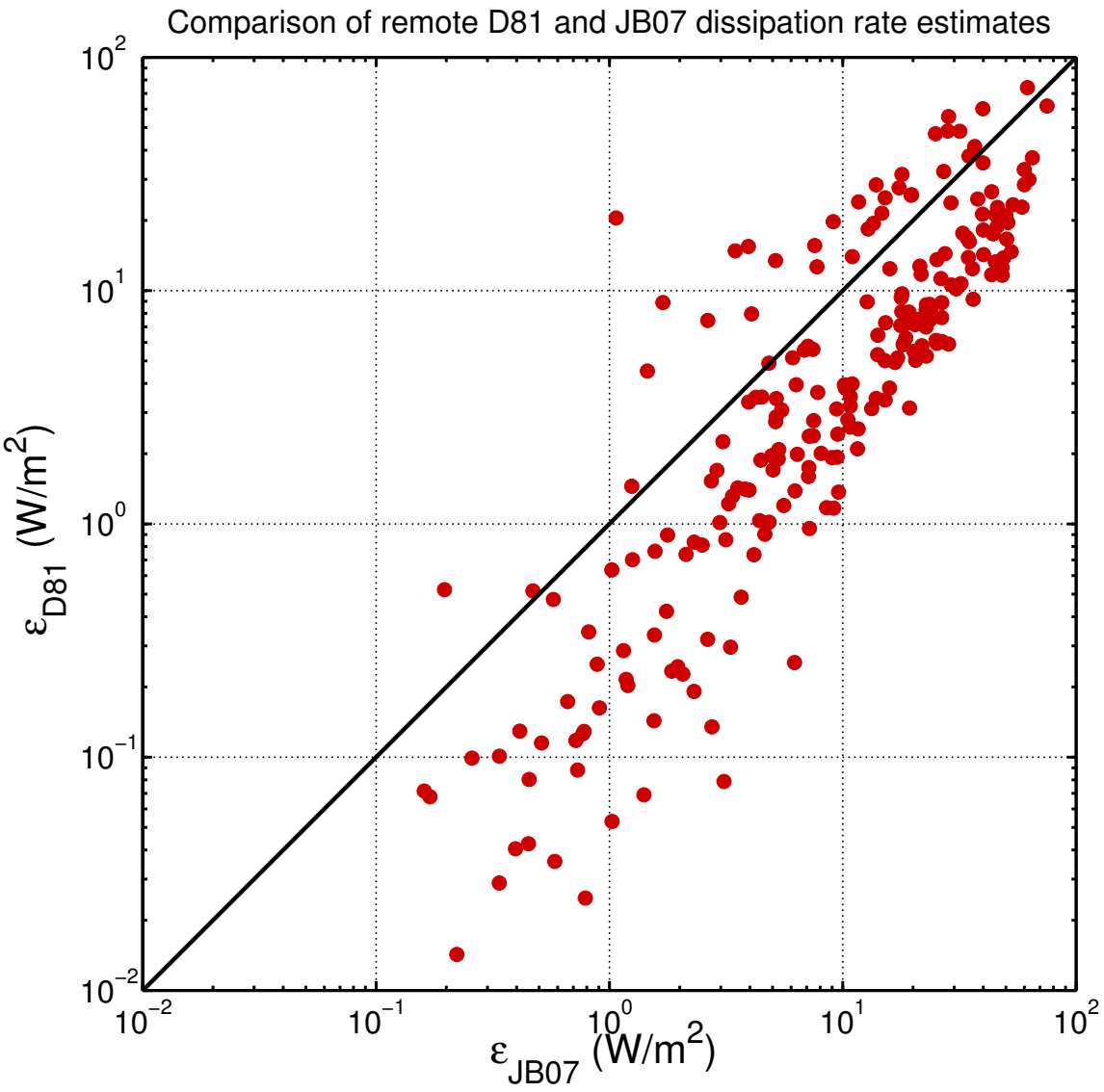

Figure 4.14: Scatter plot of remote Duncan versus JB07 dissipation rate estimates. One-to-one line plotted in black for comparison.

Chapter 5

DISCUSSION

5.1 Detection algorithm

By exploiting the distinct signatures of active and residual foam in IR imagery, breaking wave crests were isolated and roller length was measured. Roller length was then used to evaluate Duncan's wave energy dissipation rate model. The normalization of pixel intensity for each timestack resulted in a thresholding algorithm that consistently identified breaking crests, over the entire 18-minute record and along the full cross-shore transect, for 210 out of 253 timestacks. For these 210 timestacks, the breaking rates calculated over the bar and at the shoreline from the binary mask were comparable to the peak frequency measured by the FRF 3-m ADCP. Researchers at Oregon State University confirmed similar breaking rates during SZO 2010 in visual imagery via manual (human-eye) breaker detection (personal communication with Adam Keen). For the remaining 43 timestacks, secondary processing (discussed in Methods section) was necessary to correct for inhomogeneous background pixel intensity, usually a result of inhomogeneous cloud coverage. Storm conditions on 09/12/2010 and 09/13/2010 elevated the breaking rate, sometimes resulting in a merging of subsequent breaking waves. Actively breaking crests were correctly identified during this time, but the merged crests caused underestimation of the breaking rate and overestimation of the roller length. This effect was seen almost exclusively at the shoreline, and would result in increased dissipation rate estimates due to the dependence on L_r^2. Binary masks on which normalization and secondary processing failed were excluded from the results.

A sensitivity analysis was performed on the three timestacks from Figures 3.13, 3.14, and 3.15, to test the effect of a change in threshold value for actively breaking waves. These three examples were chosen for sensitivity analysis because they are representative of the full dataset. Figure 3.13 demonstrates the typical bimodal intensity distribution. Figure 3.14 shows a unimodal-plateau intensity distribution. Figure 3.15 illustrates how uneven cloud

coverage results in inhomogeneous background intensity, which complicates the choice of a single threshold to be used over the entire timestack. The ratio of the number of pixels identified to the total number of pixels in the timestack, or the percent coverage (PC), was used as a sensitivity assessment statistic. If a small change in threshold intensity, $\mathbf{I}_b$, produces a small change in PC, the detection algorithm is stable, but if a small change in $\mathbf{I}_b$ produces a large change in PC, the detection algorithm is unstable. For each example, the change in percent coverage was computed for a 25% increase and 25% decrease in the threshold value as,

$$\Delta\mathrm{PC} = \mathrm{PC}_{\mathbf{I}_b \pm 0.25\mathbf{I}_b} - \mathrm{PC}_{\mathbf{I}_b}. \tag{5.1}$$

It was found that for the bimodal distribution example (Figure 3.13), increasing the threshold resulted in ΔPC of -1.78% and decreasing the threshold gave ΔPC equal to 3.17%. The results for increased and decreased threshold values for the examples from Figures 3.14 and 3.15 were -3.05% and 4.84%, and -3.86% and 24.58%, respectively. These three examples represent most of the variability in intensity distribution characteristics. The sensitivity analysis shows small changes in PC for all but the last case. In the third example, the normalization of pixel intensity (processing common to all data) reduced the contrast between wave rollers and the background, which increased the sensitivity to threshold choice and the uncertainty in the final results. The example shown in Figure 3.15 represents a minority of the data (17%). For the remaining 83% of the data analyzed, the mean ΔPC was 3.21%. This small change in percent coverage supports the robust nature of the presented thresholding method for IR imagery.

5.2 Roller Length

In order to evaluate the D81 dissipation parameterization, the roller lengths extracted from the binary masks must be corrected for projection errors. Using a geometric scaling based on wave slope and wave direction, the projected roller length, L_r', was transformed into the corrected roller length, L_r. In the projection of a 3-D wavy surface onto the 2-D plane, a steeper wave slope incurs a larger projection error than a milder wave slope, and this effect is amplified with increasing distance from the camera. Here, the wave slope ($\eta(t)$-derived wave

slope, shown in Figure 3.18) was assumed constant for each 18-minute timestack and on the order of a few degrees. This is an assumption made in previous work in both the laboratory and field. In the laboratory, Duncan (1981) observed wave slopes of 10-15°, and Haller and Catalan (2009) used wave slopes of 5, 12.6, and 20°. A survey of literature values from both the laboratory and field yields a range of 2-24° (Dally and Brown, 1995; Reniers and Battjes, 1997; Ruessink et al., 2001). SZO 2010 field estimates of mean wave slope ranged from 2-8°. Because estimated wave slope varied gradually over the experiment, it is concluded that assuming a constant wave slope for each 18-minute record is acceptable for a first test of Duncan's parameterization. Wave directions, relative to the camera look-direction, had an interquartile range of 33-69°. This is important because the wave propagation direction relative to the camera look-direction determines whether or not the roller length is a crest-perpendicular measurement or taken at an oblique angle to the crest. An obliquely measured roller length is larger than the actual roller length (Appendix A).

Figure 4.3 shows that, for the range of wave slopes and wave directions discussed (boxed), the correction ratio, r in (3.18), of L_r'/L_r ranges from 1 to 4. Specifically, when wave direction is less than 50°, the ratio maintains a value between 1 and 2 for all wave slopes. Above 50°, the correction ratio increases steeply with wave slope. Therefore, if waves propagate from a small range of directions, and the camera is positioned to observe along the mean propagation direction, variations in wave slope won't significantly affect our roller length measurement (for relatively small wave slopes 2-12°). Moreover, variations in roller length by a factor of 2 or 4 are small when compared to the range of $\varepsilon_{\mathrm{D81}}$ ($\mathcal{O}(10^4)$).

For this research, Figure 4.5 illustrates three examples of the range of roller lengths observed over an 18-minute timestack as a function of cross-shore position. Note that while there is a decrease in breaking wave count over the bar at high tide, the roller lengths achieved here are comparable to those measured at low tide. Therefore, the decrease in dissipation rate at high tide, discussed later, can be attributed to a decrease in breaking rate rather than a decrease in roller length. The bimodal pattern of roller length count over the transect (most evident in Figure 4.5(a,b)) suggests a threshold for the maximum roller length at each cross-shore location and outlines the conditions for depth-limited breaking at the FRF. For Figure 4.5(a), the peak roller length of ∼5m is reached at x=170m, 20m

onshore of the ADCP (the position at which the remote and *in situ* estimates are compared). Further analysis of the spatial distribution of roller length is beyond the scope of this thesis. Nevertheless, Figure 4.5 demonstrates the potential contribution of IR imagery to understanding breaking wave evolution in the surf zone.

5.3 Comparison of D81 and in situ dissipation rate estimates at a point

The D81 remote estimate at a point compares well with the *in situ* TKE dissipation rate estimate. A one-to-one agreement was not expected and is not observed because the *in situ* estimate derived from the ADCP at x=190m includes other sources of dissipation in addition to wave breaking. The *in situ* dissipation rate estimate was based on measurements of velocity variability in the water column. The final *in situ* estimate therefore includes dissipation due to bottom stress, shear from return flow off the beach, alongshore current shear, and wave breaking. At the same time, not all of the energy dissipated by a breaking wave may be measured by the ADCP. In addition to turbulence, breaking waves produce sound, heat, and bubbles, and the depth to which a breaking wave penetrates the water column depends on the type of breaker (Thornton and Guza, 1983). Most breakers at the FRF were spilling or plunging-spilling breakers, so dissipation was likely concentrated near the surface. Lastly, the *in situ* estimate has a relatively high noise floor (3-5W/m^2), resulting from the low water level (maximum 2.5m) above the ADCP, in conjunction with the ADCP's inability to sample near the surface and interference due to bubbles.

In general, the D81 remote estimate is of the same order of magnitude as the *in situ* estimate, which supports the validity of the D81 estimate. The times for which the D81 estimate drops far below the *in situ* estimate may be explained by the near-zero breaking rates. Given the high confidence in the detection algorithm's quality control procedures (minimizing false-positive and false-negative identification of breaking crests), and the D81 estimate's agreement with the *in situ* estimate for higher breaking rates, it is concluded that the low D81 wave dissipation rate estimates are reasonable. Even though these estimates are based on fewer waves, and therefore have weaker statistics, the D81 model is still physically applicable at low breaking rates.

The scatter plot in Figure 4.11 summarizes the correlation of the D81 and *in situ* esti-

mates. When the D81 dissipation rate estimate is large (greater than 1 W/m^2), the D81 and *in situ* estimates group around a one-to-one line. When the D81 dissipation rate estimate is lower than 1 W/m^2, the *in situ* estimate maintains values around 3 W/m^2, which could suggest that the dissipation rate due to sources other than wave breaking was approximately 3 W/m^2. Further analysis of the magnitude of the components of the *in situ* dissipation rate estimate is beyond the scope of this thesis.

5.4 Comparison of cross-shore integrated D81 and bulk energy flux

The cross-shore integrated remote D81 estimate of energy dissipation due to wave breaking is compared to the *in situ* bulk energy flux estimate in Figure 4.12. The D81 wave energy dissipation estimate was integrated from its offshore extent at x=245m to the shoreline, yielding the energy dissipation rate per unit crest length over the full transect. The bulk energy flux was computed from the energy density spectrum of the FRF 3-m ADCP, located near the offshore edge of the transect. The bulk energy flux was expected to be greater than the integrated D81 estimate, because wave breaking is only one path through which energy may be dissipated (Trowbridge and Elgar, 2001; Bryan et al., 2003; Feddersen, 2012), and in general, it is. Other sinks for wave energy include bottom stress, bubble injection, sound and heat production, advection by mean currents, or wave reflection off the beach (Figure 5.1). Reflection at the FRF at Duck, NC, can be as low as 3%, reach about 18% at high tide and low wave heights, and varies with the tide (Elgar, 1994). There are, however, a few times when the D81 wave dissipation estimate is larger than the bulk energy flux estimate: early on 09/10/2010 and during the storm on 09/12/2010 and 09/13/2010. One possible explanation for the larger D81 estimates is that the high-wind storm conditions produced local sea waves within the surf zone, which were not incorporated into the swell-dominated bulk energy flux calculation due to the instrument positioning, and these wind-aided breaking sea waves elevated the remotely-sensed dissipation rate. The ratio of the integrated D81 estimate to the bulk energy flux yields an estimate of the percentage of total incoming wave energy that is dissipated by wave breaking. Figure 5.2 shows this ratio, $E_{\mathrm{D81}}/\mathcal{F}$, over the experimental record. $E_{\mathrm{D81}}/\mathcal{F}$ has a minimum of 0, a maximum of 1.93, and a mean of 0.36. The ratio oscillates due to the tidally dependent remote dissipation rate estimate. Its mean, when

values greater than 1 are excluded, is 0.25, which suggests that under normal wind and wave conditions 25% of the incoming wave energy is dissipated via wave breaking. The D81 estimate may help improve nearshore circulation and storm surge models by incorporating temporally and spatially varying information about dissipation due to wave breaking in the surf zone (Figures 4.8 and 4.12).

5.5 Comparison of remotely-sensed wave energy dissipation rate estimates

The D81 remote estimate also compares well with the JB07 remote estimate of wave energy dissipation (Figure 4.14). Both estimates include some supplementary *in situ* data, although JB07 relies more heavily on factors difficult to estimate remotely, including H_{rms} and h. The D81 wave-by-wave remote estimate and the JB07 statistical remote estimate agree well in both magnitude and phase, which supports the field-applicability of both estimates and their potential usefulness for informing and being incorporated into nearshore models.

5.6 Figures

Figure 5.1: (left) Timestack created from 18 minutes of data along the transect shown in Figures 3.6 and 3.7. (right) An expansion of 2 minutes of data shows bright breaking waves over the bar (x≈190m) and at the shoreline. Reflected non-breaking and breaking waves can also be seen propagating away from the shore.

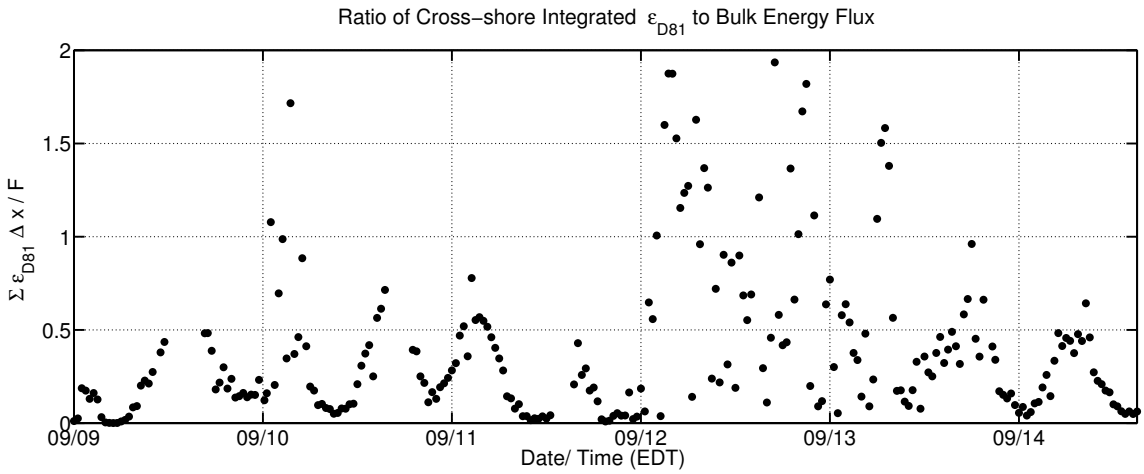

Figure 5.2: Time series of $\Sigma\varepsilon_{\mathrm{D81}}\Delta x/\mathcal{F}$, the ratio of cross-shore integrated remote dissipation rate estimate to the bulk energy flux.

Chapter 6

CONCLUSION

By exploiting the unique signals of active and residual foam in thermal IR imagery, a thresholding algorithm was developed to identify breaking waves along a transect in the surf zone. The roller length of each wave was extracted and corrected for image projection. Roller length was then used to estimate energy dissipation due to wave breaking via Duncan's (1981) formulation. The D81 dissipation rate estimate compared well with an *in situ* dissipation rate estimate measured at a point. When the D81 cross-shore dissipation rate profile was integrated, it also compared well to a bulk energy flux estimate, computed at the offshore edge of the transect. Both comparisons support the applicability of the D81 parameterization to the field. Remarkable agreement was found between the independent D81 and JB07 dissipation rate estimates. Since the JB07 model is often nested within nearshore circulation models, the agreement of the results from D81 and JB07 suggests that the D81 formulation may also work well within nearshore models. One advantage to using the D81 formulation is that is relies only on surface signatures, i.e. parameters visible to the IR imager, whereas the JB07 calculation requires wave height and water depth.

A next step for this research is to extend the methods for analysis along a transect to analysis over an area. Two-dimensional maps would capture the spatial and temporal variations of energy dissipation due to wave breaking and would be valuable to modelers for data assimilation. Processing IR images in two dimensions would also enable the measurement of wave direction on a wave-by-wave basis. With this information, projection error could be corrected with higher accuracy. Additionally, for future experiments, the IR camera should be optimally positioned to look along the typical wave propagation direction so that geometry-based errors can be minimized. To improve IR remote sensing capabilities, two IR cameras, one up-looking and one down-looking, should be deployed. The up-looking camera should image the region of sky that is reflected off the sea surface and imaged by the down-

looking camera. Overlap near the horizon of the two fields of view would help align the images so that the reflected sky conditions (e.g. cloud and sun position and movement) can be removed from the sea surface images. Removing the reflected background component from the IR signal of the sea surface may stabilize the background pixel intensity, so less normalization is necessary. Also, these IR images of emitted radiation (reflected component mostly removed) from sea surface can be used to estimate wave slope. A modulation transfer function could be developed using the dependence of emissivity on incidence angle to invert for wave slope (2.6). Validation and calibration could be completed with the help of LIDAR wave slope measurements. This IR-derived, wave-by-wave slope estimate could then be used, with roller length, in the D81 formulation to produce a truly remote estimate of energy dissipation due to wave breaking in the surf zone.

As a last note, there were many fundamental questions raised throughout this research that were not immediately relevant to the task at hand, but which should be given attention in the future. Perhaps some of the most basic and potentially insightful of these questions are: What does IR imagery reveal about the evolution of a breaking wave? How is the evolution of roller length controlled by initial wave height, bathymetry, and tidal fluctuations? These questions may be investigated using the SZO2010 data set.

BIBLIOGRAPHY

Battjes, J. (1972). Set-up due to irregular waves. *Coastal Engineering Proceedings 1*(13), 1993–2004.

Battjes, J., J. Janssen, et al. (1978). Energy loss and set-up due to breaking of random waves. In *Proc. 16th Int. Conf. Coastal Eng*, Volume 1, pp. 649–660.

Birkemeier, W. A., H. Miller, S. Wilhelm, A. DeWall, and C. Gorbics (1985). A user's guide to the coastal engineering research center's (cerc's) field research facility. Technical report, DTIC Document.

Booij, N., R. Ris, and L. H. Holthuijsen (1999). A third-generation wave model for coastal regions: 1. model description and validation. *Journal of Geophysical Research: Oceans (1978–2012) 104*(C4), 7649–7666.

Bourlier, C., J. Saillard, and G. Berginc (2000). Intrinsic infrared radiation of the sea surface. *Journal of Electromagnetic Wave and Applications 14*(4), 551–561.

Branch, R., C. Chickadel, A. Jessup, and R. Carini (2012, Dec. 3-7). Abstract os13e-1782. presented at 2012 Fall Meeting, AGU, San Francisco, Calif.

Branch, R., C. C. Chickadel, and A. T. Jessup (2014, January). Thermal infrared multipath reflection from breaking waves observed at large incidence angles. *IEEE Transactions on Geoscience and Remote Sensing 52*(1), 249–256.

Bryan, K. R., K. P. Black, and R. M. Gorman (2003). Spectral estimates of dissipation rate within and near the surf zone. *Journal of Physical Oceanography 33*(5), 979.

Collins, J. I. (1970). Probabilities of breaking wave characteristics. *Coastal Engineering Proceedings 1*(12), 399–414.

Dally, W. R. and C. A. Brown (1995). A modeling investigation of the breaking wave roller with application to cross-shore currents. *Journal of Geophysical Research: Oceans (1978–2012) 100*(C12), 24873–24883.

Dean, R. G. and R. A. Dalrymple (1984). *Water wave mechanics for engineers and scientists*. Prentice-Hall.

Duncan, J. (1981). An experimental investigation of breaking waves produced by a towed hydrofoil. *Proceedings of the Royal Society of London. A. Mathematical and Physical Sciences 377*(1770), 331–348.

Elgar, T. H. C. Herbers, R. T. G. (1994, July). Reflection of ocean surface gravity waves from a natural beach. *Journal of Physical Oceanography 24*(7), 1503–1511.

Feddersen, F. (2012). Scaling surf zone turbulence. *Geophysical Research Letters 39*(18), L18613.

Fogelberg, R. A. (2003a). A study of microbreaking modulation by ocean swell using infrared and microwave techniques. Master's thesis, University of Washington.

Fogelberg, R. A. (2003b). A study of microbreaking modulation by ocean swell using infrared and microwave techniques. Master's thesis, University of Washington.

G. O. Marmorino, G. B. S. (2005). Bright and dark ocean whitecaps observed in the infrared. *Geophysical Research Letters 32*(L11604), 4.

Gerbi, G. P., J. H. Trowbridge, E. A. Terray, A. J. Plueddemann, and T. Kukulka (2009, May). Observations of turbulence in the ocean surface boundary layer: Energetics and transport. *Journal of Physical Oceanography 39*(5), 1077–1096.

Grasso, F., B. Castelle, and B. Ruessink (2012). Turbulence dissipation under breaking waves and bores in a natural surf zone. *Continental Shelf Research 43*, 133–141.

Haller, M. C. and P. A. Catalan (2009, JUL 22). Remote sensing of wave roller lengths in the laboratory. *Journal of Geophysical Research-Oceans 114*.

Holland, K. T. and R. A. Holman (1997). Video estimation of foreshore topography using trinocular stereo. *Journal of Coastal Research 13*(1), 81–87.

Janssen, T. and J. Battjes (2007). A note on wave energy dissipation over steep beaches. *Coastal Engineering 54*(9), 711 – 716.

Jessup, A. T., W. E. Asher, M. Atmane, K. Phadnis, C. J. Zappa, and M. R. Loewen (2009, August). Evidence for complete and partial surface renewal at an air-water interface. *Geophysical Research Letters 36*, L16601.

Kuo, C. T. and S.-J. Kuo (1974). The effect of wave breaking on the statistical distribution of wave heights. In *Civil Engineering in the Oceans III*, pp. 1211–1231. ASCE.

Lamarre, E. and W. Melville (1991). Air entrainment and dissipation in breaking waves. *Nature 351*(6326), 469–472.

Lanckriet, T. and J. A. Puleo (2013). Near-bed turbulence dissipation measurements in the inner surf and swash zone. *Journal of Geophysical Research: Oceans 118*(12), 6634–6647.

Masuda, K. (2006, August). Infrared sea surface emissivity including multiple reflection effect for isotropic gaussian slope distribution model. *Remote Sensing of Environment 103*(4), 488–496.

Masuda, K., T. Takashima, and T. Y (1988, March). Emissivity of pure and sea waters for the model sea-surface in the infrared window regions. *Remote Sensing of Environment 24*(2), 313–329.

Nalli, N. R., P. J. Minnett, E. Maddy, W. W. McMillan, and M. D. Goldberg (2008). Emissivity and reflection model for calculating unpolarized isotropic water surface-leaving radiance in the infrared. 2: Validation using fourier transform spectrometers. *Applied optics 47*(25), 4649–4671.

Nalli, N. R., P. J. Minnett, and P. van Delst (2008). Emissivity and reflection model for calculating unpolarized isotropic water surface-leaving radiance in the infrared. i: Theoretical development and calculations. *Applied optics 47*(21), 3701–3721.

Niclos, R., V. Caselles, E. Valor, and C. Coll (2007, December). Foam effect on the sea surface emissivity in the 8-14 mu m region. *Journal of Geophysical Research-Oceans 112*(C12), C12020.

Plant, N., R. Holman, M. Freilich, and W. Birkemeier (1999, JUL 15). A simple model for interannual sandbar behavior. *Journal of Geophysical Research-Oceans 104*(C7), 15755–15776.

Reniers, A. and J. Battjes (1997). A laboratory study of longshore currents over barred and non-barred beaches. *Coastal Engineering 30*(1), 1–21.

Ris, R., L. Holthuijsen, and N. Booij (1999). A third-generation wave model for coastal regions: 2. verification. *Journal of Geophysical Research: Oceans (1978–2012) 104*(C4), 7667–7681.

Ruessink, B., J. Miles, F. Feddersen, R. Guza, and S. Elgar (2001). Modeling the alongshore current on barred beaches. *Journal of Geophysical Research: Oceans (1978–2012) 106*(C10), 22451–22463.

Stockdon, H. and R. Holman (2000, SEP 15). Estimation of wave phase speed and nearshore bathymetry from video imagery. *Journal of Geophysical Research-Oceans 105*(C9), 22015–22033.

Thomson, J. (2012). Wave breaking dissipation observed with "swift" drifters. *Journal of Atmospheric and Oceanic Technology 29*(12), 1866 – 1882.

Thornton, E. and R. Guza (1983). Transformation fo wave height distribution. *Journal of Geophysical Research-Oceans and Atmospheres 88*(NC10), 5925–5938.

Trowbridge, J. and S. Elgar (2001). Turbulence measurements in the surf zone. *Journal of Physical Oceanography 31*(8), 2403.

W. Eifler, C. J. D. (2001). Modeling the thermal surface signature of breaking waves. *Journal of Geophysical Research 106*(C11), 27, 163–27, 185.

Wiles, P. J., T. P. Rippeth, J. H. Simpson, and P. J. Hendricks (2006). A novel technique for measuring the rate of turbulent dissipation in the marine environment. *Geophysical Research Letters 33*(21).

Appendix A

GEOMETRY CORRECTIONS

A.1 Roller length corrections

In order to correct for projection error, it must be assumed that the three-dimensional position of the toe of the wave roller is correctly identified at $(x, y, z = MSL)$, and can therefore serve as a reference point, $\mathbf{p}_1$. From $\mathbf{p}_1$, the projection of the roller length, $\mathbf{p}_2$, can be defined as,

$$\mathbf{p}_2 = \mathbf{p}_1 + [L_r', 0, 0]. \tag{A.1}$$

The line, $\vec{\mathbf{l}}$, that begins at the camera's position, $\mathbf{c}$, passes through the true breaking wave crest, $\mathbf{l}_{crest}$, and ends at $\mathbf{p}_2$, can be written as,

$$\vec{\mathbf{l}} = \mathbf{c} + t(\mathbf{p}_2 - \mathbf{c}). \tag{A.2}$$

Figure A.1 illustrates this geometry and also identifies wave roller slope, θ, and wave propagation direction relative to the camera look-direction, ϕ. In order to find $\mathbf{l}_{crest}$, we must find the intersection of $\vec{\mathbf{l}}$ and the wave face. The wave face is defined as,

$$\mathrm{z}_{int} = \mathrm{p}_{1,3} - \frac{dz}{dx}\mathrm{p}_{1,1} - \frac{dz}{dy}\mathrm{p}_{1,2}, \tag{A.3}$$

where slopes dz/dx and dz/dy are given by,

$$\frac{dz}{dx} = \tan\theta\cos\phi, \tag{A.4}$$

$$\frac{dy}{dx} = \tan(90- \mid \phi \mid), \quad \text{and} \tag{A.5}$$

$$\frac{dz}{dy} = \frac{dz/dx}{dy/dx} = \frac{\tan\theta\cos\phi}{\tan(90- \mid \phi \mid)}. \tag{A.6}$$

Setting equal (A.2) and (A.3) and solving for the point of intersection, t_{crest}, yields,

$$t_{crest} = \frac{\mathrm{z}_{int} - \mathrm{c}_3 + \frac{dz}{dx}\mathrm{c}_1 + \frac{dz}{dy}\mathrm{c}_2}{(\mathbf{p}_2 - \mathbf{c}) \cdot (-\frac{dz}{dx}, -\frac{dz}{dy}, 1)}. \tag{A.7}$$

t_{crest} can then be used in (A.2) to solve for $\mathbf{l}_{crest}$:

$$\mathbf{l}_{crest} = \mathbf{c} + t_{crest}(\mathbf{p}_2 - \mathbf{c}). \tag{A.8}$$

The distance from $\mathbf{p}_1$ to $\mathbf{l}_{crest}$ is the corrected roller length, L_r:

$$L_r = \frac{\mathrm{l}_{crest,3} - \mathrm{p}_{2,3}}{\sin\theta}. \tag{A.9}$$

Finally, the ratio of L_r' to L_r, r, is computed:

$$r = \frac{L_r'}{L_r} = \frac{L_r' \sin\theta}{\mathrm{l}_{crest,3} - \mathrm{p}_{2,3}}. \tag{A.10}$$

This ratio is not necessary in the correction process, but it is useful in assessing the magnitude of the projection error as a function of wave roller slope and wave direction (Figure 4.3).

A.2 Figures

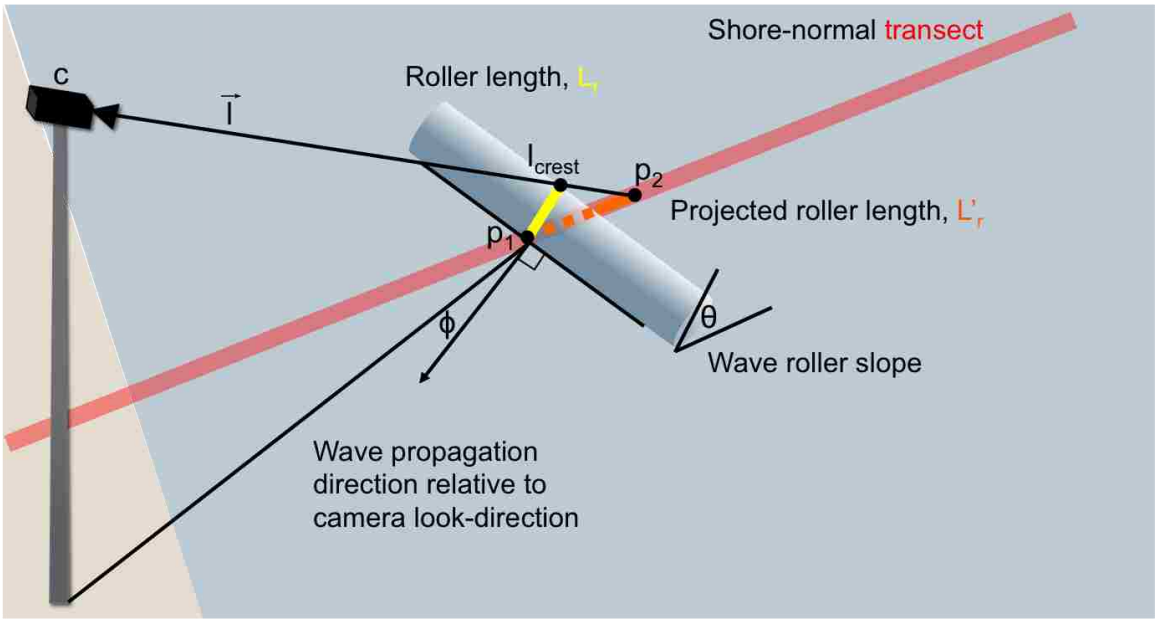

Figure A.1: Schematic of camera-wave geometry.

```
% Given Lproj, theta, phi, c, and p1. Find Lr and Ratio.

% camera position
load Iomega_HDD/Duck/RAW/DUCK_2010_Sept_FRFTowerGeometry.mat
tilt = GFRFTower.geometry.tilt*180/pi;
c = [GFRFTower.camera.XYZ(1),GFRFTower.camera.XYZ(2),GFRFTower.camera.XYZ(3)];

% load wave slope time series
load('Iomega_HDD/Duck/goodDATA/meanslope.mat')
% wave slope (deg): theta = [2.9,5,6,10,12.6,14.7,16.3,19.5,20,24.2] from ...
    the lit

% load peak wave direction time series
load('Iomega_HDD/Duck/goodDATA/ALLdata3.mat','TIME','X')
load('Iomega_HDD/Duck/goodDATA/EnergyFlux.mat','weighted_a_unwrap','t') % ...
    wavedat time is already in EDT
% wave dir from true N
wavedirN = weighted_a_unwrap;
wavedirX = 90-wavedirN+17;
wavedirX_interp = interp1(t,wavedirX,epoch2Matlab(TIME-4*60*60));
wavedirX_interp(1) = wavedirX(1);
% phi = angle wave face makes with x-axis

% load tidal data to get z coord for p1_all = (x,y=725,z=tide)
load('Iomega_HDD/Duck/RAW/DuckTide_NAVD.txt')
tide = DuckTide_NAVD(:,5);
% create time vec for tide
yy = repmat(2010,length(tide),1);
mm = repmat(09,length(tide),1);
dd = ...
    [repmat(09,24,1);repmat(10,24,1);repmat(11,24,1);repmat(12,24,1);repmat(13,24,1);repmat(14
hh = DuckTide_NAVD(:,3);
minu = repmat(00,length(tide),1);
sec = repmat(00,length(tide),1);
ttide = datenum(yy,mm,dd,hh,minu,sec);
% position in SZ with z=tidal stage
```

```
% p1_all = ...
    [(85:5:245)',repmat(725,33,1),repmat(tide(find(matlab2Epoch(ttide)≤TIME(i),1,'last')),33,1)]; ...
    % location along transect of roller toe

% location of files
imReadPath = 'Iomega_HDD/Duck/goodDATA/DUCK4/';

for xx=1:length(X)
for i=1:length(TIME)
    % position of breakers at (190,725,tide) for correction of Lr at that ...
        point in the SZ
    % (correction for Duncan eps comparison plot)
    p1_all(i,1:3) = ...
        [X(xx),725,tide(find(matlab2Epoch(ttide)≤TIME(i),1,'last'))];
end
% avg wave slope
theta_all = meanslope;
% % max slope
% theta_all = maxslope;
% min slope
% theta_all = minslope;
phi_all = wavedirX_interp;
% evaluate function
[LrPmn,LrPmd,LrCorr,LrRatio,LrTime] = ...
    findLrRatio(imReadPath,c,p1_all,theta_all,phi_all); % findLrRatio ...
    function provided below
for i=1:length(LrPmn)
    LrPmntot{i,xx} = LrPmn{i};
    LrPmdtot{i,xx} = LrPmd{i};
    LrCorrtot{i,xx} = LrCorr{i};
    LrRatiotot{i,xx} = LrRatio{i};
end
end
```

```
function [LrPmn,LrPmd,LrCorr,LrRatio,LrTime] = ...
    findLrRatio(imReadPath,c,p1_all,theta_all,phi_all)

%
% INPUTS
% imReadPath:   file read path
% c:            camera position in FRF coord system
% p1_all:       position of along transect of wave toe (tidally adjusted)
% theta_all:    range of wave slopes observed
% phi_all:      range of wave directions observed
%
% OUTPUTS
% LrCorr:       true Lr, projection error corrected
% LrRatio:      ratio of Lr' to Lr
% LrTime:       time stamp in EDT (Matlab time)
%

% load time stack file
D = dir([imReadPath '*.mat']);

%%
for i = 1:length(D)

clear M; clear gzero; clear dxind; clear wavea; clear waveb;
clear LrPmn; clear LrPmd;

% load file
fn = [imReadPath D(i,1).name];
load(fn,'timevec','x','masksm','Lr','Nt')

% create time in matlab EDT
if i==1
    LrTime(i) = epoch2Matlab(timevec(1)-4*60*60);
elseif i>1
    LrTime(i) = epoch2Matlab(matlab2Epoch(LrTime(i-1))+30*60);
end
```

```
36
37 if isempty(timevec)
38     LrPmn{i} = nan;
39     LrPmd{i} = nan;
40     LrCorr{i} = nan;
41     LrRatio{i} = nan;
42     continue
43 end
44
45 % identify waves that cross desired x loc
46 M = bwlabel(masksm,4);
47 xind = find(x==p1_all(1,1));
48 gzero = find(M(:,xind)>0);
49
50 if numel(gzero)==0
51     LrPmn{i} = nan;
52     LrPmd{i} = nan;
53     LrCorr{i} = nan;
54     LrRatio{i} = 0;
55     continue
56 end
57
58 dxind = diff(gzero);
59 wavea(1) = gzero(1);
60 ends = find(dxind>1);
61 for k=1:length(ends)
62     waveb(k) = gzero(ends(k));
63     wavea(k+1) = gzero(ends(k)+1);
64 end
65 waveb(length(wavea)) = gzero(end);
66
67 % compute mean and median roller length for each individually identified wave
68 for k=1:length(wavea)
69     if (length(x)-xind)<50
70         Mw = M(wavea(k):waveb(k),(xind-50):end);
71     elseif xind<51
```

```
72          Mw = M(wavea(k):waveb(k),1:(xind+50));
73      else
74          Mw = M(wavea(k):waveb(k),(xind-50):(xind+50));
75      end
76      LrPmn{i}(k) = mean(sum(Mw>0,2).*0.25);
77      LrPmd{i}(k) = median(sum(Mw>0,2).*0.25);
78  end
79
80  % if no breakers detected, skip
81  if isempty(LrPmn{i})
82      LrCorr{i} = nan;
83      LrRatio{i} = nan;
84      continue
85  end
86
87  % choose position in SZ
88  p1 = p1_all(i,:);
89
90  % choose wave slope
91  theta = theta_all(i);
92  if isnan(theta)
93      theta = theta_all(i+1);
94  end
95
96  % choose wave direction
97  phi = phi_all(i);
98
99  % correct projection error
100 for k = 1:length(LrPmn{i})
101         % intersection of line from camera to p1+Lproj and wave face plane
102         % line: ll = c+t*(p2-c);
103         % wave-face plane: z = zint + dzdx*x + dzdy*y
104         p2 = p1+[LrPmn{i}(k),0,0];
105         dzdx = tand(theta)*cosd(phi);
106         dydx = tand(90-abs(phi));
107         dzdy = dzdx/dydx;
```

```
108         zint = p1(3)-dzdx*p1(1)-dzdy*p1(2);
109         t = (zint-c(3)+dzdx*c(1)+dzdy*c(2))/dot(p2-c,[-dzdx,-dzdy,1]);
110         crest = c+t*(p2-c);
111         LrCorr{i}(k) = (crest(3)-p2(3))/sind(theta);
112         LrRatio{i}(k) = LrPmn{i}(k)./LrCorr{i}(k);
113 end
114 end
115 end
```

Appendix B

MATLAB CODE

B.1 Normalization of IR timestack and thresholding algorithm

```
% normalization and thresholding

% load time stack file
imReadPath = 'Iomega_HDD/Duck/goodDATA/DUCK4/';
D = dir([imReadPath '*.mat']);

for i=1:length(D)
clear data
fn = [imReadPath D(i,1).name];
load(fn)
data = double(data);
Nt = size(data,1);
Nx = size(data,2);
if isempty(data)
    continue;
end

% remove the shore
xmean = nanmean(data,1);
shorebreak = find(xmean(1:200)==max(xmean(1:200)));
if shorebreak≥17
    shoreind = shorebreak-16; % go 4m onshore of max xmean
elseif shorebreak≤10
    shoreind = 1;           % include entire x-extent (high tide)
else
    shoreind = shorebreak-4;  % go 1m onshore of max xmean
end
```

```
28 datans = horzcat(nan(Nt,shoreind-1),data(:,shoreind:end)); % datans = data ...
       no shore
29
30 % normalize data wrt time, then space
31 % this normalization still sometimes makes shore break too dim to be id'd
32 dmt = datans-repmat(prctile(datans,25,2),1,Nx);
33 dmtx = dmt-repmat(prctile(dmt,5,1),Nt,1);
34 % normalize min pix int to zero
35 ndata = dmtx-min(dmtx(:));
36 L = max(ndata(:))+1;         % L: number of pix int levels
37
38 % p(I)
39 bins = 0:(L-1);
40 P = histc(ndata(:),bins);
41 P = P./sum(¬isnan(ndata(:)));
42 P = smooth(P);
43 % p'(I)
44 di = mean(diff(bins));
45 dbins = bins(1)+(di/2):di:bins(end);
46 dP = diff(P)./di;
47 dP = smooth(dP);
48 % p''(I)
49 ddbins = bins(2):di:(bins(end)-1);
50 ddP = diff(dP)./di;
51 ddP = smooth(smooth(ddP));
52
53 % find global min of p'(k)
54 globmindP = find(dP==min(dP));
55 % find zero-crossing that follows global min of p'(k)
56 zcrossdP = globmindP-1+find(dP(globmindP:end)≥0,1);
57 % if no zero-crossing or zcross too far from globmindP, use p''(k)
58 if isempty(zcrossdP) || zcrossdP≥length(dbins)
59     % find local max that follows the global min
60     globminddP = find(ddP==min(ddP));
61     maxposconcav = ...
           globminddP-1+find(ddP(globminddP:end)==max(ddP(globminddP:end)));
```

```
62      % try using the minimum positive concavity following maxposconcav
63      posddP = find(ddP(maxposconcav:end)>0);
64      [m ind] = sort(ddP(maxposconcav-1+posddP));
65      % find 25th percentile above the max that follows the min (median was
66      % too high and resulted in underdetection)
67      ffind = round(length(ind)/4);
68      % Ib = breaking pix int
69      Ib = ddbins(maxposconcav-1+posddP(ffind));
70      zcross = 1; % keep track of method used (0=no zero-crossing use p'')
71  else
72      % name threshold based on zero-crossing
73      Ib = dbins(zcrossdP);
74      zcross = 0; % keep track of method used (1=zero-crossing of p' used)
75  end
76
77  % create mask
78  mask = zeros(size(ndata));
79  mask(ndata(:)≥Ib) = 1;
80  % check for underdetection
81  if sum(mask(:))/numel(mask(:,shoreind:end))<0.003
82  % 0.003 chosen b/c that's how much you'd expect with only shore break
83      % find local max that follows the global min
84      globminddP = find(ddP==min(ddP));
85      maxposconcav = ...
            globminddP-1+find(ddP(globminddP:end)==max(ddP(globminddP:end)));
86      % try using the minimum positive concavity following maxposconcav
87      posddP = find(ddP(maxposconcav:end)>0);
88      [m ind] = sort(ddP(maxposconcav-1+posddP));
89      % find 25th percentile above the max that follows the min (median was
90      % too high and resulted in underdetection)
91      ffind = round(length(ind)/4);
92      Ib = ddbins(maxposconcav-1+posddP(ffind));
93      zcross = 2;
94      % redo mask
95      mask = zeros(size(ndata));
96      mask(ndata(:)≥Ib) = 1;
```

```
end
% clean mask
masksm = bwmorph(mask,'clean');
masksm = bwmorph(masksm,'majority');
masksm = bwmorph(masksm,'fill');
masksm = bwmorph(masksm,'majority');

% forward difference in x to get Lr
fdx = diff(masksm,1,2);
%initialize Lr
Lr = nan(Nt,Nx);
% compute Lr and x-shore roller position
for j=1:Nt
    toe = find(fdx(j,:)==1);
    if isempty(toe)
        continue
    else
    crest = find(fdx(j,:)==-1);
    if numel(crest)<numel(toe)
        crest = [crest,Nx];
    end
    if numel(toe)<numel(crest)
        toe = [1,toe];
    end
    roller = round((toe+crest)/2);
    Lr(j,roller) = x(crest)-x(toe);
    end
end
% summary stats: median Lr at each x-shore position
Lr_medx = nanmedian(Lr,1);

% forward difference in t to get Nb
fdt = diff(masksm,1,1);
Nb = nansum(fdt>0,1);
% divide by record length to get BR
tau = timevec(end)-timevec(1);
```

```
133 BR = Nb/tau;
134 end
135
136 % load time stack file
137 imReadPath = 'Iomega_HDD/Duck/goodDATA/DUCK4/';
138 D = dir([imReadPath '*.mat']);
139
140 for i=1:length(D)
141 clear data
142 fn = [imReadPath D(i,1).name];
143 load(fn,'timevec','x','data','BR','Lr','Lr_medx','Nx','zcross')
144 FN{i} = fn;
145 if isempty(data)
146     TIME(i) = TIME(i-1)+30*60;
147     BRr(i,:) = nan(1,Nx);
148     LPROJ(i,:) = nan(1,160);
149     Zcross(i) = nan;
150 else
151     TIME(i) = timevec(1);       % time vector
152     BRr(i,:) = BR;                          % breaking rate
153     Zcross(i) = zcross;
154     k = 1;
155     for j=1:4:(length(x)-1)
156         LPROJ(i,k) = nanmedian(reshape(Lr(:,j:(j+3)),length(timevec)*4,1));
157         % uncorrected median roller length binned every 0.5m instead of ...
              every 0.25m
158         k = k+1;
159     end
160 end
161 end
162
163 X = x;  % FRF transect
164 k = 1;
165 for i=1:4:(length(X)-3)
166     XLr(k) = mean(X(i:(i+3)));
167     k = k+1;
```

```
168 end
169 clear BR
170 BR = BRr;
171 clear BRr
```

B.2 Evaluating D81

```
% load and compute Duncan for each LrCorr
%
% Duncan 1981 estimate of energy dissipation due to wave breaking
% empAL2:       empirical reln b/t x-sectional area of roller and its length ...
    +/- 0.01
% rho sea:      density of underlying sea water (kg/m^3)
% rhop:         density of breaking region (kg/m^3) (this is aerated)
% rhoratio:     rhop/rhosea
% g:                gravity (m/s^2)
% L:                roller length (m)
% theta:        wave slope (rad) from the lit ...
    [2.9,5,6,10,12.6,14.7,16.3,19.5,20,24.2]
% tau:              shear stress along the breaking boundary (N/m^2, Pascals)
%

load('Iomega_HDD/Duck/goodDATA/LrcorrectionsTOTredo','LrCorrtot','LrTime')
% LrTime already in EDT (matlab)
load('Iomega_HDD/Duck/goodDATA/ALLdata3.mat','X')
load('Iomega_HDD/Duck/goodDATA/meanslope.mat')

% constants
empAL2 = 0.11;
rhoratio = 0.6;
rhosea = 1025;          % (kg/m^3)
rhop = rhoratio*rhosea;     % (kg/m^3)
g = 9.81;                       % (m/s^2)

% avg wave slope
theta = meanslope;
% max wave slope
% theta = maxslope;
% min wave slope
% theta = minslope;
```

```
32
33 % dissipation rate
34 for xx=1:size(LrCorrtot,2)
35     for i=1:length(LrTime)
36         if (isnan(LrCorrtot{i,xx}(1)))
37             epsD{i,xx} = nan;
38             epsDtot(i,xx) = nan;
39             continue
40         end
41         for j=1:length(LrCorrtot{i,xx})
42             Lr = LrCorrtot{i,xx}(j);
43             epsD{i,xx}(j) = empAL2*(Lr^2)*rhop*g*sind(theta(i));
44         end
45         epsDtot(i,xx) = (1/(18*60))*sum(epsD{i,xx});
46     end
47 end
48
49 % use this for just at x=190
50 xx = find(X==190);
51 for i=1:length(LrTime)
52     if (isnan(LrCorr{i}(1)))
53         epsD{i} = nan;
54         epsDtot(i) = nan;
55         continue
56     end
57     for j=1:length(LrCorr{i})
58         Lr = LrCorr{i}(j);
59         epsD{i}(j) = empAL2*(Lr^2)*rhop*g*sind(theta(i));
60     end
61     epsDtot(i) = (1/(18*60))*sum(epsD{i});
62 end
```

B.3 Bulk energy flux calculation

```
% compute bulk energy flux at x=190m
load('Iomega_HDD/Duck/goodDATA/ALLdata3.mat','TIME','BR','X')
load('Iomega_HDD/Duck/FRF/adopSpec.01.201009_07_17.mat') %3-m adop

% define variables
t = matlab2Epoch(wavedat.time);
ind = find(t≥TIME(1),1):find(t≥TIME(end),1);
t = t(ind); % UTC
dirtime = epoch2Matlab(t-4*60*60); % wavedat time in EDT
% get rid of bad data
bad = find(diff(dirtime)<0.04);
dirtime(bad(1):bad(end)) = [];
t = dirtime;

h = wavedat.depthP(ind);
h(bad(1):bad(end)) = [];
Hs = wavedat.hs(ind);
Hs(bad(1):bad(end)) = [];
Tp = 1./wavedat.fp(ind);
Tp(bad(1):bad(end)) = [];
g = 9.81;
rho = 1025;

for i=1:length(ind)
    Edir{i} = wavedat.espt{ind(i)};
    E1d{i} = wavedat.dwAvv{ind(i)};
end
for i=bad(1):bad(end)
    Edir(i) = [];
    E1d(i) = [];
end

f = wavedat.dwfhz;
```

```
34 a = wavedat.dwdeg;
35 % unwrap angles
36 for i=1:length(Edir)
37     Edir_unwrap{i} = [Edir{i}(:,91:end),Edir{i}(:,1:90)];
38 end
39 a_unwrap = [a(91:end)-360,a(1:90)];
40
41 for i=1:length(t)
42     % energy-weighted frequency
43     weighted_f(i) = sum(f.*E1d{i})./sum(E1d{i});
44     % energy weighted wave direction
45     weighted_a_unwrap(i) = ...
           sum(a_unwrap.*sum(Edir_unwrap{i},1))./sum(sum(Edir_unwrap{i}));
46 end
47
48 % calc energy flux from 1D energy spectra
49 for i=1:length(t)
50     for j=1:length(f)
51         k = wavenumber(g,2*pi*f(j),0,h(i),0,0);
52         n = 0.5*(1+(2*k*h(i))/sinh(2*k*h(i)));
53         C = (g/(f(j)*2*pi))*tanh(k*h(i));
54         Cg(i,j) = n*C;
55     end
56         F(i) = rho*g*sum(E1d{i}.*Cg(i,:))*mean(diff(f));
57 end
```

B.4 Evaluating JB07

```
% get ETA from adopp data
load('Iomega_HDD/Duck/goodDATA/ALLdata3.mat')
load('Iomega_HDD/Duck/ADOPP/SurfZoneOptics_Aquadopp_08-11Sep2010.mat','timemeans');
ind1 = find(TIME≤matlab2Epoch(timemeans(end)),1,'last');
fname = 'Iomega_HDD/Duck/ADOPP/SurfZoneOptics_Aquadopp_08-11Sep2010.mat';
ETA = [];
TIME_adopp = [];
Hh = [];

for nn=1:ind1
    tstart = epoch2Matlab(TIME(nn));
    tend = epoch2Matlab(TIME(nn+1));
    clear eta;
    [eta,presmeans,time_adopp] = pres2Eta(fname,tstart,tend);
    kk = 1;
    clear h;
    for ii=1:60:(length(eta)-59)
        h(ii:(ii+59)) = eta(ii:(ii+59))+presmeans(kk);
        kk = kk+1;
    end
    h((length(h)+1):length(eta)) = eta((length(h)+1):end)+presmeans(kk);
    if isempty(ETA)
        ETA = eta;
        Hh = h;
        TIME_adopp = matlab2Epoch(time_adopp)-4*60*60;  % epoch time EDT
    else
        ETA = vertcat(ETA,eta);
        Hh = horzcat(Hh,h);
        TIME_adopp = vertcat(TIME_adopp,matlab2Epoch(time_adopp)-4*60*60);
    end
end

load('Iomega_HDD/Duck/ADOPP/SurfZoneOptics_Aquadopp_11-14Sep2010.mat','timemeans');
```

```
34 ind2 = find(TIME≤matlab2Epoch(timemeans(end)),1,'last');
35 fname = 'Iomega_HDD/Duck/ADOPP/SurfZoneOptics_Aquadopp_11-14Sep2010.mat';
36
37 for nn=(ind1+1):(ind2-1)
38     tstart = epoch2Matlab(TIME(nn));
39     tend = epoch2Matlab(TIME(nn+1));
40     clear eta;
41     [eta,presmeans,time_adopp] = pres2Eta(fname,tstart,tend); % pres2Eta ...
           function included below
42     kk = 1;
43     clear h;
44     if length(eta)<5
45         continue
46     end
47     for ii=1:60:(length(eta)-59)
48         h(ii:(ii+59)) = eta(ii:(ii+59))+presmeans(kk);
49         kk = kk+1;
50     end
51     h((length(h)+1):length(eta)) = eta((length(h)+1):end)+presmeans(kk);
52     ETA = vertcat(ETA,eta);
53     Hh = horzcat(Hh,h);
54     TIME_adopp = vertcat(TIME_adopp,matlab2Epoch(time_adopp)-4*60*60);
55 end
56
57 % get Hrms from ETA
58 for i=1:length(TIME)
59     tind = ...
           find(TIME_adopp≤(TIME(i)-(4*60*60)),1,'last'):find(TIME_adopp≥(TIME(i)-(4*60*60)+18*60),1);
60     STD_18(i) = nanstd(ETA(tind));
61     TIME_adopp_18(i) = TIME(i)-(4*60*60)+9*60; % time in epoch EDT (midpoints)
62 end
63 Hmo = 4.*STD_18;
64 Hrms18 = Hmo./1.350;
65 Hrms18(123:127) = nan;  % no data for TIME_adopp_18(123:127)
66
67 % calculate dissipation rate at adopp location
```

```
68 load('Iomega_HDD/Duck/goodDATA/ETA_h_adopp.mat','Hh','TIME_adopp')
69 for i=1:length(TIME)
70     tind = ...
           find(TIME_adopp≤(TIME(i)-(4*60*60)),1,'last'):find(TIME_adopp≥(TIME(i)-(4*60*60)+18*60
71     h18(i) = nanmean(Hh(tind));
72 end
73 h18(123:127) = nan;
74
75 B = 1;
76 g = 9.81;
77 rho = 1025;
78 xind = find(X==190);
79 Br = nanmean(BR(:,(xind-1):(xind+1)),2);
80
81 epsBJ = (3*sqrt(pi)/16)*B*rho*g*Br'.*(Hrms18.^3)./h18;
```

```
function [eta,presmeans,time_adopp] = pres2Eta(fname,tstart,tend)

% Time increment should be on the order of minutes, not hours.
load(fname,'pres','presmeans','presvar','time','timemeans')

% overall corrections for spikes and tide, convert to dbar %
% smooth presmeans to remove spikes
presmeans = smooth(presmeans);

% threshold a diff of pres to remove spikes
presdiff = diff(pres);
ind = find(presdiff<-2);
pres(ind) = (pres(ind-1)+pres(ind+1))/2;

% remove tide using minute-means
% subtract presmeans from pres to remove tide signal
k = 1;
for i=1:60:length(pres)
    if k≤length(presmeans)
    presnomn(i:i+59) = pres(i:i+59)-presmeans(k);
    k = k+1;
    end
end

% convert units 1dbar = 10000Pa
presnomn = presnomn*10000;

% time increment of interest for pres time series
indt1 = find(time≥tstart,1);
indt2 = find(time≥tend,1);

% time increment of interest for presmeans time series
indt1m = find(timemeans≥tstart,1);
indt2m = find(timemeans≥tend,1);

p = presnomn(indt1:indt2);
```

```
37 t = time(indt1:indt2);
38 m = length(t);
39 fs = 1;
40 T = m*fs;
41 if rem(m,2) == 0
42   f = [((m/2)):-1:(-(m/2-1))]'/T;
43 else
44   f = [((m-1)/2):-1:(-(m-1)/2)]'/T;
45 end
46 f = ifftshift(f);
47 P = fft(p);
48
49 % Calculate wave height
50 g = 9.81;
51 rho = 1025;
52 d = mean(pres); %dbar¬m
53 % find k vec
54 Tp = 1./abs(f);
55 % can't go to really low freq, or really long period b/c they converge too ...
       slowly... threshold for reasonable speed f(1000) = 0.0038 Hz
56 L0 = (g*(Tp.^2))/(2*pi);
57 L = L0;
58 for i=1:length(L0)
59     Ltemp = 0;
60     while abs(L(i)-Ltemp)>0.05
61         Ltemp = L(i);
62         L(i) = L0(i)*tanh(2*pi*d/Ltemp);
63     end
64 end
65 k = (2*pi)./L;
66
67 % write specific Kz for f=0
68 z = -d;
69 Kz = cosh(k*(z+d))./cosh(k*d);
70 Kz(isinf(Tp)) = 1; % for f=0
71 Eta = P(:)./(rho*g*Kz);
```

```
72
73 eta = ifft(Eta);
74 time_adopp = t;
75 presmeans = presmeans(indt1m:indt2m);
76
77 end
```